UNIVERSITÀ
DEGLI STUDI
DI PADOVA

Sede Amministrativa: Università degli Studi di Padova

Dipartimento di Scienze Chimiche

CORSO DI DOTTORATO DI RICERCA IN SCIENZE MOLECOLARI
CURRICOLO: SCIENZE CHIMICHE
CICLO XXXV

PROBING THE ULTRAFAST DYNAMICS OF BIOLOGICAL AND BIOINSPIRED SYSTEMS BY MULTIDIMENSIONAL SPECTROSCOPIES

Coordinatore: Ch.mo Prof. Leonard J. Prins
Supervisore: Ch.mo Prof. Elisabetta Collini

Dottoranda: Elisa Fresch

Abstract

During the last years, biological light-harvesting systems have been extensively studied for their capability of capturing sunlight and converting it into energy. These systems have developed new strategies and optimized their structures to reach remarkable efficiency. Thus, a full knowledge of all the finer details regulating the processes driving light-matter interaction and energy transfer among molecules would allow us to design and synthesize new artificial molecules or improve the existing ones. As widely known, relaxation dynamics is strongly influenced by the surroundings and by the coupling with the vibrations of the molecules, so the characterization of relaxation processes is of crucial importance. In the study of light-harvesting, particular attention has been dedicated to the role that the environment plays in tuning the properties of photoactive chromophores. For example, a scaffold can act as a structural framework that holds the chromophores in a specific orientation, but can also affect their photophysical properties. Moreover, when the molecules are positioned close to each other, interchromophore electronic interactions can be strong enough to form delocalized states that unfold new energy transfer pathways.

In order to fully characterize these processes, a useful tool is represented by Two-Dimensional Electronic Spectroscopy (2DES). Since its development in the late 1990s, it has gained particular interest for its capability of following the ultrafast dynamics of complex systems both with a temporal and a spatial resolution, allowing us to reveal fine details, often not available with other techniques.

In this work, we exploited 2DES to characterize the relaxation dynamics of different systems in the femtosecond regime. In the first part, we provided a detailed investigation of the peculiar signatures of isolated Chlorophyll *b*, one of the most widespread light-harvesting chromophore. Subsequently, we exploited the knowledge acquired in the study of an isolated pigment to investigate the ultrafast behaviour of a natural pigment-protein complex, the Water-Soluble Chlorophyll-binding Protein. Then, we make us of the knowledge acquired on biological samples to engineer and study a new artificial bioinspired system, more specifically

a functionalized boron dipyrromethene (BODIPY) properly engineered to form a dimer motif. Lastly, in an attempt to push even further our approach toward possible biomimetic applications, we implemented a new experimental scheme of the 2DES technique, the Action-2DES (A-2DES). With A-2DES, the detected signal is a real property of the system, enabling us to operate at the real working conditions of the devices.

Abstract in lingua italiana

Negli ultimi anni, i complessi antenna biologici sono stati ampiamente studiati per la loro capacità di catturare la luce solare e convertirla in energia. Questi sistemi hanno sviluppato nuove strategie e ottimizzato le loro strutture per raggiungere una notevole efficienza. Quindi, la conoscenza di tutti i dettagli che regolano i processi di interazione luce-materia e il trasferimento di energia tra le molecole ci permette di progettare e sintetizzare nuove molecole artificiali o di migliorare quelle esistenti. Come ampiamente noto, la dinamica di rilassamento è fortemente influenzata dall' ambiente circostante e dall'accoppiamento con le vibrazioni delle molecole, per cui è di importanza cruciale raggiungere una completa caratterizzazione dei processi di rilassamento. Nello studio del processo di *light-harvesting*, particolare attenzione è stata posta sul ruolo dell'ambiente nella regolazione delle proprietà dei cromofori fotoattivi. Ad esempio, la struttura proteica è utilizzata per organizzare i cromofori in un orientamento specifico, ma può anche influenzare le loro proprietà fotofisiche. Inoltre, quando le molecole sono posizionate vicine l'una all'altra, le interazioni elettroniche tra diversi comofori possono essere abbastanza forti da formare stati delocalizzati che aprono nuove vie di trasferimento dell'energia.
Per caratterizzare completamente questi processi, uno strumento utile è rappresentato dalla Spettroscopia Elettronica Bidimensionale. Fin dal suo sviluppo alla fine degli anni anni '90, ha acquisito particolare interesse per la sua capacità di seguire le dinamiche ultraveloci di sistemi complessi con una risoluzione sia temporale che spaziale, permettendo di rivelare dettagli spesso non disponibili con altre tecniche.
In questo lavoro, abbiamo sfruttato la Spettroscopia Elettronica Bidimensionale per caratterizzare le dinamiche di rilassamento di diversi sistemi nel regime dei femtosecondi. Nella prima parte, abbiamo condotto un'analisi dettagliata dei contributi peculiari della clorofilla *b* isolata. Essa rappresenta infatti uno dei cromofori più diffusi nei complessi antenna. Successivamente, abbiamo sfruttato le conoscenze acquisite dallo studio di un pigmento isolato per indagare la dinamica ultraveloce di un complesso pigmento-proteina naturale, la *Water-Soluble Chlorophyll-binding Protein*. Abbiamo, quindi, sfruttato le conoscenze acquisite sui campioni biologici per

progettare e studiare un nuovo sistema artificiale, più precisamente delle molecole di boro-dipirrometene opportunamente ingegnerizzate per formare un dimero. Infine, per spingere ulteriormente il nostro approccio verso un'effettiva applicazione, abbiamo trattato una nuova implementazione della Spettroscopia Elettronica Bidimensionale, l'*Action-2DES*. Nell'A-2DES, il segnale misurato è una proprietà reale del sistema, che ci permette di operare nelle condizioni reali di lavoro dei dispositivi.

Contents

1 | Introduction

Biomimetics is the study of nature to understand the underlying mechanisms and functions of natural processes and apply them in different scientific fields [1]. The complex architectures of natural structures are mimicked for the development of new artificial technologies [2]. Among the vast variety of biological systems, natural photosynthetic complexes provide an unlimited source of inspiration. The light-harvesting complexes (LHCs) are responsible for capturing the energy from the sunlight and funnelling it to the reaction centres during the very first step of photosynthesis. In the long course of evolution, these systems have developed several strategies and optimized their structures to reach a remarkable efficiency [3]. The structural complexity behind these systems is astonishing: a large number of absorptive molecules are bound into a protein scaffold and carefully positioned to drive the flow of energy in the right direction. Several examples have been proposed for mimicking the efficiency of these LHCs with artificial systems [4], including supramolecular polymers [5–8], self-assembled structures like dendrimers [9, 10], functionalized nanostructures [11, 12] and bioinspired systems [13, 14].
Even if the field of bioinspired molecules appears to be promising, mimicking the features of biological processes is not a trivial task. An interplay between theoretical and experimental research has been devoted to developing novel methods to achieve a full comprehension of all the subtle details. Along this research line, special emphasis has been put on the role of the environment. Numerous efforts have addressed the contributions that the protein scaffold plays in regulating the photophysical properties of the embedded chromophores. In principle, the protein acts as a structural framework that holds the chromophores in specific orientations [15]. However, it is universally recognised that the protein environment also deeply affects the static and dynamical properties of the embedded pigments [16]. Regarding the static effects, it has been observed that changes in the protein conformation or the substitution of specific amino acids can lead to a broadening of the absorption spectra or to a blue/red shift of the absorption maxima [16–19]. Concerning the dynamical aspects, it has been demonstrated that the electrostatic and polarization

effects of the protein acting on the pigments can modulate their interactions, thus influencing the energy transfer rates between chromophores by modifying their electronic couplings [20].
Excitation energy transport (EET) in LHCs depends on the relative strength of the pigment–pigment interaction and the pigment–environment interaction. Depending on which term contributes most, the EET falls in two limit regimes. In one case, when the electronic coupling between pigments is much smaller than the coupling with the environment, the transport falls in an incoherent regime, meaning that localized excitations would hop from pigment to pigment as a classical process. In the opposite case, EET falls in a coherent regime and the excitation results delocalized between molecules, while the effect of the environment can be merely considered as a small perturbation [21–24]. Actually, EET in LHCs has been found to almost always fall in an intermediate regime, meaning that the electronic interactions between pigments are close to the strength of the coupling to the environment vibrational modes [21]. Therefore, the investigation of the energy transport processes is also crucial for studying the complex interplay between coherent and incoherent dynamics. From a theoretical point of view, the combination of quantum and classical methods has allowed the simulation of multichromophoric aggregates in the presence of the protein environment [25, 26], making it possible to obtain increasingly finer details. More recently, also the dynamical role of the protein has been revealed. Indeed, thermal fluctuations and conformational changes of the protein scaffold can affect the efficiency and the robustness of biological machinery [27].
Among all the possible protein-chromophore interactions discussed above, the tuning of the electronic and transport properties of the system can be achieved through the formation of hydrogen(H)-bonds. It has been found that H-bonds stabilize the protein folding [28] and help the binding of the pigments to the protein scaffold [29]. For example, the formation of an H-bond between the Chlorophyll *b* (Chl *b*) formyl group and its protein surroundings seems to play an important role in the stabilization of different LHCs [30]. Moreover, it is reported that the formation of H-bonds between chromophores and the surrounding environment through amino acid residues or water molecules can tune their site energies, modulating the cascade of energy transfer [31].

In a more general framework, H-bonds are fundamental interactions for many biological and artificial systems. This is not surprising considering that they are site-specific interactions, with easily predictable orientations, distances, and geometries. Since its discovery, the nature of the H-bond has been widely investigated by dif-

ferent experimental and theoretical methods. For many years, the research focused on the investigation of H-bond solely considering its structural function. In fact, H-bonds provide most of the directional interactions that promote and assist protein folding, protein structure formation and molecular recognition [32].
Actually, the role of H-bonds is not limited to a mere structural element but plays an important part also in determining the dynamics of photophysical processes. While the ground-state dynamics have been the subject of intense study [33, 34], only in recent years the excited-state hydrogen bonding dynamics has gained more and more attention. Indeed, the photoexcitation of the H-bonded system is rapidly followed by a reorganization of the H-donor and acceptor molecules due to the significant difference in the charge distribution of different electronic states [35]. This reorganization process leads to a weakening or a strengthening of the H-bond in the excited state with respect to the ground state. Thus, it has important implications for the modulation of molecular non-equilibrium processes, significantly affecting the ultrafast excited-state dynamics [36]. Both intra- and inter-molecular hydrogen-bonding interactions are involved in this reorganization. For example, it has been found that intra-molecular H-bonds in donor-bridge-acceptor complexes provide new electronic-coupling pathways for ultrafast charge transfer reactions [37]. Moreover, numerous computational calculations have been dedicated to the investigation of the role of intra-molecular H-bonds on the photophysics of many aromatic systems [38, 39]. On the other side, it has been proved that inter-molecular H-bonds in electronically excited states can significantly facilitate internal conversion, intersystem crossing and intra-molecular charge transfer [40, 41]. The electronic excited state H-bonding dynamics are predominantly determined by the vibrational motions of the hydrogen donor and acceptor groups [40, 42]. The hydrogen-bonding interaction also plays important roles in triplet-triplet energy transfer, as reported for porphyrins systems [43].
Generally, all these processes typically occur on ultrafast time scales of hundreds of femtoseconds. Therefore, to directly monitor the ultrafast dynamical behavior of hydrogen bonds in the excited state, various femtosecond time-resolved spectroscopic techniques have been used [44, 45]. In this context, Two-dimensional Electronic Spectroscopy (2DES) appears to be a particularly suited technique.

Since its development in the late 1990s, 2DES has turned out to be a really powerful technique to follow the ultrafast dynamics in molecules or more complex systems. It consists in collecting the third-order nonlinear polarization signal through multiple interactions between light and matter. 2DES provides information on the

evolution of the system with both high temporal and spectral resolution [46]. The former is strictly linked to the possibility of exciting the system with femtosecond laser pulses, while the latter is achieved by separating and resolving the different components of the final signal as a function of frequency in a 2D-spectrum. As a direct consequence, this technique allows capturing the temporal behavior of both populations and coherences, unrevealing electronic and vibrational couplings and separating inhomogeneous and homogeneous broadening [47]. Moreover, 2DES technique characterizes systems in a non-equilibrium condition, allowing the investigation of excited-state dynamics.
While in the first 2DES applications a non-collinear geometry was preferred, more recently the collinear Action-2DES (A-2DES) technique is quickly gaining ground because of the possibility of switching to the so-called "action detected" techniques. In the collinear configurations, a fourth pulse is added to the pulse sequence to drive the system into an excited state population. The ultrafast dynamics of the system is then retrieved by detecting an incoherent signal proportional to this population, such as fluorescence or photocurrent. These techniques are particularly inspiring in view of characterizing operating devices or realizing ad hoc schemes to answer specific questions. Moreover they can be performed with a much simplified optical setup. For these reasons, action-detected techniques represent one of the most promising developments of multidimensional techniques [48].

This thesis developed in this burgeoning context, with the precise aim of characterizing the excited state dynamics of biological and bioinspired systems. As mentioned above, 2DES represents one of the most suitable spectroscopic techniques to follow the ultrafast dynamics in molecules or more complex systems. Taking advantage of 2DES, particular attention was dedicated to achieving a better understanding of the excitation processes and to ascertain the role of the environment in the relaxation dynamics. Chapter 2 briefly describes the standard spectroscopic methods used to preliminary characterize the systems investigated here. Chapter 3 is entirely devoted to the description of the theoretical background behind a third-order non-linear optical spectroscopy, together with the experimental optical setup used in the 2DES technique and the analysis toolbox developed for data processing and interpretation.
Given the complexity of unravelling the spectroscopic features of each chromophore inside pigment-protein complexes, we first focused on a preliminary investigation of isolated Chlorophyll *b* molecules in solution. Chapter 4 reports a comparative study of the distinctive signatures of Chlorophyll *b* immediately after photexcita-

tion, at room and at cryogenic temperature.
In Chapter 5, we exploited the know-how acquired on isolated chromophores to study the complex interplay between chromophores and the protein environment. In this context, the Water-Soluble Chlorophyll-binding Protein (WSCP) has been chosen as a model system to investigate the importance of specific interactions with the protein scaffold, H-bonds in particular, in tuning the ultrafast relaxation dynamics. These findings suggested the possibility of controlling the photophysics and the transport properties of multichromophores by engineering specific H-bonds. Therefore, by mimicking the key structural elements in WSCP (dimers of chlorophylls and possible formation of H-bonds with protein residues), we engineered and studied new artificial bioinspired systems. This approach is described in Chapter 6, where the dynamics of two functionalized boron dipyrromethene (BODIPY) properly engineered to form a H-bonded dimer is described. In an attempt to push even further the bio-mimetic approach toward the characterization of real energy harvesting devices, the final steps of the research activity consisted in the realization of an A-2DES setup based on photocurrent detection. Chapter 7 thus reports a brief theoretical discussion of the technique, along with the experimental optical setup and the first measurements on a prototypical graphene-based device.

2 | Experimental methods

2.1. Spectroscopic methods

Spectroscopic techniques are based on light-matter interaction. All spectroscopic methods aim to probe the properties of a given material after perturbation with electromagnetic radiation [49]. Different optical setups are employed depending on the optical properties of the material under investigation. However, a clear distinction can be made between standard techniques and advanced spectroscopic methods. The former, like absorption, emission and circular dichroism spectroscopies, rely on conventional and commercial instruments. The latter, like pump-probe spectroscopy or 2DES, require specific and sophisticated homemade setups. In the following sections, more details about the above mentioned techniques are reported. Since the importance of 2DES technique in this work, a separated chapter (Chapter 3) will be dedicated to explain in more detail the theory and all the steps necessary to perform a 2DES experiment.

2.1.1. Standard spectroscopic methods

2.1.1.1. Linear absorption and fluorescence

Steady-state absorption spectroscopy is a widely used linear technique. It measures the intensity of light absorbed by a sample as a function of wavelength. For each wavelength scanned by a monochromator, the absorbance is defined as the minus logarithm of the ratio of the intensity of the light before and after the sample:

$$A(\omega) = -log\frac{I\omega)}{I_0(\omega)} = \varepsilon(\omega)lC \tag{2.1}$$

where $I(\omega)$ and $I_0(\omega)$ are the intensity of light detected after and before the sample, respectively. The absorbance is also linearly related to the optical path l and to the concentration of the sample C through the molar extinction coefficient $\varepsilon(\omega)$ [49]. All

the absorption measurements reported in this work were performed with a Varian Cary 5 spectrometer.
A second standard linear technique is fluorescence spectroscopy, which measures the intensity of light emitted by a sample after excitation. Emission (excitation) spectra are obtained by fixing the excitation (emission) wavelength, while the emission (excitation) wavelength is scanned [50]. The instrument used in this thesis is a FluoroMax 3 spectrometer (Horiba, Jobin Yvon).

2.1.1.2. Circular dichroism

An optically active sample absorbs differently the left- and right-components of an incident circularly polarised light. The difference in the absorption coefficients is called circular dichroism (CD). In a CD measure, the light of a lamp is alternately prepared to be left- and right- circularly polarized by means of a Pockels cell. This modulation is made at a specific frequency so that a lock-in amplifier coupled to the photomultiplier tube can detect only the differential CD effect [49]. CD spectra are measured with a Jasco J-710 spectrometer.

2.1.2. Advanced spectroscopic methods

2.1.2.1. Pump-probe spectroscopy

Pump-probe spectroscopy has been one of the most common non-linear optical techniques since the outbreak of ultrafast lasers. In this technique, the laser pulse is split into a "pump" pulse and a "probe" pulse. The pump beam has a high optical fluence and is used to excite the sample. The probe beam, with a weaker optical fluence, overlaps the pump beam on the sample. The experiment is based on the measurement of the variation of the intensity of the probe beam as a function of the time delay, in the absence and presence of the pump pulse. This variation is then converted into a differential absorption, which is function of the frequency of the probe, to obtain the so-called transient absorption (TA) spectra. The TA spectra are recorded at increasing time delay between the pump and the probe pulse in order to investigate the dynamics of the process [51]. In our experiment, we used a home-built setup represented in Figure 2.1. Briefly, a Ti:Sapphire laser system (Spitfire) generates a train of pulses centred at 800 nm with a repetition rate of 1 kHz and a pulse duration of 150 fs. The output beam is split into two beams using a beam splitter to generate a probe and a pump beam. The pump beam repetition rate is set at 500 Hz

through an optical chopper and its frequency is doubled to 400 nm by means of second harmonic generation (SHG). Simultaneously, probe beam pulses are converted to white-light pulses through super-continuum white light generation in a sapphire crystal. White-light pulses are then split in two beams, one sent to the sample and the other used as reference. Pump and probe beams are overlapped on the sample and the delay between the two is controlled by a retroreflector mounted on a translation stage. The white-light transmission spectrum is recorded by a CCD detector coupled with a diffractive grating. The difference between the transmittance recorded in the presence or absence of pump pulse gives the TA spectra.

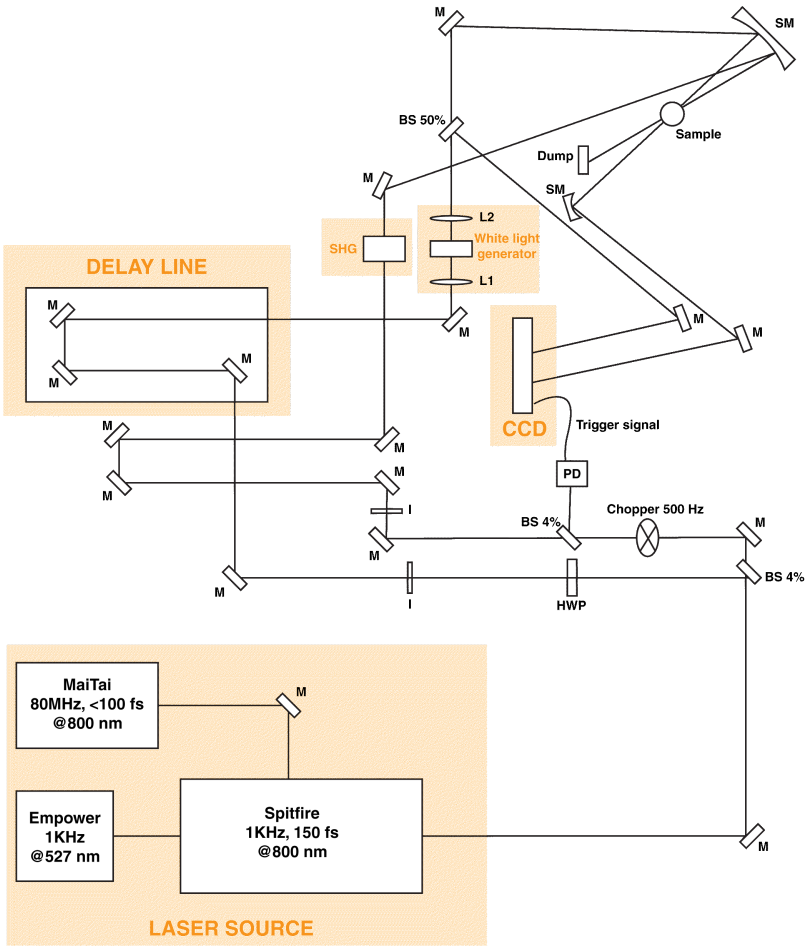

Figure 2.1: Schematic representation of the pump-probe optical setup. Abbreviations: (M) mirror, (SM) spherical mirror, (I) iris, (BS) beam splitter, (HWP) half-wave plate, (L) lens, (PD) photodiode.

3 | 2D-Electronic Spectroscopy

3.1. Theory

In this section, we introduce the theoretical formalism behind Two-Dimensional Electronic Spectroscopy (2DES). In spectroscopy, matter and light are considered as a single system described by a Hamiltonian, given by the sums of three terms:

$$\hat{H} = \hat{H}_M + \hat{H}_L + \hat{H}_{int} \tag{3.1}$$

where $\hat{H}_M$ is the Hamiltonian of matter, $\hat{H}_L$ the Hamiltonian of light and $\hat{H}_{int}$ represents the light-matter interaction. A simplified approach, generally adopted to avoid solving complex mathematical equations, is the semi-classical description. In this approximation, the matter is treated quantum-mechanically, while the light is described classically by Maxwell's equations. The physical observable of a spectroscopic experiment is the macroscopic polarization of the material $P(t)$. The polarization is then used as a source term to obtain the electric field of the signal emitted from the sample. When the system is an isolated molecule, the polarization can be conveniently derived from the wavefunction formalism [51]. However, a real system is composed of an ensemble of interacting molecules and a statistical description is required. In this scenario, a suitable approach is the density matrix formalism, which describes the system as a statistical average. In the following sections, we introduce the density matrix formalism and the principles behind the 2DES technique.

3.1.1. Density matrix formalism

The density matrix formalism is usually adopted when dealing with an ensemble of molecules interacting with the environment, as in condensed phase systems. The

density operator for a statistical mixture of states can be defined as:

$$\hat{\rho}(t) = |\Psi(t)\rangle\langle\Psi(t)| = \sum_k p_k |\Psi_k(t)\rangle\langle\Psi_k(t)| \tag{3.2}$$

with p_k the probabilities of finding the system in the state $\Psi_k(t)$. When all $p_k = 0$ except for one with $p_k = 1$, the system is in a pure state and the wavefunction formalism can be used [51].
Using an arbitrary basis set $|n\rangle$, the wavefunction and the Hermitian conjugate can be expanded as:

$$\begin{aligned} |\Psi(t)\rangle &= \sum_n |n\rangle c_n(t) \\ \langle\Psi(t)| &= \sum_m c_m^*(t)\langle m| \end{aligned} \tag{3.3}$$

and the matrix elements are defined as:

$$\rho_{nm} = \sum_k p_k \langle n|\Psi_k\rangle\langle\Psi_k|m\rangle \tag{3.4}$$

The diagonal matrix elements, for which $m = n$, are called populations and represent the probability of finding the system in the state $|n\rangle$. Off-diagonal elements ($n \neq m$) are named coherences and describe an oscillating probability between two states, with a frequency depending on their energy difference.
One of the main advantage of this formalism is that the expectation value of a generic operator can be expressed as:

$$\langle\hat{A}\rangle = Tr\left[A\rho\right] \tag{3.5}$$

Therefore, it can be simply evaluated by summing diagonal elements (trace), with no reference to the wavefunction.
In this framework, the temporal evolution of a quantum ensemble of states can be described by the density operator only, using the Liouville Von-Neumann equation:

$$\frac{\partial\hat{\rho}(t)}{\partial t} = -\frac{i}{\hbar}\left[\hat{H}(t), \hat{\rho}(t)\right] \tag{3.6}$$

Equation 3.6 can be reformulated in the interaction picture that splits the time dependence both on the Hamiltonian operator and on the density operator:

$$\frac{\partial \hat{\rho}_I(t)}{\partial t} = -\frac{i}{\hbar}\left[\hat{H}_{int,I}(t), \hat{\rho}_I(t)\right] \tag{3.7}$$

A perturbative expansion of the density operator can be performed to solve the time-dependent problem over an ensemble of states. Integrating Equation 3.7 and iteratively substituting, we obtain, in the interaction picture [51]:

$$\begin{aligned}\hat{\rho}_I(t) = \hat{\rho}_I(0) + \sum_{n=1}^{\infty}\left(-\frac{i}{\hbar}\right)^n \int_{t_0}^{t} d\tau_n \int_{t_0}^{\tau_n} d\tau_{n-1} ... \\ ... \int_{t_0}^{\tau_2} d\tau_1 \left[\hat{H}_{int,I}(\tau_n), \left[\hat{H}_{int,I}(\tau_{n-1}), ... \left[\hat{H}_{int,I}(\tau_1), \hat{\rho}_I(t_0)\right) \right] ...\right]\right]\end{aligned} \tag{3.8}$$

Every iterative step can be interpreted as an interaction between light and matter, where the nth term represents the system after n interactions with the electric field.

3.1.2. Response function

The key quantity for the interpretation of a spectroscopic measurement is the macroscopic polarization $P(r,t)$. Its oscillation leads the system to emit a signal in the form of an electromagnetic wave. For a weak electric field, the polarization depends linearly on the electric field E:

$$P = \epsilon_0 \chi^{(1)} E \tag{3.9}$$

where ϵ_0 is the dielectric constant of the vacuum and $\chi^{(1)}$ the linear optical susceptibility of the medium.
However, if the electric field is sufficiently intense, non-linear effects become relevant and the polarization can be expanded:

$$P^{(1)} + P^{(2)} + P^{(3)} + ... = \epsilon_0 \left(\chi^{(1)} E + \chi^{(2)} EE + \chi^{(3)} EEE + ...\right) \tag{3.10}$$

where the term $\chi^{(n)}$ represents the nth-order susceptibility.
The macroscopic polarization can be calculated as the expectation value of the dipole moment operator, $\hat{\mu}$, as:

$$P(t) = Tr\left[\mu\rho(t)\right] = \langle \hat{\mu}\hat{\rho}(t)\rangle \tag{3.11}$$

where μ and ρ are the matrix representations of the respective operator.
For a two-level system in the linear case:

$$\rho = \begin{pmatrix} \rho_{11} & \rho_{12} \\ \rho_{21} & \rho_{22} \end{pmatrix} \qquad \mu = \begin{pmatrix} 0 & \mu_{12} \\ \mu_{21} & 0 \end{pmatrix} \tag{3.12}$$

and the polarization is defined as:

$$P(t) = Tr\left[\begin{pmatrix} 0 & \mu_{12} \\ \mu_{21} & 0 \end{pmatrix}\begin{pmatrix} \rho_{11} & \rho_{12} \\ \rho_{21} & \rho_{22} \end{pmatrix}\right] = \mu_{12}\rho_{21} + \mu_{21}\rho_{12} \tag{3.13}$$

As can be seen from Equation 3.13, the polarization depends only on the off-diagonal elements of the density matrix, which can act as source of electric field. In the interaction picture, the nth-order polarization can be expressed as:

$$P^{(n)}(t) = Tr\left[\mu_I(t)\rho_I^{(n)}(t)\right] \tag{3.14}$$

with $\hat{\mu}_I$ the dipole moment operator in the interaction picture.
Under the dipole approximation, the light-matter interaction Hamiltonian can be described as the product between the dipole moment operator and the total perturbing electric field:

$$\hat{H}_{int,I}(t) = -\hat{\mu}_I(t)E(t) \tag{3.15}$$

In order to obtain a general equation that connects the density matrix operator with the non-linear polarization, we can combine Equations 3.8 and 3.15 into Equation 3.14 to get [51]:

$$\begin{aligned} P^{(n)}(t) = \left(-\frac{i}{\hbar}\right)^n \int_{t_0}^{t} d\tau_n \int_{t_0}^{\tau_n} d\tau_{n-1} \ldots \int_{t_0}^{\tau_2} d\tau_1 E(\tau_n)E(\tau_{n-1}) \ldots E(\tau_1) \\ \times Tr\left[\mu_I(t)\left[\mu_I(\tau_n), [\mu_I(\tau_{n-1}), \ldots [\mu_I(\tau_1), \rho_I(t_0)]\right]\right]\right] \end{aligned} \tag{3.16}$$

This equation allows to connect the macroscopic and the microscopic description of the system. The lowest non-linear term able to provide information on the properties of excited states is the third order. Hence, the first important term in non-liner

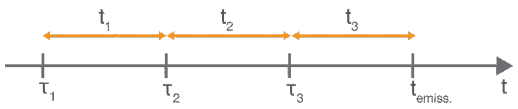

Figure 3.1: Schematic illustration of time ordering of pulses in a third-order spectroscopy. t_1, t_2 and t_3 represent the time interval between interactions, while τ_1, τ_2 and τ_3 denote the absolute time values.

spectroscopy is the third-order polarization:

$$P^{(3)}(t) = \left(-\frac{i}{\hbar}\right)^3 \int_{t_0}^{t} d\tau_3 \int_{t_0}^{\tau_3} d\tau_2 \dots \int_{t_0}^{\tau_2} d\tau_1 E(\tau_3)E(\tau_2)E(\tau_1) \times Tr\left[\mu_I(t)\left[\mu_I(\tau_3),[\mu_I(\tau_2),[\mu_I(\tau_1),\rho_I(t_0)]]\right]\right] \tag{3.17}$$

In order to simplify this equation, we assume that $\rho_I(t_0)$ is the equilibrium density matrix, not evolving in time under the influence of the Hamiltonian, so that t_0 can be set to $(-\infty)$. Moreover, a change of variables can be done by setting:

$$\begin{aligned} \tau_1 &= 0 \\ t_1 &= \tau_2 - \tau_1 \\ t_2 &= \tau_3 - \tau_2 \\ t_3 &= t - \tau_3 \end{aligned} \tag{3.18}$$

where τ_n denotes the absolute time points of light-molecules interactions, while t_n represents the time intervals between these interactions (see Figure 3.1).
The resulting third-order polarization becomes:

$$P^{(3)}(t) = \int_0^\infty dt_3 \int_0^\infty dt_2 \int_0^\infty dt_1 E(t-t_3)E(t-t_3-t_2)E(t-t_3-t_2-t_1)S^{(3)}(t_3,t_2,t_1) \tag{3.19}$$

where we introduce the third-order optical response function $S^{(3)}(t_{1,},t_2,t_3)$ defined as:

$$S^{(3)}(t_3,t_2,t_1) = \left(-\frac{i}{\hbar}\right)^3 Tr\left[\mu_I(t_3+t_2+t_1)\left[\mu_I(t_2+t_1),[\mu_I(t_1),[\mu_I(0),\rho(-\infty)]]\right]\right] \tag{3.20}$$

The interactions at time 0, t_1 and (t_2+t_1) generate the non-equilibrium density matrix $\rho^{(3)}$, whose off-diagonal elements emit an electric field at time $(t_3+t_2+t_1)$, that is the spectroscopic signal.

By explicitly calculating the commutator, we obtain all the possible evolution pathways, called Liouville pathways, that the system can follow:

$$S^{(3)}(t_3, t_2, t_1) = \left(-\frac{i}{\hbar}\right)^3 \sum_{j=1}^{4} \left(R_j - R_j^*\right) \tag{3.21}$$

that for the third-order response function are 8, in pairs of conjugate complex:

$$\begin{aligned}
R_1 &= Tr\left[\mu_I(t_3+t_2+t_1)\mu_I(0)\rho(-\infty)\mu_I(t_1)\mu_I(t_2+t_1)\right] \\
R_1^* &= Tr\left[\mu_I(t_3+t_2+t_1)\mu_I(t_2+t_1)\mu_I(t_1)\rho(-\infty)\mu_I(0)\right] \\
R_2 &= Tr\left[\mu_I(t_3+t_2+t_1)\mu_I(t_1)\rho(-\infty)\mu_I(0)\mu_I(t_2+t_1)\right] \\
R_2^* &= Tr\left[\mu_I(t_3+t_2+t_1)\mu_I(t_2+t_1)\mu_I(0)\rho(-\infty)\mu_I(t_1)\right] \\
R_3 &= Tr\left[\mu_I(t_3+t_2+t_1)\mu_I(t_2+t_1)\rho(-\infty)\mu_I(0)\mu_I(t_1)\right] \\
R_3^* &= Tr\left[\mu_I(t_3+t_2+t_1)\mu_I(t_1)\mu_I(0)\rho(-\infty)\mu_I(t_2+t_1)\right] \\
R_4 &= Tr\left[\mu_I(t_3+t_2+t_1)\mu_I(t_2+t_1)\mu_I(t_1)\mu_I(0)\rho(-\infty)\right] \\
R_4^* &= Tr\left[\mu_I(t_3+t_2+t_1)\rho(-\infty)\mu_I(0)\mu_I(t_1)\mu_I(t_2+t_1)\right]
\end{aligned} \tag{3.22}$$

where R_j^* is the conjugate complex of R_j and, by convention, the last interaction of all the terms is written as emitted from the ket. The amount of terms in the response function exponentially grows as the number of interactions between light and matter increases. Indeed, the 8 terms of the non-linear response function are further split by the electric field, as described in Equation 3.19. Since the total external field is given by three laser pulses, the total third-order signal includes 864 terms. Thus, some approximations are introduced to have just four independent terms. The approximations are the following:

(i) **Time ordering**: laser pulses are shorter in time than the time interval between them, so they do not overlap in time and each interaction can be assigned to a specific ordered laser pulse.

(ii) **Phase matching**: the wavevector of the emitted signal is given by a combination of the wavevectors of the incident beams:

$$\vec{k}_{sign} = \sum_{n=1}^{3} \pm \vec{k}_n \tag{3.23}$$

Therefore, it is possible to distinguish between different Liouville pathways just by selecting the exciting geometry of the experimental setup.

(iii) **Rotating Wave Approximation**: applying this approximation, only terms with either positive or negative frequencies will contribute to the response function, but not both, because components with the same sign are highly oscillatory and can be neglected. So, the central frequency of the emitted signal can be determined as:

$$\omega_{sign} = \sum_{n=1}^{3} \pm\omega_n \tag{3.24}$$

A physical interpretation of these contributions can be evaluated using a more visual instrument, namely Feynman diagrams, described in the next section.

3.1.3. Double-sided Feynman diagrams

Double-sided Feynman diagrams are a powerful visual tool to identify the Liouville pathways that correspond to the nth-order signals. Each diagram is built following precise rules, here illustrated:

(i) vertical axes depict the time evolution of ket and bra states, with ket drawn on the left and bra on the right. Time is running from the bottom to the top.

(ii) each interaction with the electric field is represented by an arrow. The last interaction, which accounts for the emission of the signal from the sample, is indicated with a wavy arrow and by convention drawn on the left of the diagram (on the right in the case of the conjugate complex).

(iii) an arrow pointing to the left represents an interaction with a positive frequency field while an arrow pointing to the right represents an interaction with a negative electric field.

(iv) an arrow pointing toward the system accounts for absorption interaction while an arrow pointing away represents an emission interaction. The last interaction corresponds to an emission of light, so it always points away from the system.

(v) before the first interaction, the system is in equilibrium in the ground state. After the last interaction, the system is in a pure state (ground or excited).

As outlined in the above section, only four terms (and their complex conjugates) are necessary to describe the third-order response function, corresponding to the Feynman diagrams in Figure 3.2.

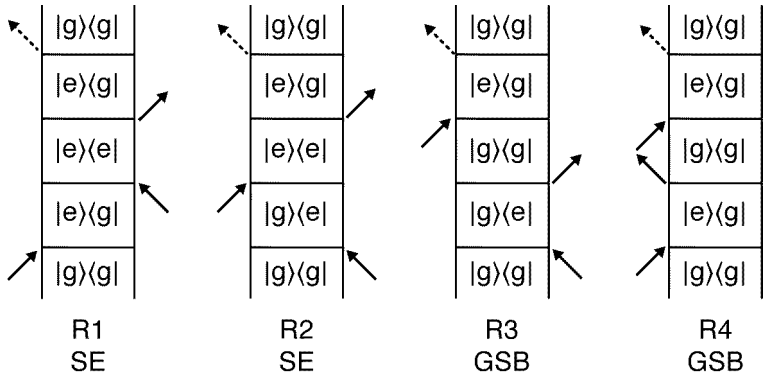

Figure 3.2: Feynman paths summarizing all the possible contributions to the third order response function in a two level system. R_1 and R_2 represent the process of stimulated emission, while R_3 and R_4 are ground state bleaching pathways.

R_1 and R_2 Feynamn pathways correspond to the stimulated emission (SE) process. The first two pulses generate an excited state population $|e\rangle\langle e|$ and, after the third interaction, the system emits the third-order signal. They represent the ideal terms to study the evolution of the excited state along t_2. R_3 and R_4 Feynman pathways correspond to ground state bleaching (GSB) process, where the evolution of the ground state along t_2 is monitored.

Experimentally, different contributions from the total signal can be separated since signals originating from different Liouville pathways are emitted in different directions. Indeed, $R_2$and R_3 terms can be collected separately from $R_1$and R_4 by tuning the phase-matching direction. Signal wavevectors are given by two different combinations:

$$\begin{aligned} \vec{k}^{R}_{sign} &= -\vec{k}_1 + \vec{k}_2 + \vec{k}_3 \\ \vec{k}^{NR}_{sign} &= +\vec{k}_1 - \vec{k}_2 + \vec{k}_3 \end{aligned} \tag{3.25}$$

The signal generated along $\vec{k}^{R}_{sign}$ direction is addressed as rephasing (R) signal, while the signal generated in $\vec{k}^{NR}_{sign}$ direction is labelled as non-rephasing (NR) signal. This terminology arises from the different behaviour of the two terms along t_1 and t_3. Indeed, in rephasing paths, the phase of the signal evolves at conjugate frequency during the two time intervals, while in non-rephasing paths it evolves with the same frequency. In addition, summing up the real parts of the rephasing and the non-rephasing signal, we obtain the purely absorptive (or total) signal.

The time intervals between subsequent interactions are known with specific names. t_1 is called coherence time, because ground and excited state are in a coherence after the first interaction, t_2 is known as population time because the system evolves in a pure state (a population) during this time delay, while t_3 is the rephasing time

because it is the time interval needed to collect signals.
Another contribution to consider is the excited state absorption (ESA) process, where the last interaction generates an excited state population. As for the SE signal, the first two interactions populate the excited state but the third interaction stimulates an absorption to a higher excited state. For this reason, signals originating from ESA paths are always negative, while SE and GSB pathways give rise to positive signals. ESA terms contribute to both rephasing and non-rephasing phase matching conditions.

3.1.4. Relaxation process and spectral lineshapes

In spectroscopic experiments we usually deal with a statistical ensemble of molecules. Each molecule of this system is surrounded by a different local environment that affects its properties, resulting in a dynamic distribution of frequencies and phases of the oscillations and in a static distribution of the resonance frequencies. For this reason, the macroscopic polarization is eventually damped.
The effects of the environment in the 2DES spectra can be explained with the lineshape function formalism [51, 52], where all the information connected to system-bath coupling is included in a function $g(t)$.
For simplicity, this formalism is illustrated here for the linear optical response. The absorption spectrum $A(\omega)$ is proportional to the electric field emitted by the off-diagonal elements of the density matrix, which, in turn, is proportional to the first order polarization induced in the system. It is possible to demonstrate that the absorption spectrum is proportional to the Fourier transform (FT) of the time evolution of the correlation function of dipole moments [51]:

$$\begin{aligned} A(\omega) \propto \mathfrak{R}\left\{\int_0^\infty dt\, e^{-i\omega t}\, Tr\left[\mu_I(t)\mu_I(0)\rho(-\infty)\right]\right\} = \\ = \mathfrak{R}\left\{\int_0^\infty dt\, e^{-i\omega t}\, Tr\left[\mu_{ab}(t)\mu_{ab}(0)\rho_{ab}\right]\right\} \end{aligned} \tag{3.26}$$

Equation 3.26 describes the situation in which the radiation is in resonance with the transition between two states a and b of the system. In the case of an isolated system, the coherences generated by the external electric field will oscillate indefinitely at the resonance frequency ω_{ab} and the corresponding spectrum can be described by a $\delta-$function:

$$A(\omega) \propto \mathfrak{R}\left\{\int_0^\infty dt\, e^{-i\omega t} e^{i\omega_{ab} t}\right\} = 2\pi\delta(\omega_{ab} - \omega) \tag{3.27}$$

However, in real systems, the situation is complicated by the fact that each molecule can interact with the surrounding environment, i.e., with other molecules or with the solvent; in such cases, the system is characterized by a static distribution of slightly different transition frequencies ω_{ab}, described by a Gaussian function. Therefore, ω_{ab} becomes time-dependent and the absorption spectrum takes the form:

$$A(\omega) \propto \Re \int_0^\infty dt\, e^{-i\omega t} e^{i\int_0^t d\tau\, \omega_{ab}(\tau)} \tag{3.28}$$

The frequency $\omega_{ab}(\tau)$ can be separated into two parts: its time-independent average frequency $\overline{\omega}_{ab}$ and a time-dependent deviation $\delta\omega_{ab}(t)$, so $\omega_{ab}(\tau) = \overline{\omega}_{ab} + \delta\omega_{ab}(\tau)$; therefore, Equation 3.28 can be rewritten as:

$$A(\omega) \propto \Re \int_0^\infty dt\, e^{-i\omega t} e^{i\bar{\omega}_{ab}t} e^{i\int_0^t d\tau\, \omega_{ab}(\tau)} \tag{3.29}$$

Moreover, $\delta\omega_{ab}(\tau)$ can be expanded in power-series, also called cummulant expansion, to obtain, after proper approximations [51]:

$$A(\omega) \propto \Re \int_0^\infty dt\, e^{-i\omega t} e^{i\bar{\omega}_{ab}t} e^{-g(t)} \tag{3.30}$$

where $g(t)$ is the lineshape function, defined as the correlation function of $\delta\omega$:

$$g(t) = \int_0^t \int_0^{\tau'} d\tau'\, d\tau''\ \langle \delta\omega(\tau'')\delta\omega(0)\rangle \tag{3.31}$$

The correlation function $g(t)$ can be modeled with an exponential function [51]:

$$\langle \delta\omega(t)\delta\omega(0)\rangle = \Delta^2 e^{-\frac{t}{\tau_c}} \tag{3.32}$$

which depends on two parameters, the correlation time τ_c and the fluctuation amplitude $\Delta = \delta\omega$.
Integrating the correlation function $g(t)$ twice, we obtain the so-called Kubo-lineshape function [53, 54]:

$$g(t) = \Delta^2 \tau_c^2 \left[e^{-\frac{t}{\tau_c}} + \frac{t}{\tau_c} - 1 \right] \tag{3.33}$$

This model takes into account all the possible broadening mechanisms and can be discussed for two possible limiting situations. If τ_c is longer than the molecular relaxation timescales, $g(t)$ can be associated with static or inhomogeneous broadening:

the molecules of the ensemble have a static distribution of resonance frequencies, due to different local surroundings, but they do not fluctuate. In this case, $g(t)$ can be approximated as:

$$g(t) = \frac{\Delta^2 t^2}{2} \tag{3.34}$$

with the absorption spectrum:

$$\begin{aligned} A(\omega) &\propto \Re \int_0^\infty dt\, e^{-i\omega t} e^{i\bar{\omega}_{ab} t} e^{-\frac{\Delta^2 t^2}{2}} \\ &= \sqrt{\frac{2\pi}{\Delta^2}} exp\left(-\frac{(\omega - \overline{\omega}_{ab})^2}{2\Delta^2}\right) \end{aligned} \tag{3.35}$$

This situation yields to a Gaussian function centered to $\overline{\omega}_{ab}$,with spectral width equal to Δ; the absorption spectrum shows the energy distribution of the molecules in the ensemble.

If τ_c is shorter than the molecular relaxation timescales, the dynamic homogeneous broadening situation is obtained: molecules are subjected to rapid fluctuations in phase and changes in frequency in the entire range of Δ. In this case, the lineshape function can be defined as:

$$g(t) = \Delta^2 \tau_c t = \frac{t}{T_2} = \Gamma t \tag{3.36}$$

where $\Delta^2 \tau_c = \frac{1}{T_2} = \Gamma$ is the decay constant that describes the damping of the oscillation between states *a* and *b*. It includes contributions from the decay constant of the excited state (T_1) and the pure dephasing time (T_2^*):

$$\Gamma = \frac{1}{T_2} = \frac{1}{2T_1} + \frac{1}{T_2^*} \tag{3.37}$$

where the first term accounts for the loss of population of the excited state and the second one describes the phase randomization of the oscillation between the two states. The absorption spectrum becomes:

$$\begin{aligned} A(\omega) &\propto \Re \int_0^\infty dt\, e^{-i\omega t} e^{i\bar{\omega}_{ab} t} e^{-\Gamma t} \\ &= \frac{2\Gamma}{(\omega - \overline{\omega}_{ab}) + \Gamma^2} \end{aligned} \tag{3.38}$$

which is a Lorentzian function centered at frequency $\overline{\omega}_{ab}$.
In general, real systems lie between these two limits. Every molecule has its own instantaneous frequency, which evolves over time as the system interacts with the surroundings. This process is also known as spectral diffusion. In this case, the spectral shape is the convolution of Lorentzian and Gaussian distributions, resulting in a Voigt profile.
The treatment outlined above can be generalized for higher-order signals and can be used for the calculation of the response function of any order of polarization.
It should also be noted that, besides the Kubo's lineshape model, other models for the description of $g(t)$ can be used, depending on what is considered.

3.1.5. 2D Electronic Spectroscopy

In a 2DES experiment, the final signal is measured as a function of the time delays between the three exciting pulses, $Sig^{(3)}(t_1, t_2, t_3)$. In order to obtain the signal in a more intuitive form, the time domains t_1 and t_3 are usually Fourier-transformed:

$$Sig^{(3)}(\omega_1, t_2, \omega_3) = \int \int_{-\infty}^{+\infty} dt_1 dt_2 Sig^{(3)}(t_1, t_2, t_3)\, e^{-i\omega_1 t_1}\, e^{-i\omega_3 t_3} \tag{3.39}$$

The information encoded by the signal can now be more easily visualized in the form of a two-dimensional frequency-frequency map evolving along the population time, where the x and y-axis correspond to the excitation frequency ω_1 and to the emission frequency ω_3, respectively. The axis ω_1 contains information about the first excited coherence, hence about the energies of the states involved in the transition, whereas the axis ω_3 contains information about the second optical coherence. Finally, information on the dynamics can be retrieved by looking at how the 2D-map evolves during the population time.
Fluctuations introduce broadening in the features of 2D spectra, but a great advantage of 2DES technique is the possibility of distinguishing homogeneous from inhomogeneous broadening: in a rephasing spectrum, at early population times, the inhomogeneous broadening can be recovered along the diagonal, while the homogeneous broadening appears along the anti-diagonal.
To better understand the nature of different signals appearing in the spectra, it is useful to identify the different Feynman paths contributing to the signal. Diagonal peaks in the 2DES maps can be associated with GSB and SE signals, accounting for the evolution of population dynamics of ground and excited states, respectively.

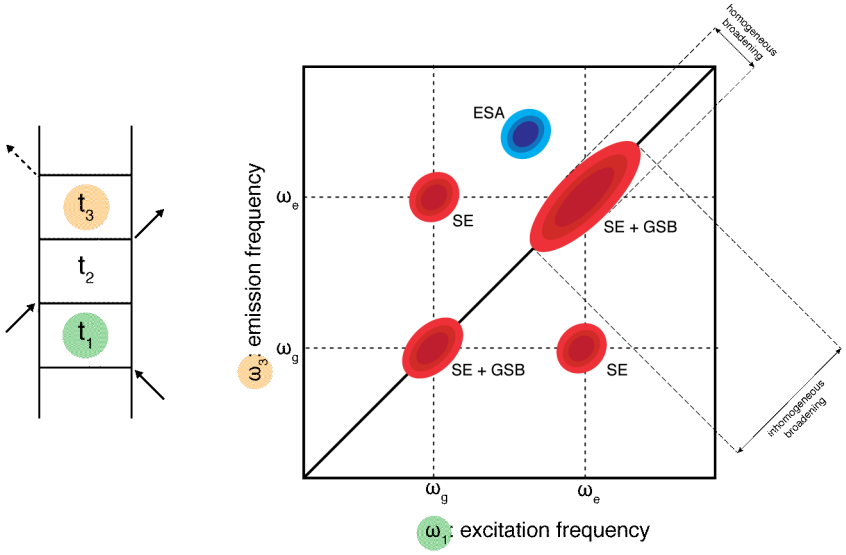

Figure 3.3: Structure of a 2D frequency-frequency map for a given t_2 value, where ω_1 and ω_3 are the Fourier-transforms of t_1 and t_3, respectively. The intensity of the signals appears in the maps with a color scale: red peaks are positive (GSB+SE) and blue ones are negative (ESA). The shape of the peaks can reveal the presence of inhomogeneous broadening (elongation along the diagonal) and homogeneous broadening (anti-diagonal direction).

Off-diagonal peaks are instead due to SE and ESA pathways. ESA signal often appears at emission frequency higher than excitation frequency, while SE signal is located symmetrically in the anti-diagonal direction. SE and GSB signals are positive, while ESA signals give a negative contribution, as summarized in Figure 3.3.

The relaxation between energy levels or energy transfer between different molecules result in the formation of rising cross-peaks below the diagonal with simultaneous decay of the diagonal signals associated with the initial states. Excitation and emission coordinates of the cross-peaks provide direct information on the energy of the involved states.

Until now, no assumption has been made about the nature of the excited states, namely they could both represent electronic or vibrational states. The following section explains how to distinguish coherences between states of different nature.

3.1.5.1. Signal beatings: electronic and vibrational contributions

In rephasing and non-rephasing signals, several beatings are expected along the population time. Depending on the character of the involved states, vibrational or electronic coherences can be distinguished. Thus, the interpretation of 2D spectra requires an accurate analysis of the complex pattern of oscillations emerging from the spectroscopic signal. In molecules and their aggregates, vibronic contributions

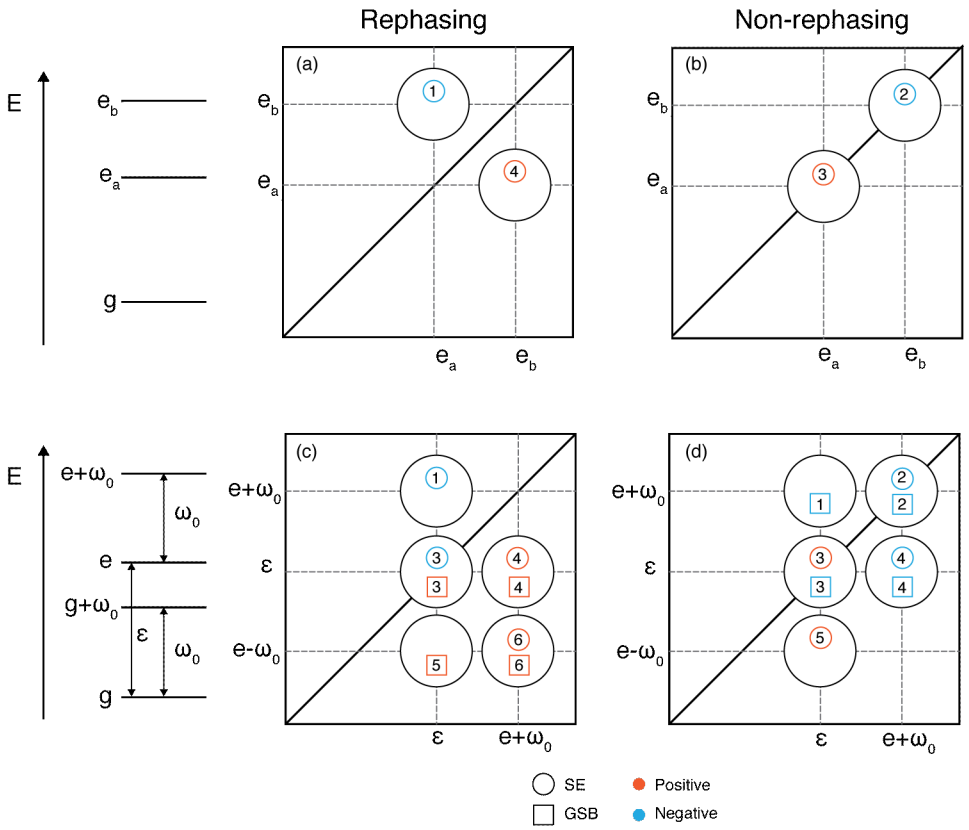

Figure 3.4: Diagrammatic scheme showing the amplitude pattern for (a,b) electronic coherences and (c,d) vibrational coherences. The energy levels are labeled with g and e for ground and electronic states respectively, whereas the vibrational quantum is ω_0. GSB signal is indicated with square and SE signal with circle; the numbers serve as references for Figure 3.5 and Figure 3.6. Positive and negative frequency contributions are marked with red and blue color, respectively. Panels (a,c) represent the expected pattern for rephasing signals, whereas panels (b,d) refer to non-rephasing signals.

emerge from the coupling of electronic transitions with vibrational modes. These vibrational modes have energies in the order of 100 - 3000 cm^{-1}, which are in the same order of magnitude of excitonic couplings and of electronic energy gaps in aggregates. From that, it follows that vibronic and excitonic systems show spectroscopic similarities, which can complicate the interpretation of coherent beatings in 2D spectra. Moreover, since femtosecond laser pulses used in 2DES have a spectral bandwidth in the order of thousand of cm^{-1}, also different electronic transitions could be excited simultaneously.

For this purpose, two models with different internal coherent dynamics can be used to distinguish between electronic and vibrational contributions [55]. Figure 3.4 shows the different pattern for rephasing and non-rephasing signals.

Electronic coherences have 4 oscillatory contributions, two in the rephasing spectra and two in the non-rephasing. These beatings appear at cross-peaks ($\varepsilon_\alpha, \varepsilon_\beta$) and

$(\varepsilon_\beta, \varepsilon_\alpha)$ in the rephasing experiment and on the diagonal coordinates $(\varepsilon_\alpha, \varepsilon_\alpha)$ and $(\varepsilon_\beta, \varepsilon_\beta)$ in the non-rephasing experiment.
Assuming the most common displaced harmonic oscillator picture, the distribution of the vibrational coherences in rephasing spectra is usually referred as 'chair pattern', since it recalls features of a chair. In non rephasing spectra, instead, the distribution is flipped upside-down. In rephasing spectra the signal occurring at coordinates $(\varepsilon + \omega_0, \varepsilon - \omega_0)$ has oscillating character, while at $(\varepsilon + \omega_0, \varepsilon + \omega_0)$ it has not. The opposite happens in non rephasing spectra. However, it must be taken into account that in a realistic system more than one vibrational mode can be coupled to an electronic transition and so, also other components oscillating at frequency ω_x appear in the maps at coordinates $(\varepsilon \pm \omega_x)$. Electronic and vibrational coherences can also be discerned by the timescale of their dynamics. Electronic coherences generally last for tens of femtoseconds and are strongly influenced by temperature and environmental fluctuations; on the other hand, vibrational coherences can survive for longer times, also several picoseconds, because are less affected by inhomogeneity and fluctuations.

3.2. Setup

The experimental acquisition of 2DES measurements requires a specific pulse geometry. A wide range of experimental configurations have been proposed but three main groups can be identified: (i) fully collinear geometry, where all the pulses have the same direction, (ii) partially non-collinear geometry, in which two of the pulses have the same direction and one is tilted of a small angle [56], and (iii) fully non-collinear geometry, where all the pulses have different directions. All implementations have their advantages and disadvantages [57]. Our 2DES experiments are performed with a fully non-collinear BOXCARS geometry, based on the setup proposed by Hauer *et al.* [58] and subsequently improved [59], where the three laser pulses propagate parallel along the vertices of an imaginary square before being focalized on the sample. This setup has many advantages like: the use of one diffractive optic element to generate all the beam replicas; the high signal-to-noise ratio due to the background free direction of detection; the possibility of acquiring the different contributions to the signal (rephasing and non-rephasing) thanks to the independent scan of each beam delay. However, it often lacks of phase stability and requires a phasing procedure, as the phase relation among pulses changes when they pass through the wedges. In the following sections, the main elements of the setup are

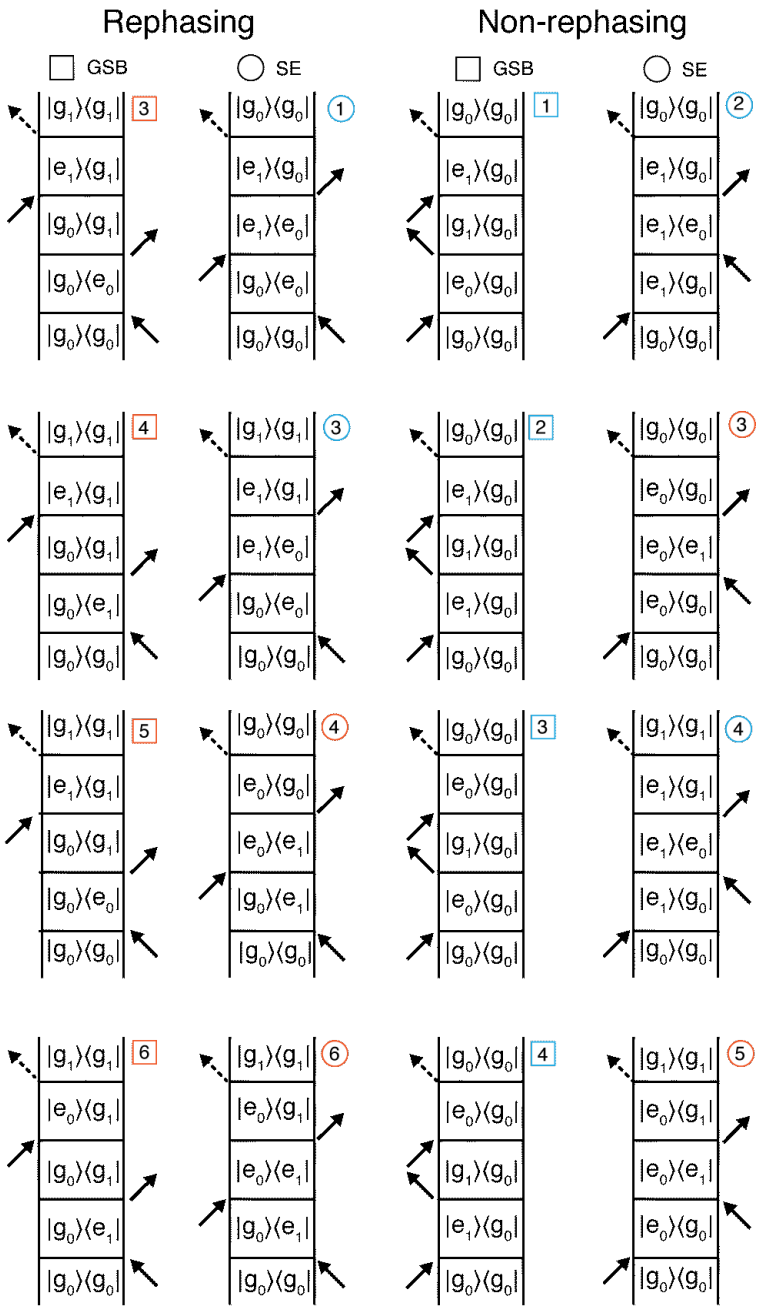

Figure 3.5: Feynman diagrams for vibrational coherences. The numbers indicate specific coordinates of the maps in Figure 3.4 panels (c,d).

illustrated, along with the crucial steps necessary to perform the experiment.

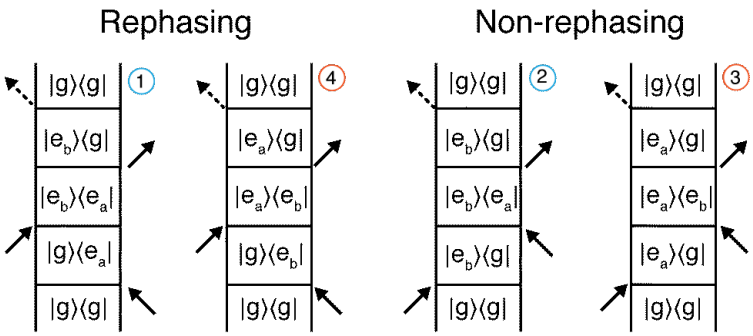

Figure 3.6: Feynman diagrams for electronic coherences.The numbers indicate specific coordinates of the maps in Figure 3.4 panels (a,b).

3.2.1. Optical setup

A schematic representation of the 2DES setup is shown in Figure 3.7.
A Coherent® Libra laser system generates pulses at a repetition rate of 3 kHz and centred at 800 nm. The outcoming pulses have a time duration of about 100 fs and a bandwidth of about 12 nm.
A GuideStar® beam stabilizer system compensates for possible beam position drifts. The central wavelength of the outcoming pulses is converted from 800 nm in the visible range by a commercial non-collinear optical parametric amplifier (NOPA) (Light Conversion® Topas White). The maximum achievable bandwidth depends on the selected central wavelength but it is typically on the order of 80-100 nm.
Before entering the optical setup, the pulses from the NOPA pass through a pulse shaping and a prism compressor stage, to maximize the time resolution and to achieve complete control of the phase of the different spectral components of the broadband pulses. A comprehensive explanation of the compression and shaping stage is reported in section 3.2.2.
The pulse is split into four identical beams in the BOXCARS geometry, by focusing the incoming beam in a 2D diffractive optic element (DOE) with the spherical mirror (SM3). The outgoing divergent beams are then collimated and parallelized by a doughnut-shaped spherical mirror (DSM1).
The variable time delays between the three exciting pulses are introduced by the use of couples of antiparallel 4° CaF_2 25 mm long wedges (WP). One wedge of each pair is mounted on a translational stage (Aerotech® Ant95), whose position is computer-controlled. The choice of CaF_2 ensures to induce less phase distortion in broadband pulses. With this configuration, the precision of the time delays between the pulses is about 0.07 fs, even with long scanning times. The fourth pulse is used as a lo-

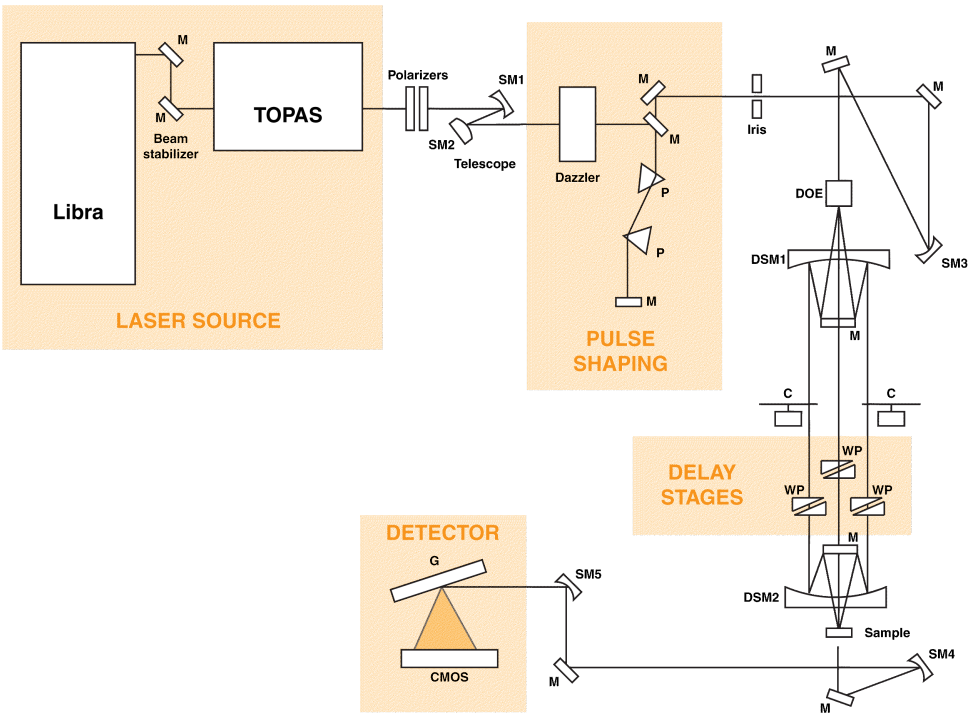

Figure 3.7: Schematic representation of the 2DES optical setup. Abbreviations: (M) mirror, (SM) spherical mirror,(P) prism, (DOE) diffractive optical element, (DSM) doughnut spherical mirror, (C) optical chopper, (WP) wedge pair, (G) grating.

cal oscillator (LO), for heterodyne detection, and attenuated by a graduated neutral density filter to maximize the heterodyne signal. The four beams are focused onto the sample by DSM2.

The third-order signal is emitted in the LO direction and the signal-LO interference is delivered to the spectrograph (Andor® Shamrock 303i) equipped with a sCMOS (scientific Complementary Metal-Oxide Semiconductor) camera (Andor Solis-Newton®).

3.2.2. Compression and shaping stage

The pulse duration is directly linked to the time resolution of a 2DES experiment. A shorter pulse ensures a better time resolution. The pulse duration depends on the bandwidth of the laser spectrum and on the phases of its spectral components. For a given bandwidth, the shortest achievable pulse is called transform-limited (TL) pulse. A TL pulse is obtained when the phase of the pulse shows only a linear dependence with the frequency. The laser field of a pulse can be written as:

$$E(t,\omega) = S(\omega) \cdot e^{i(\omega_0 t)+\phi(\omega))} \tag{3.40}$$

where S_ω is the spectral shape, ω_0 is the central frequency of the laser spectrum and $\phi(\omega)$ is the phase function. The frequency dependence on the phase can be expressed with a Taylor series expansion around ω_0 and truncated at the fourth order:

$$\begin{aligned}\phi(\omega) = \phi(\omega_0) + \left(\frac{d\phi}{d\omega}\right)_{\omega_0}(\omega-\omega_0)+ \\ +\frac{1}{2}\left(\frac{d^2\phi}{d\omega^2}\right)_{\omega_0}+(\omega-\omega_0)^2+ \\ +\frac{1}{6}\left(\frac{d^3\phi}{d\omega^3}\right)_{\omega_0}+(\omega-\omega_0)^3+ \\ +\frac{1}{24}\left(\frac{d^4\phi}{d\omega^4}\right)_{\omega_0}+(\omega-\omega_0)^4\end{aligned} \tag{3.41}$$

Different orders describe different properties of the temporal profile of the pulse. The first order term is related to the arrival time of the pulse. The second order describes the linear chirp, while higher terms describe phase distortions with point (even orders) or axial (odd orders) symmetry with respect to ω_0 [60]. When a broadband pulse passes through an optical material with a non-constant refractive index that changes as a function of the wavelengths, the different frequency components in the pulse propagate in the medium with different speed, i.e., the red component travels faster than the blue one. For this reason, each component acquires a different phase and the pulse duration increases. Non-linear deviations, correlated to phase distortions, must be compensated before any experiment because it is reported that they affect the final shapes of the 2DES maps [61, 62].

In our setup, these corrections are performed by two systems: a prism compressor and an acousto-optic programmable dispersive filter (AOPDF, Fastlite® Dazzler), briefly described below. The AOPDF is a small device containing an acoustic-optic crystal and a piezoelectric device that generates acoustic waves. The TL pulse can be obtained by estimating the coefficients of the terms of the Taylor expansion and cancelling them *via* the AOPDF. The performances of the AOPDF are complemented by a standard prism compressor formed by a couple of transparent prisms made of SF11, a material whose refractive index is wavelength dependent. The linear chirp can be corrected by adjusting the distance and the relative angle between the prisms.

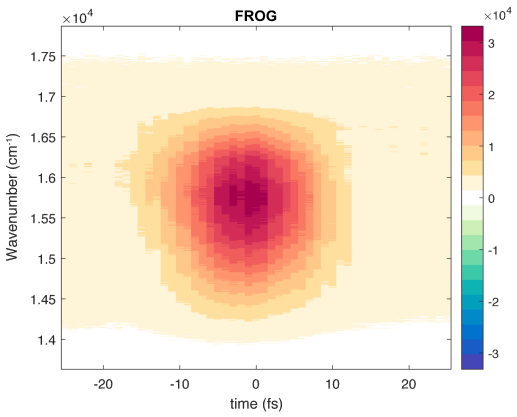

Figure 3.8: Example of an experimental FROG signal recorded as a function of scanned time delays and of the frequencies recorded by the camera.

3.2.3. FROG

Frequency-Resolved Optical Gating (FROG) technique is used to measure the pulse profile. FROG consists in spectrally resolving the signal beam of an autocorrelation measurement [63]. In our setup, we exploit the BOXCARS geometry to perform FROG by replacing the sample with a non-zero third order material, usually DMSO. The use of the same cuvette for the sample and the DMSO guarantees identical operating conditions in 2DES and FROG measurements, thus retaining the same pulse properties in the two experiments. In FROG, two of the pulses are overlapped in space and kept fixed at time zero, while the third pulse is scanned from negative to positive delays. The interference between the first and the second pulse acts as a grating for the third pulse, which is diffracted and recorded with the camera in the signal direction. A time-frequency map is registered as a function of the scanned delay times and of the frequencies recorded by the camera (Figure 3.8). The width of the signal along the x-direction provides the time duration of the pulse for each frequency, while the width of the signal along the y-axis represents the frequency spectrum of the pulse. For a TL pulse, the maximum signal is generated when the three pulses are superimposed in time. Different distortions can affect the shape of a FROG signal caused by changes of the coefficients of the second, third and fourth-order terms of the Taylor expansion in Equation (3.41). In order to have a pulse duration as short as possible, FROG measures are iteratively performed while changing the coefficients of the different terms of Equation (3.41) via the AOPDF and checking the FROG result until the best temporal resolution is found.

3.2.4. Time delays calibration

In non-collinear 2DES experiments, the phase of the final signal is a linear combination of the phases of all the pulses. In our setup, the time delay between exciting pulses is controlled by translation stages that adjust the wedges position and the amount of CaF_2 that the pulses pass through. To obtain meaningful 2DES spectra, the accuracy of the translation stage should be good enough to conserve the phase difference between the pulses in the entire scanned time range.
In our procedure, a linear relation associates the position x_i (in mm) of the i^{th} stage, and thus the position of the wedge, with the time delay τ_i (in fs) of the i^{th} pulse:

$$\tau_i(x_i) = c_i(x_i - z_i) \tag{3.42}$$

where c_i is the linear calibration coefficient (fs/mm) to be determined. $\tau_i(x_i)$ is calculated with respect to the time zero of the experiment, i.e. when all the linear stages are in the position z_i which ensures an equal time delay of all the exciting pulses from LO.
The calibration procedure allows us to retrieve (i) the time zero of the experiment, namely the positions z_i of the three linear stages that satisfy the condition: $\tau_i(z_i) = 0$ fs; (ii) find the linear coefficients c_i to convert a displacement of the stage in a time delay from the zero of the experiment. The overall calibration method in detail is reported in [59] and resolves some of the most important issues of non-collinear 2DES setups [64], crucial to obtaining high quality 2DES data.

3.2.5. Phase matching

In a BOXCARS 2DES experiment, the propagation of the exciting beams at the three vertices of a square is crucial to generating the third-order signal along the fourth vertex, corresponding to the LO propagation direction. For this reason, the four beams should be carefully aligned in order to avoid deviations of even small angles, which could produce artefacts in the measured signal. The optical WP used to time delay the pulses represents a critical factor and could induce deviations if not properly aligned. The procedure employed to correct this deviation consists of two steps. First, the four beams position is recorded on a portable camera and the setup is perfectly aligned without wedges. Then, the wedges are placed on the translational stages and deviations from the previous beams' path are corrected by slightly rotating the wedges along both the horizontal and vertical axes. Finally, the transla-

tional stages are moved along their entire length and the conservation of the beams position is checked to ensure that the phase-matching condition will be preserved during a 2DES measurement.

3.2.6. Time scan definition

In our 2DES setup, we have an independent control on the scan of each pulse, meaning that we can scan all the different time delays of the three exciting pulses. Since the phase of the heterodyne detected signals can be expressed as a combination of the phases of each pulse:

$$\begin{aligned} \phi^{R}_{signal} &= -\phi_1 + \phi_2 + \phi_3 - \phi_{LO} \\ \phi^{NR}_{signal} &= +\phi_1 - \phi_2 + \phi_3 - \phi_{LO} \end{aligned} \tag{3.43}$$

the most convenient configuration to perform a 2DES experiment consists in fixing the time delay between the third beam and LO. The remaining two pulses are scanned simultaneously to obtain 2DES spectra. This choice makes it possible to gain phase stability; indeed, the phase of the measured signal is a function only of the phase difference between beams 1 and 2 since $\phi_3 - \phi_{LO}$ is kept constant during the scan.

3.2.7. Signal acquisition

In a 2DES experiment, a direct measurement of the third-order signal (homodyne detection) is not a convenient approach. Indeed, the signal intensity is typically very low since it is proportional to the squared modulus of its electric field ($I_S \propto |E_S(t)|^2$).
A more useful detection scheme is the heterodyne detection, which consists in the acquisition of the interference between the emitted signal and the LO, which propagates in the same direction as the signal. This approach provides a linear relationship between the signal field and the light intensity. In this scheme, the total intensity is written as [57]:

$$I_{TOT} \propto |E_S(t) + E_{LO}(t)|^2 \propto I_s(t) + I_{LO}(t) + 2\Re\left\{E^*_{LO}(t) \cdot E_S(t)\right\} \tag{3.44}$$

After neglecting the intensity of the signal, much smaller than the mixed contribu-

tion, and subtracting the intensity of LO, obtained from a separate measurement, the signal intensity can be expressed as:

$$I_{HET} \propto \Re \{E^*_{LO}(t) \cdot E_S(t)\} \tag{3.45}$$

One of the advantages of this detection method is that the signal-to-noise ratio is increased because of the linear dependence.
A problem of heterodyne detection is the presence in the signal of several spurious contributions detected by the sCMOS. In addition to the homodyne signal ($|E_S|^2$) and to the LO signal ($|E_{LO}|^2$), also scattering from the exciting pulses in the signal/LO direction has to be removed. For these reasons, a double lock-in detection scheme modulation is employed [65]. In this scheme, two of the incoming pulses, $\vec{k}_2$ and $\vec{k}_3$, are modulated with two optical choppers, whose frequencies are chosen considering the laser repetition rate and the operating frequency of the recording camera: in our setup, the frequencies were set to 250 Hz and 50 Hz, respectively. It is important to consider that the higher modulation frequency should be a multiple of the smaller one, in order to achieve the right phase-locking of the signal and to avoid phase instability. With this acquisition, the signal appears at the sum (300 Hz) or at the difference (200 Hz) of the modulation frequencies. The intensity of the recorded signal can now be expressed as:

$$I_{TOT} \propto I_S(t) + 2\Re \{E^*_{LO} \cdot E_S\} + 2\Re \{E^*_1 \cdot E_S\} + 2\Re \{E^*_2 \cdot E_3\} \tag{3.46}$$

Most of the scattering contributions are removed, since they reach the camera with the frequency of modulation of a single chopper or they are not modulated at all. However, the acquired signal still contains some unwanted contributions, as reported in Table (3.1). Those contributions will be removed from the signal during the data processing steps, as described in the next section.

3.3. Data Processing and Analysis

The 2DES collected data are stored in the form of a 3D-matrix, containing all the signal-LO interference registered as a function of t_1, t_2 and ω_3. However, before data analysis, a preliminary processing step is required to remove the scattering contributions still present. Both the preliminary processing and the data analysis

Table 3.1: All the possible signal contributions acquired by the detector. Only the real part of these contributions can be recorded. The double lock-in method allows removing most of the spurious contributions and only the contributions highlighted in red are retained and must be removed in the data processing procedure.

x	E_1^*	E_2^*	E_3^*	E_{LO}^*	E_S^*
E_1	$\lvert E_1\rvert^2$	$E_1E_2^*$	$E_1E_3^*$	$E_1E_{LO}^*$	$E_1E_S^*$
E_2	$E_2E_1^*$	$\lvert E_2\rvert^2$	$E_2E_3^*$	$E_2E_{LO}^*$	$E_2E_S^*$
E_3	$E_3E_1^*$	$E_3E_2^*$	$\lvert E_3\rvert^2$	$E_3E_{LO}^*$	$E_3E_S^*$
E_{LO}	$E_{LO}E_1^*$	$E_{LO}E_2^*$	$E_{LO}E_3^*$	$\lvert E_{LO}\rvert^2$	$E_{LO}E_S^*$
E_S	$E_SE_1^*$	$E_SE_2^*$	$E_SE_3^*$	$E_SE_{LO}^*$	$\lvert E_S\rvert^2$

are done with a home-written MATLAB® routine.

3.3.1. Preliminary processing

The preliminary processing consists of a series of steps described in detail in previous literature [59]. The most important steps are quickly detailed in the following paragraphs. The recorded interference can be expressed as:

$$E_sE_{LO}^* = \mathcal{E}_s(\omega_3)\mathcal{E}_{LO}(\omega_3)\, e^{i\omega_3(\tau_s-\tau_{LO})} \tag{3.47}$$

with $\mathcal{E}_s(\omega_3)$ and $\mathcal{E}_{LO}(\omega_3)$ the square root of the corresponding fields intensity and $(\tau_s - \tau_{LO})$ the time delay between signal and LO.
Firstly, the raw data are divided by the root square of the LO spectrum to retain only the signal field and the emission axis is interpolated in order to obtain an energy axis evenly spaced. To isolate the pure signal from the $E_s \cdot E_{LO}^*$ contribution, it is necessary to work with complex data; in doing so, the causality property can be exploited: since the LO arrives at the camera after the signal, $(\tau_s - \tau_{LO})$ must be negative and this is imposed by means of a Hilbert transformation. After this operation, the signal becomes a complex valued signal; then a correction for the delay between LO and the zero of the experiment is applied. To reduce the sampling frequency of the signal in the t_1 axis, a rotating frame approach is applied [66].
At this point, the 2DES data must be phased; indeed, the signal contains both a real and an imaginary part, so it is possible to maintain only one part by simply deciding the correct phase to apply. Generally, we are interested in the real part of the signal, because it carries information on the absorptive phenomena happening during the relaxation dynamics of the system under investigation.
A further correction in the phase is necessary because the LO and the exciting pulses

pass through different mediums. In order to remove the spurious contributions still present, a time-filtering in the t_3 dimension is applied by means of a super-Gaussian function; only the third-order signal can be retained by tuning the filter appropriately, taking care not to create artefacts. The fact that the pulses pass through the wedges produces a small dispersion of the pulse spectral components, which affects t_1 and t_2 delays; for this reason, the delay trend is corrected using Equation 3.41.
Finally, the last step is the Fourier transform along t_1, in order to obtain the 2D excitation-emission maps at each scanned value of t_2.
All these operations are performed both for rephasing and non-rephasing datasets; if more than one data has been collected, this preliminary processing is applied to each dataset and then the final data is averaged among all the datasets.

3.3.2. Data Analysis

Once the preliminary processing described above is applied, the data are stored in a 3D-matrix as a function of ω_1, t_2 and ω_3. The study of the evolution of the signal along t_2 provides information about several processes, i.e. the relaxation dynamics of the systems, the presence and the evolution of vibrational, electronic or vibronic coherences or the possibility of energy transfer processes. Moreover, the position of the peaks in a 2D map is informative of the energies of the main states involved in the dynamics of the system and the shape of the peaks provides a way to characterize homogeneous and inhomogeneous broadening. All the processes described above can be divided into two groups, depending on the evolution of the signal along t_2. The first group comprises non-oscillating pathways, where the system reaches a pure state after the first two interactions and evolves following its relaxation dynamics. The second group includes oscillating pathways, in which the system reaches a coherent superposition of states after the first two interactions; thus, the signal oscillates during t_2 with a frequency proportional to the energy gap of the states involved in the coherence, until it dampens over time with its dephasing rate.

3.3.2.1. Global analysis of coherence and population dynamics

For data analysis, we applied the global fitting procedure proposed by Volpato et al. [67], based on finding the best solutions of a minimization problem through the variable projection algorithm. It allows retrieving simultaneously both the non-oscillating and oscillating components of the signal by fitting the data with a sum

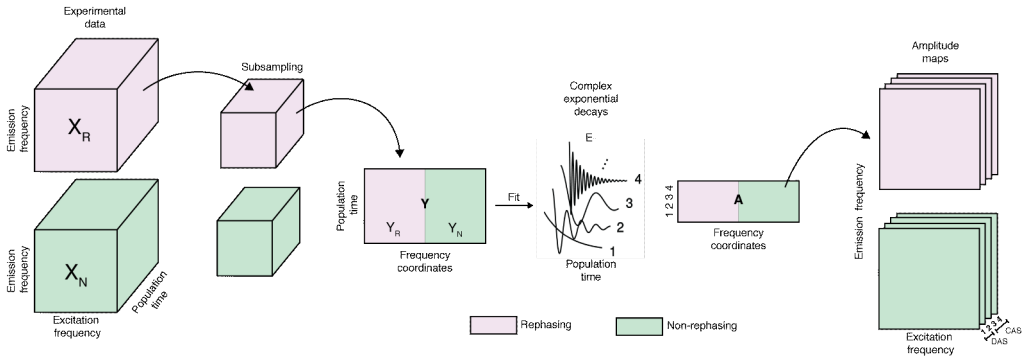

Figure 3.9: Schematic representation of the fitting procedure. Rephasing and non-rephasing data (X_R and X_N) are subsampled and reshaped into the matrix Y, to which the global fitting procedure is applied. From the fitting frequencies, decay constants and matrix A are recovered. Rephasing and non-rephasing amplitude maps are obtained from matrix A for each complex exponential decay component. Two types of maps can be identified: decay-associated spectra (DAS) for non-oscillating signals and coherence-associated spectra (CAS) for oscillating signals. Reproduced from ref. [67].

of complex exponential functions. At the end of the fitting procedure, frequencies, damping times and amplitude maps for all the fitted components of both rephasing and non-rephasing signals can be retrieved in one step. A schematic summary of the fitting procedure is reported in Figure 3.9. From the global fitting procedure, we obtain two different kinds of amplitude maps, useful to interpret the dynamics of the signal evolving in time. Decay-associated spectra (DAS) are obtained by fitting the signal with non-oscillating exponential functions and are used to model the decay of the populations along t_2. A 2D-DAS describes the amplitude distribution of the signals that do not oscillate in time. We only retrieved the real part of a 2D-DAS, since population dynamics are usually associated with absorptive phenomena. In a 2D-DAS, a positive (negative) contribution means that the signal is exponentially decaying (rising) with the associated time constant derived from the fitting procedure.

Coherent-associated spectra (CAS) are used to model the oscillating dynamics of vibrational and electronic coherences between two states of the system. They are obtained by fitting the signal with complex exponential functions to retrieve information on the phase, frequency and amplitude of the beatings.

3.3.2.2. Power spectrum of frequencies

The oscillating dynamics of a system can be also investigated with an alternative approach: the non-oscillating part of the signal can be removed by subtracting it from the total signal and the remaining matrix of oscillating residues can be analyzed separately. The simplest methodology to extract the frequencies of the oscillations

in t_2 consists of integrating the 2D maps of residues along both the excitation and the emission axes and Fourier-transforming along the t_2 axis. In this way, a power spectrum of frequencies, representing the intensities of the beatings that oscillate along t_2, can be obtained. In principle, the power spectrum results analogous to a Raman spectrum if only vibrational coherences contribute to the beatings. Thus, it represents a useful method to distinguish when a particular beating mode is due to a vibrational coherence or to other phenomena, like electronic coherences or solvent contributions. Indeed also vibrational contributions of the solvent can be retrieved and identified by comparison with the Raman spectrum of the solvent.

3.3.2.3. Time-frequency transform

Another approach to investigate the oscillation dynamics of a system is based on time-frequency transform (TFT) [68]. The advantage of TFTs is that they retain information on both time and frequency dimensions, unravelling the dynamics of oscillating signals. Thus, it is possible to follow the evolution of these oscillations along t_2 and determine their dephasing times. Briefly, the oscillating residues, obtained by subtracting the non-oscillating part of the signal, are extracted for a specific point (ω_1, ω_3) of the 2D map and then analyzed by a bilinear transform, in our case an optimized smoothed pseudo-Wigner Ville (SPWV) transform [69]. In this way, for each beating component it is possible to identify the frequency, along the y-axis, and its associated damping time, along the x-axis.

4 | Chlorophyll b

4.1. Introduction

The work presented in this Chapter aims at investigating the spectroscopic properties of isolated chlorophyll *b* (Chl *b*) molecules in solution. Chl *b* is one of the most important photosynthetic pigments, found in land plants, cyanobacteria and green algae. The majority of Chl *b* is usually found inside of light-harvesting complexes (LHCs), large pigment-protein complexes responsible for the early steps of photosynthesis. Its biological functions in these photosynthetic complexes have been widely studied in the literature. For example, it is known that Chl *b* expands the spectral range of wavelengths absorbable by a photosynthetic system, so it is used for capturing sunlight and tunnelling it to the reaction centres together with chlorophyll *a* (Chl *a*) [70, 71]. Chl *b* also plays an essential role in enhancing the turnover of LHCs, which is probably related to its capability of binding more tightly to the LHC with respect to other chlorophylls species [72].
Usually, LHCs involve multiple interactions of the pigments between each other and with the protein backbone [73, 74]. Nevertheless, the complexity of these interactions often hinders an in-depth comprehension of all the fine details regulating the biological functions. For these reasons, preliminary investigations on the photophysical properties of isolated Chl *b* may be of help to disentangle its role in these complex environments. In previously reported studies, Chl *b* dynamics have been investigated through different time-resolved techniques [75, 76], and also multidimensional spectroscopy [77, 78], to disclose more details on its relaxation dynamics. However, all these works focused on processes happening on a longer timescale, studying, for example, the internal conversion dynamics [76] or the spectral diffusion [77] after the first hundreds of femtoseconds after excitation. Nonetheless, the very early steps of the relaxation dynamics immediately after photoexcitation are crucial to understanding all the ensuing processes, including energy transfer when the Chl *b* molecule is part of a light-harvesting chromophore network. Thus, in this

work, we applied 2DES to investigate the sub-100 fs relaxation dynamics of Chl *b* within the Q-bands. The measures were performed both at room temperature and at 77 K to evaluate the contribution of different dynamic mechanisms present in the two different conditions.

4.1.1. Experimental Methods

Chl *b* from spinach was purchased from SigmaAldrich and used without further purification. For 2DES measurements at room temperature Chl *b* was dissolved in a 4:1 methanol-ethanol mixture and diluted until reaching an optical density of 0.3 on the Q-bands maximum in a 1 mm cuvette. For 2DES measurements at 77 K the sample was prepared by dissolving Chl *b* in a 4:1 methanol-ethanol mixture, until an optical density of about 0.3 was reached in the Q-bands maximum in a 0.5 mm cuvette. The ethanol-methanol mixture was selected for its capability of forming a good glass matrix at 77 K. We ruled out the presence of Chl *b* aggregates at these conditions lowering the concentration down to one order magnitude and observing no spectral changes in the normalized steady-state absorption spectra.
Since Chl *b* is particularly sensitive to photo-oxidation, all the solutions were degassed and immediately sealed. Moreover, steady-state absorption spectra were acquired before and after each scan to control that no degradation of the sample happened during the 2DES measurements.
2DES measurements were performed tuning the laser spectrum to cover the Q-bands spectral region. Therefore, the outcoming pulses were centred at 15380 cm^{-1} (650 nm). The pulse duration, optimized through FROG measurements, was compressed to 10 fs, leading to a spectral bandwidth of about 1471 cm^{-1}. The pulse energy was 7 nJ at the sample position. The optical setup for 2DES measurements was described in detail in Chapter 3. An Oxford Instruments OptistatDN cryostat was employed for the measurements at 77 K. The population time t_2 was scanned from 0 to 1000 fs, in steps of 7.5 fs, while the coherence time t_1 was scanned from 0 to 125 fs in steps of 3 fs. Each experiment was repeated at least five times to ensure reproducibility.

4.1.2. Linear Characterization

The linear absorption spectra measured for Chl *b* in a 4:1 ethanol-methanol mixture, both at room temperature (RT) and at 77 K, are reported in Figure 4.1(b).

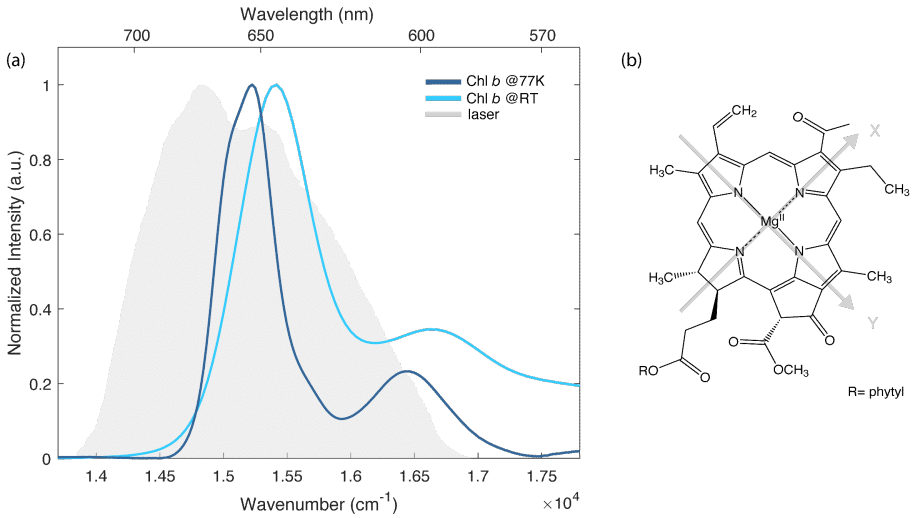

Figure 4.1: (a) Normalized absorption spectra of Chl *b* in the Q bands region at room temperature (light blue) and at 77 K (dark blue). The grey area represents the laser spectrum profile used in the 2DES experiments. (b) Molecular structure of Chl *b*. Adapted from Ref. [84].

The electronic properties of Chl *b* are conventionally explained according to Gouterman's four orbital model [79, 80]. Within this framework, the lowest energy transitions, labeled as Q-bands, are the result of two possibly overlapping independent electronic transitions identified as Q_x ($S_0 \rightarrow S_2$) and Q_y ($S_0 \rightarrow S_1$) [81]. The subscripts x and y identify the polarization directions within the macrocycle plane, as illustrated with gray arrows in Figure 4.1(b). Higher energy vibronic transitions arise instead as separated sidebands, usually identified as Q_y(0,1) and Q_x(0,1), respectively.

At RT, the lowest energy band at 15420 cm^{-1} (648 nm) is assigned to Q_y(0,0) transition, while higher energy signals are attributed to the mixing of Q_y(0,n) and Q_x states [76, 82]. At RT, these bands are broadened by the activation of low-frequency molecular vibrations and by inhomogeneous effects. Conversely, as expected, the spectrum at 77 K is slightly blue-shifted with respect to the one at RT and is characterized by narrower bandwidths [83].

4.1.3. Results

A comparative study of the ultrafast dynamics of both Chl *b* at RT and at 77 K was performed by means of 2DES. The investigated spectral region covers the lowest energy part of the Q-band, as shown in Figure 4.1(a).

The 2DES response can be visualized in a series of 2D frequency-frequency maps correlating the excitation (x-axis) and the emission (y-axis) frequencies for each value

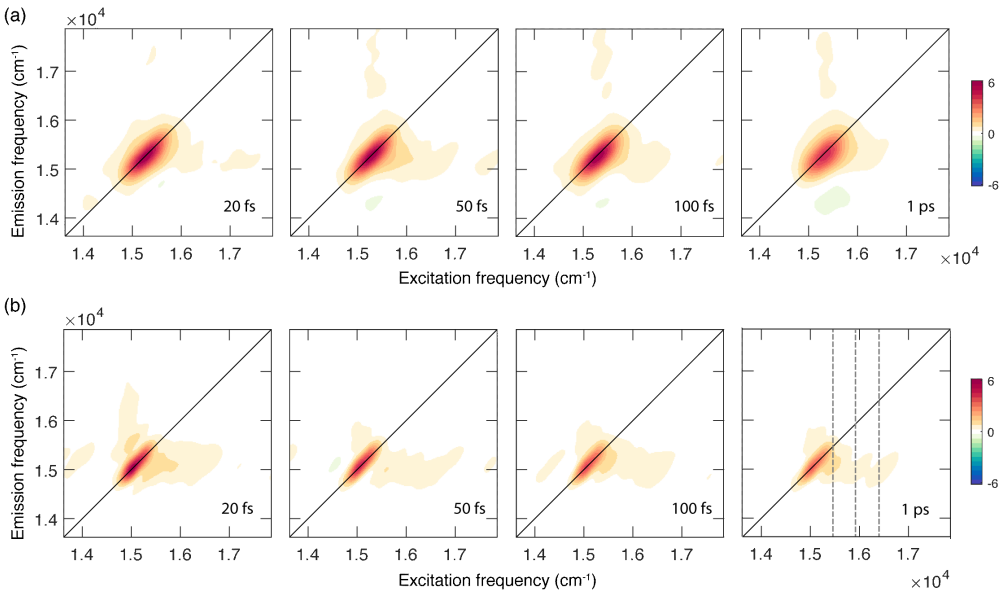

Figure 4.2: Absorptive 2DES maps of Chl *b* in a EtOH-MeOH 4:1 mixture recorded at (a) RT and at (b) 77 K at selected values of population time. Grey dashed lines in the map at population time of 1 ps at 77 K pinpoint the positions of the main vibronic features at an excitation energy of 15400, 15990 and 16400 cm^{-1}. Adapted from Ref. [84].

of the population time [46, 47].

Figure 4.2 shows the evolution of the 2DES signal as a function of the population time at RT (panel a) and at 77 K (panel b). For both sets of measurements, the main feature in the 2D maps is a diagonal peak attributed to the ground state bleaching and stimulated emission of the $Q_y(0,0)$ band excited by the laser. In addition, the presence of cross peaks can be assessed at symmetric off-diagonal positions. The most intense cross peak is centered at coordinates of about (16000, 15250) cm^{-1}, which position is consistent with the coupling of $Q_y(0,0)$ state with vibrational modes in the range 200-1100 cm^{-1}. These modes are also responsible for the broadening and the vibronic progression in the linear absorption spectrum. Ultrafast relaxation processes from higher states can also contribute at these spectral coordinates, as verified for Chl *a*. All these spectral features are expected for isolated Chl *b* molecules in solution and in agreement with what was previously reported for other chlorophylls and tetrapyrrole compounds [85–88].

A first qualitative comparison of the response at RT and at 77 K reveals significant differences in the spectral shape of the signals and their related time evolution. At RT, the 2D maps are characterized by a broader signal that is initially elongated along the diagonal and becomes more rounded at longer population times. On the contrary, the signal on the maps recorded at 77 K appears significantly narrower, es-

pecially along the anti-diagonal dimension, and does not show a relevant evolution of the peak shape in the investigated time window of 1 ps. The narrower bandwidth allows us to identify more clearly the vibrational modes which contribute most to the lower diagonal cross-peaks, where signals at an excitation energy of about 15400, 15990 and 16400 cm^{-1} can be identified. The coordinates of these signals are consistent with the energy of the vibronic features emerging also from the absorption spectrum at 77 K and with the frequency of the most intense vibrational modes of the Chl *b* molecule, as also outlined by Raman spectroscopy (see Figure 4.6(a)).

To clarify the dynamics underlying the time evolution of the 2DES response, the data have been analysed through a multi-exponential global fitting procedure [67], where the first 10 fs were omitted to minimize possible artifacts arising from pulse superposition. This fitting procedure allows retrieving both the oscillating and non-oscillating dynamics of the 2DES response and could efficiently disentangle the different components that contribute to the evolution of the 2DES signal [67].

Focusing first on the non-oscillating population dynamics, the global fitting reveals a bi-exponential decaying behaviour for both RT and 77 K measurements. The fitting results (Figure 4.3) are shown in terms of 2D-DAS (2D-Decay Associated Spectra), each one associated with a specific time constant resulting from the bi-exponential fitting of both sets of measurements. For the solution of Chl *b* at RT, the fitting analysis revealed two time constants of about 150 fs and >1 ps, respectively. The longer time constant captures the dynamics of all processes that happen in a timescale longer than the investigated time window [86, 89, 90]. Also the development of an excited state absorption (ESA) is included in these dynamics and manifested as a negative feature at coordinates (15410, 14350) cm^{-1}, whose intensity progressively decays as the population time increases. The same phenomenon has already been observed for solutions of Chl *b* in different solvents in the same timescale [77]. The 2D-DAS associated with the ultrafast component exhibits a signal that is decaying on the diagonal (red area) and rising on the two regions above and below diagonal (blue areas). As already reported in the literature, when considering the dynamics of the monomeric Chl *b* in different solvents, time constants of hundreds of femtoseconds are typically ascribed to the spectral diffusion process [85, 87, 89, 90]. Indeed, fluctuations in the environment surrounding an isolated chromophore cause changes in its electronic transition frequency [85], causing a loss of correlation between the absorption and emission frequencies as the population time evolves. This is also reflected in the progressive 'rounding' of the main diago-

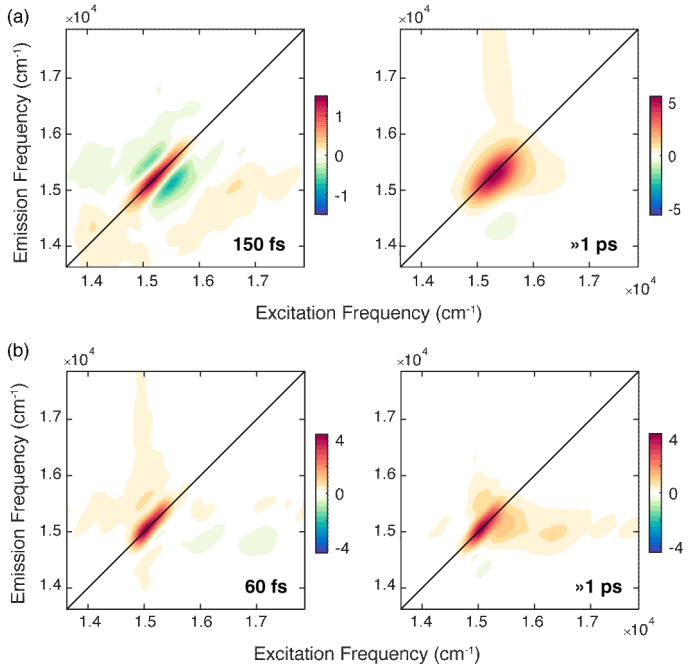

Figure 4.3: 2D-decay associated spectra (2D-DAS) resulting from the global fitting of the 2DES maps recorded for Chl *b* at (a) RT and (b) 77 K. The associated time constants are reported in each panel. A positive (negative) amplitude is recorded where the signal is decaying (rising) and indicated with a red (blue) colour. Adapted from Ref. [84].

nal peak, as already pointed out in the 2D-maps at RT. The estimated time constant of 150 fs is in good agreement with the typical timescales found for the solvation dynamics of dyes in MeOH and EtOH and can be assigned to the inertial component of solvation that results from the libration motion of the solvent molecules [85, 89, 91–93].

Differently from what was found for Chl *a* in similar conditions, no evident signatures of ultrafast $Q_x \rightarrow Q_y$ relaxation could be captured in Chl *b*. A possible explanation could be found in a different degree of mixing of the Q_x and Q_y bands, stronger in Chl *a* than in Chl *b* [82]. This would also justify the modified rate of Q_x-Q_y internal conversion in the two molecules [76].

A deeper understanding of the relaxation dynamics of Chl *b* in the ultrafast regime can be achieved by analysing the 2DES data collected at 77 K. Also for Chl *b* at 77 K, the global fitting analysis revealed two time constants of 60 fs and > 1 ps. The longer time constant describes dynamics similar to that recorded at RT, while the fastest component has a shorter time constant. At 77K, it is unlikely that the 60 fs dynamics originate from a spectral diffusion process. Indeed, it is expected that the spectral diffusion process is slowed down because the solvent fluctuations are dumped by the glass matrix [93]. Moreover, the associated 2D-DAS shows a signal

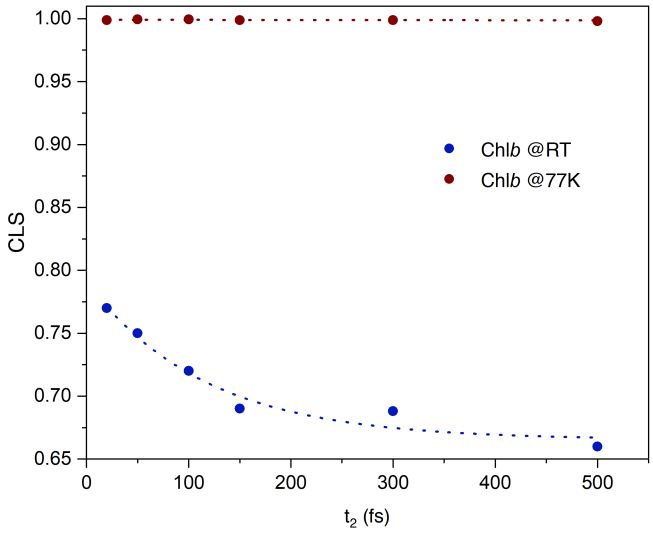

Figure 4.4: Centre line slope method results for Chl *b* at RT (blue) and 77K (red). The error in the determination of the centre line slope is estimated in the order of the 10%. Adapted from Ref. [84].

distribution different from the typical spectral shape expected for spectral diffusion. In addition, the rounding of the peak in the 2DES maps recorded at 77 K is less evident if compared to the ones measured at RT.

To verify this assumption, we applied the center line slope method (CLS), a methodology often used to study spectral diffusion in 2D spectra [77, 94]. Following the procedure reported in ref.[77], the center line of the 2D signal at a selected value of population time t_2 has been determined by using Gaussian functions fitted to slices parallel to the emission frequency y-axis. The obtained center line was then fitted by linear regression from which the angular coefficient was retrieved. We repeated this procedure for a number of 2D maps at selected values of t_2 from 20 to 500 fs and we plotted the slope values as a function of t_2 (circles) in Figure 4.4. The CLS at RT clearly shows a mono-exponential decay behavior with a time constant of 115 ± 36 fs (blue dashed line). No decay of the CLS is instead recorded at 77K, implying that there is no correlation loss due to solvent dynamics in this timescale at this temperature and confirming our assumption.

The 2D-DAS, together with a decaying signal on the diagonal, distinctly shows the presence of a rising amplitude at the lower diagonal cross peak coordinates, where the vibrational modes more strongly coupled with the Q_y transition contribute, as already shown in Figure 4.2(b). The presence of negative features below the diagonal in the ultrafast timescale is typically associated with relaxation phenomena moving

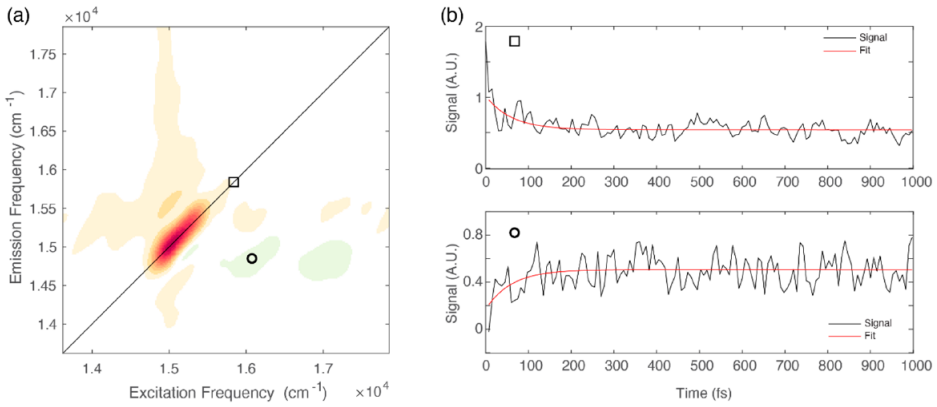

Figure 4.5: (a) 2D-DAS relative to the 60 fs component obtained for Chl *b* at 77 K. The circle and the square markers pinpoint relevant diagonal and off-diagonal coordinates: (15580, 15580) and (14900, 16050) cm^{-1}, respectively. (b) Signal decay extracted at relevant coordinates identified by the square (upper panel) and circle (lower panel). Adapted from Ref. [84].

population from higher to lower energy states [88, 89, 95]. This relaxation can also be identified by direct inspection of the signal decay at relevant coordinates. For example, in Figure 4.5, we reported the decay of the signal at diagonal coordinates (square) and the corresponding rise, with the same time constant, of the signal at off-diagonal coordinates (circle).

It has been reported that the exciting energy is quickly dumped into molecular vibrations through fast internal conversion when the modes of the bath are hindered by the low temperature [96]. These findings suggest that, at 77 K, when the spectral diffusion due to the inertial component of solvation is inhibited, the first mechanism of relaxation involves the redistribution of energy to vibrational modes. The distribution of the negative amplitude signal in the 2D-DAS associated with the 60 fs time constant is characterized by an emission frequency (y-coordinate) of about 15000 cm^{-1}, corresponding to the lowest energy Q_y (0,0) band and representing the final relaxed state. On the excitation axis (x-coordinate) we recognize two maxima at about 16000 and 17000 cm^{-1}, which suggests that vibrational relaxation mainly involves vibrational modes in the frequency range of 1000–2000 cm^{-1}. This finding is particularly relevant if compared with the results of simulations performed on Chl *a* and suggests that only a subset of vibrational modes, also in this case with frequencies in the range of 1400–2000 cm^{-1}, seems to actively support the internal conversion process [97]. Non-radiative relaxation of excited electronic states is invariably accompanied by vibrational energy redistribution and the vibrational degrees of freedom are reported to assist the internal conversion processes in different

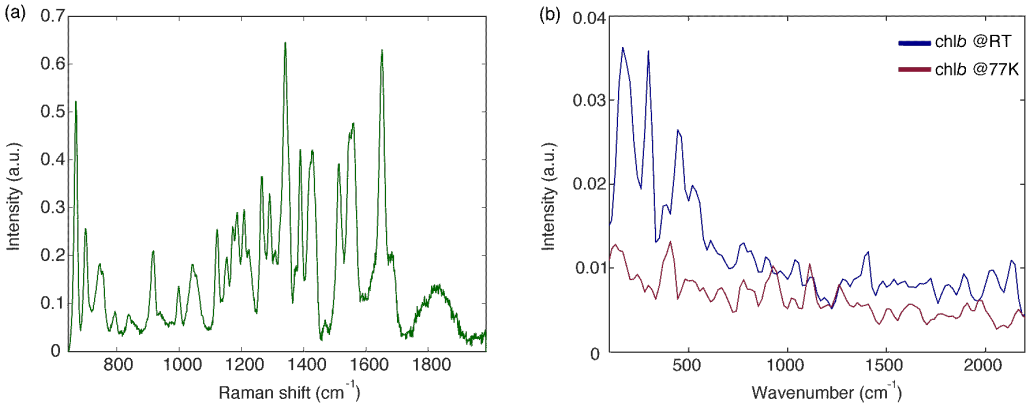

Figure 4.6: (a) Raman spectrum of Chl *b* (b)Power spectra of frequencies obtained from the analysis of the purely absorptive 2DES maps of Chl *b* at RT (blue) and at 77 K (red). Before calculating the residues, the 2DES response has been normalized on its maximum in order to allow a comparison between the amplitudes of the beatings in the two sets of measurement. Adapted from Ref. [84].

tetrapyrrole compound [97–100]. Here, we exploited the multidimensionality of the 2DES technique to identify the main vibrational modes involved in this relaxation. The analysis of the beating behaviour supports this interpretation. The oscillating residues, obtained after the subtraction of the decaying part of the signal, have been Fourier transformed to get the power spectrum of frequencies, which correlates the intensity of each beating component to its frequency [68]. Figure 4.6(b) reports the power spectra of Chl *b* at RT and at 77 K. The beatings in the 2DES signal of isolated dyes in solution originate from vibrational coherences in the ground and excited state, and can be directly compared to the vibrational modes in Raman spectra (Figure 4.6(a)).

The overall amplitude of the beating in the Chl *b* response, both at RT and 77 K, is not particularly intense. This can be justified considering the low value of the Huang-Rhys factors of the vibrational modes for chlorophyll molecules [82, 83]. Nonetheless, a few vibrational modes typical of tetrapyrrole compounds and already widely documented in the literature can be identified at about 200, 296, 380, 450, 530, 770, 926, 1120 and 1260 cm^{-1} [86, 87, 89, 90]. Moreover, with respect to RT, the amplitude of the vibrational modes with a frequency lower than 700 cm^{-1} appears strongly quenched in the power spectrum at 77 K (200, 296, 380, 450 and 530 cm^{-1}), whereas the amplitude of higher frequency modes is more or less conserved (770, 926, 1120 and 1260 cm^{-1}). This trend is expected considering that the low frequency modes are usually characterized by a certain degree of anharmonicity, which introduces a temperature dependence of the dephasing [101] and of the coupling [102]. Nonetheless, this also confirms the critical role of high frequency

modes in the early time ultrafast relaxation dynamics of Chl *b*.

4.2. Final remarks

The ultrafast dynamics of Chl *b* have been characterized by means of the 2DES technique both at RT and at 77 K. The measurements at RT allowed the characterisation of the spectral diffusion processes associated with the inertial component of solvation, with a time constant of 150 fs. The comparison with the experimental results obtained on Chl *a* solutions in similar experimental conditions [89] highlighted a marked difference in the internal conversion mechanism among the two molecules. Unlike Chl *a*, in Chl *b* there is no trace of internal conversion between Q_x and Q_y bands in the timescale of hundreds of fs. This confirms previous assumptions based on indirect experimental findings [78, 97] and supports theoretical predictions suggesting a lower degree of Q_x-Q_y mixing in Chl *b* [82].
At 77 K, where the inertial motion of solvent molecules is frozen, the primary mechanism dominating the first stages of the relaxation of the excited state is an ultrafast (60 fs) redistribution of energy into vibrational modes. While it is known that the non-radiative relaxation of excited electronic states is invariably accompanied by vibrational energy redistribution, we could also verify the importance of a selected subset of vibrational modes assisting the internal conversion process. The characterization of these dynamic and mechanistic details is an important piece of information for a better understanding of the role of Chl *b* in light-harvesting complexes. To verify whether or not the presence of Chl *b* within a protein environment could affect its relaxation dynamics, in the following Chapter we built on the knowledge acquired in this work to study a model pigment-protein complex. In particular, we wanted to correlate possible changes in its optical response to the complex interplay between the chromophores and the protein environment.

5 | Water-Soluble Chlorophyll-binding Protein

5.1. Introduction

When chromophores are embedded in a protein scaffold, the heterogeneity of the protein environment can deeply affect their spectral properties and their dynamics [20]. In a general framework, the scaffold controls the arrangement of chromophores, leading to an optimized structure and improving the efficiency of excited-energy transfer between the bound pigments [15, 18]. Specific interactions between chromophores and individual amino acids are reported to tune the spectroscopic properties of the pigments: they may affect the interchromophore interactions by determining their 3D arrangement or by modifying their site energy [15, 18, 20, 27, 31]. Interestingly, it has been demonstrated that the tuning of the chromophores properties can be achieved by the formation of hydrogen (H) bonds between the protein and the pigment [18, 31, 103]. Notwithstanding, several details of the complex interplay between the active molecules and the protein environment at the molecular level are not yet fully clarified. Moreover, the investigation can be rather complicated by the great number of different pigments bound in each protein subunit.

In this context, the Water-Soluble Chlorophyll-binding Protein (WSCP) represents an ideal model system to investigate more deeply this kind of interactions. WSCPs are a group of water-soluble proteins found in many higher plants containing only Chl molecules and no carotenoids [104]. Two classes of WSCPs are distinguished according to their photophysical properties: class I WSCPs are subject to photoconversion [105], whereas class II WSCPs are not sensitive to illumination [105, 106]. Type II WSCPs can be further divided into class IIa and IIb [107], depending on their Chl a/b ratio in native complexes and on the absorption spectra of the bound Chls [108].

The structure of class II WSCPs shows a tetrameric architecture formed by four identical subunits of about 20 kDa, each binding only one Chl molecule (Figure 5.1(b)) [109, 110]. The mechanism of tetramer formation is still under investigation but it seems to be promoted by Chl binding. Indeed, it has been hypothesized that the pre-formation of a Chls dimer could be the initial step in the oligomerization process and could lead to the stabilization of the tetrameric complex [111]. The four Chls are packed in a hydrophobic cavity within the protein matrix, forming two "open-sandwich" dimers [112], as shown in Figure 5.1(b) and (c).
The biological role of WSCP is still unclear. WSCPs do not seem to be directly involved in photosynthesis, as class-II WSCPs are not located in the chloroplasts [113]. The fact that WSCPs of different species are found in different plant organs suggests that each WSCP can perform different biological functions. Among all, WSCP has been proposed to function as a scavenger of Chls that are released during cellular breakdown or disruption [110, 113] under stress conditions [114], due to its ability to extract and bind Chls from thylakoid membranes [115].
In this work the attention is focused on the ultrafast relaxation dynamics of four pigment–protein complexes, obtained by reconstituting two WSCPs, either from *Brassica oleracea* (belonging to class IIa, in the following denoted as Bo) or *Lepidium virginicum* (belonging to class IIb, denoted as Lv) with only Chl *a* or Chl *b*. The four resulting complexes are labeled Bo-*a*, Bo-*b*, Lv-*a*, and Lv-*b*, respectively.

5.1.1. Crystallographic structure

The crystal structure of the native WSCP extracted from *Lepidium Verginicum* (LvWSCP) was determined by X-ray crystallography at 2.0 Å resolution [110]. The protein shows a homotetrameric structure, with the four chains composing the tetramer related by a nearly strict 222 symmetry except for the outer loops, which deviate from this symmetry. The WSCP tetramer can be described as a dimer of dimers, where pairs of chains 1-2 and 3-4 (numbered as shown in Figure 5.1(b)) are the principal dimers. Each of the four protein subunits binds only one Chl molecule. The four Chls are tightly packed in a hydrophobic cavity at the center of the tetramer. Each Chl binds to its monomer through a coordination bond between the carbonyl oxygen of a proline residue (P_{36}) and the central Mg^{2+} ion of the Chl. The pigments are β-ligated, namely from the top of the macrocycle. This is an uncommon feature in Chl-binding proteins where chlorophylls are predominantly α-ligated (from the bottom of the macrocycle) [116, 117]. The four Chls are related by a pseudo 222 sym-

metry and are organized into two dimers, Chl-1/Chl-2 and Chl-3/Chl-4. The Chl dimer has an "open-sandwich" structure with an interplanar angle of 27°. The four phytyl chains of the Chl molecules protrude from the tetrapyrrole dimer at one end facing each other, therefore creating a hydrophobic cavity at the tetramer center. This hydrophobic interaction is considered to be the driving force of tetramerization.

The structure of recombinant WSCP from *Brassicaceae* (BoWSCP) was resolved at 1.9 Å resolution [109]. The crystallographic structure of Bo-*a* is shown in Figure 5.1(b). The LvWSCP and BoWSCP protein sequences are highly homologous. Indeed, the protein structures and Chls arrangements in monomeric and dimeric subunits are very similar to that of LvWSCP described above. However, BoWSCP differs for the relative dimers orientation, showing a 60° rotation of one of the two dimeric units against the other within the tetramer. The main difference is a deformation of the planar Chl macrocycle in BoWSCP with respect to LvWSCP. In particular, an asparagine at position 38 (N_{38}) in LvWSCP is replaced by an alanine at position 34 (A_{34}) in BoWSCP. For this reason, a conserved tryptophan residue (LvWSCP W_{154}, BoWSCP W_{151}) forms an alternative hydrogen bond with the backbone oxygen of A_{34}. The tryptophan sidechain moves and this leads to a bending of the ring out of the Chl macrocycle plain.

5.2. Calculation of the electronic coupling

The structural arrangement of the four Chls in the protein scaffold can be modeled as a dimer motif. The electronic coupling V is expressed in terms of dipole-dipole interaction [49]:

$$V_{mn} = \left(\frac{f_i^2}{4\pi\varepsilon_0\varepsilon_r}\right)\left[\frac{(\boldsymbol{\mu}_\alpha^m \cdot \boldsymbol{\mu}_\alpha^n)}{\boldsymbol{r}_{mn}^3} - 3\frac{(\boldsymbol{\mu}_\alpha^m \cdot \boldsymbol{r}_{mn})(\boldsymbol{\mu}_\alpha^n \cdot \boldsymbol{r}_{mn})}{\boldsymbol{r}_{mn}^5}\right] \tag{5.1}$$

where the subscripts m and n run over the four Chls molecules in the WSCPs, $\boldsymbol{\mu}_\alpha^m$ is the transition dipole moment of the isolated Chls in a spherical cavity (4.58 D for Chl *a* and 3.83 D for Chl *b*) [119] and $\boldsymbol{r}_{mn}$ is the relative distance between pairs of Chls taken from the center of one molecule to the center of the other; ε_0 is the dielectric constant in the vacuum and ε_r is the relative dielectric constant assumed to be 2.40, as derived from a refractive index of 1.55 typical for protein environments [110]. f_i^2 is the local-field correction, considering the molecules embedded in a spherical

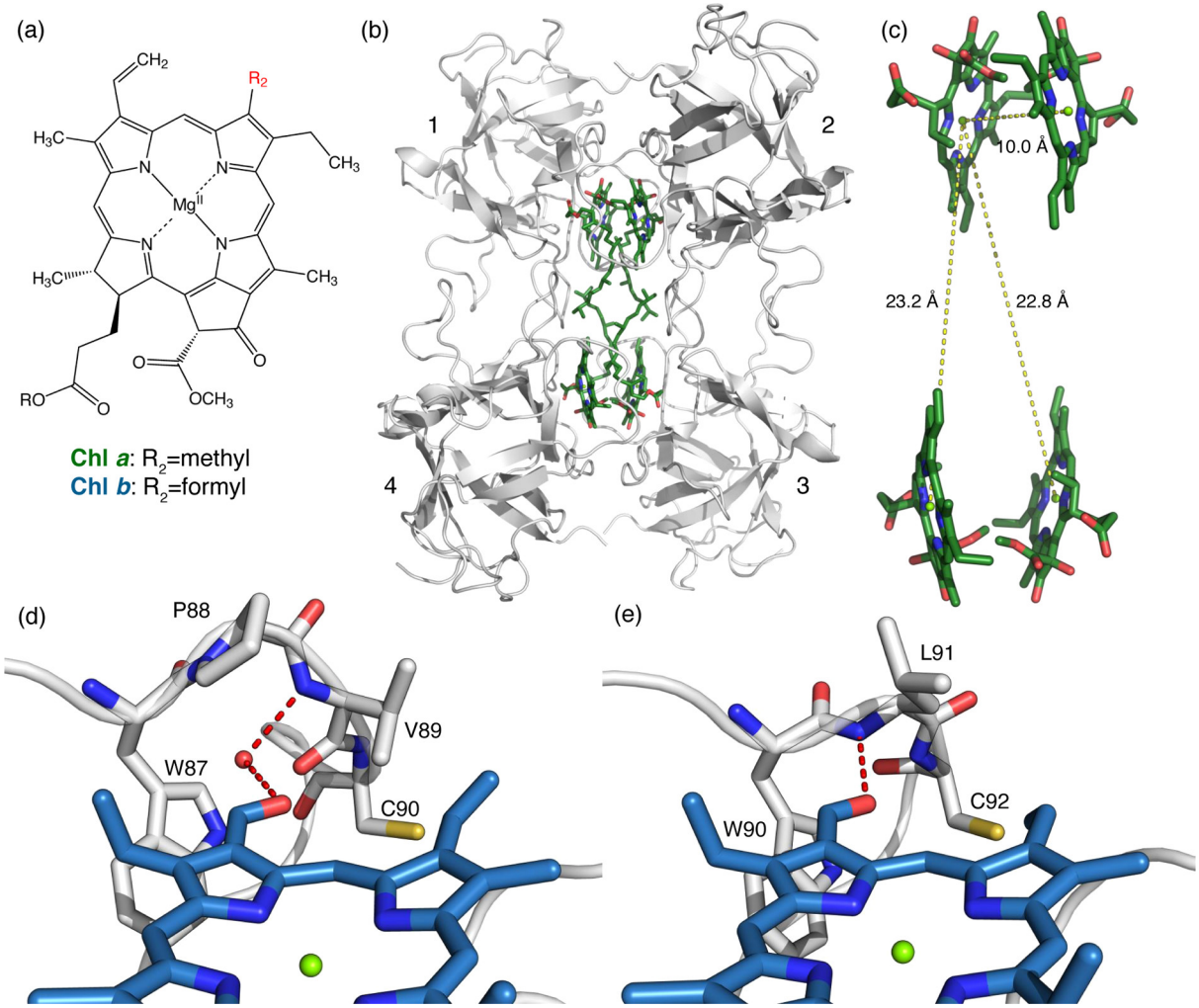

Figure 5.1: (a) Molecular structure of Chl *a* and Chl *b*. They differ in the R_2 group in the C7 position. (b) Crystallographic structure of Bo-*a*, where the tetrameric architecture is recognizable. Chls *a* are shown as green sticks, and the protein scaffold is shown in gray. The structures of Bo-*b*, Lv-*a*, and Lv-*b* present similar tetrameric structures. (c) Arrangement of the Chl molecules inside the tetramer, organized in two "open-sandwich" dimers. Center–center distances are shown with yellow dashed lines. The phytyl chains are omitted for clarity. (d,e) Detail of the surroundings of Chl *b*'s formyl in (d) Bo-*b* and (e) Lv-*b*, pinpointing the H-bonds with red dashed lines. Chls *b* are shown as blue sticks, the protein is in gray. A red dot has been added to the position at which a water molecule is expected to be present in Bo-*b*. Adapted from Ref. [118].

cavity and surrounded by a dielectric medium [49]:

$$f_i^2 = \frac{\varepsilon_r + 2}{3} \tag{5.2}$$

The relative orientations of the transition dipole moments and the values of inter-chromophore distances have been derived from the crystallographic structure. The calculated *V* among pairs of Chls for the four WSCPs are reported in Table 5.1, where the four Chls are numbered as in Figure 5.1(b).

5.3. Experimental Methods

The four WSCP complexes were expressed and reconstituted with purified Chls according to the protocol described by Agostini et al. [111] and were kindly provided by prof. H. Paulsen (Johannes Gutenberg Universitat - Mainz). For 2DES experiments at room temperature (RT), the samples were diluted in sodium phosphate buffer (20 mM, pH 7.8) until reaching an optical density of 0.3 on the Q_y maximum in a 1 mm cuvette. For 2DES measurements at 77 K, the samples were mixed with 60% glycerol (v/v) until an optical density of 0.3 in a 0.5 mm cuvette was reached on the Q_y maximum. The samples were degassed and immediately sealed to avoid the formation of oxidised species during 2DES measurements. Steady-state absorption spectra were recorded before and after each scan to check that no degradation of the sample occurred during 2DES measurements.
For 2DES measurements, the laser spectrum was centered at 15380 cm^{-1} (650 nm) to cover the Q_y spectral region. The pulse duration, optimized through FROG measurements, was compressed to 8 fs, corresponding to a spectral bandwidth of about 1840 cm^{-1}. The population time t_2 was scanned from 0 to 1000 fs in steps of 7.5 fs, while the coherence time t_1 was scanned from 0 to 125 fs in steps of 3 fs. Each experiment was repeated three times to ensure reproducibility. The exciting energy was 7 nJ at the sample position. The measurements have been performed under the same conditions at RT and at 77 K, employing an Oxford Instruments OptistatDN cryostat.

Table 5.1: Calculated values of dipole-dipole interaction in cm^{-1} for each couple of Chls in Lv-*a*, Bo-*a*, Lv-*b* and Bo-*b*.

Lv-*a*	Chl-1	Chl-2	Chl-3	Chl-4
Chl-1	-	102.60	7.26	22.46
Chl-2	102.60	-	22.45	8.48
Chl-3	7.26	22.45	-	101.58
Chl-4	22.46	8.48	101.58	-

Bo-*a*	Chl-1	Chl-2	Chl-3	Chl-4
Chl-1	-	108.31	9.12	10.89
Chl-2	108.31	-	11.23	9.12
Chl-3	9.12	10.89	-	108.31
Chl-4	11.22	9.12	108.31	-

Lv-*b*	Chl-1	Chl-2	Chl-3	Chl-4
Chl-1	-	67.51	5.21	15.02
Chl-2	67.51	-	14.86	5.68
Chl-3	5.21	14.86	-	66.60
Chl-4	15.02	5.68	66.60	-

Bo-*b*	Chl-1	Chl-2	Chl-3	Chl-4
Chl-1	-	66.63	6.37	7.96
Chl-2	66.63	-	7.96	6.37
Chl-3	6.37	7.96	-	66.63
Chl-4	7.96	6.37	66.63	-

5.4. Linear characterization

The four WSCP complexes were first characterized through linear absorption and circular dichroism spectroscopy. Regarding their optical properties, each dimer in WSCP has an "open sandwich" structure with an interplanar angle of about 27° and a center-to-center distance of 9.0 Å [110], as already outlined above. Therefore, the transition dipole moments of the two chlorophylls in the dimer are not fully parallel and show deviations from the optical behavior of a pure H-dimer. Indeed, while in an ideal H-dimer only the transition to the upper excitonic state is permitted, in Chl-WSCP complexes also the transition to the lower-energy excited state is partially allowed.

The absorption spectra of the four complexes at room temperature (RT, panels a and b) and 77 K (panel c) in the region of the Q bands are shown in Figure 5.2. In this spectral region, the protein spectra exhibit the typical features of Chl *a* and *b* chromophores, where Q_y and Q_x bands and their vibronic progressions are easily identified. The red shift of the Q_y maximum recorded for both Bo samples with respect to their Lv analogous can be explained with the deformation of the Chl *a* macrocycle planarity that occurs in Bo structure, while the pigments retain their flat conformation in Lv. Also the emission spectra for the four complexes at RT show the typical spectral properties of Chl *a* and *b*.

At RT, no sign of excitonic features is observed. Indeed, as a result of the excitonic interaction and of the geometry of the chlorophylls in the dimer, two bands should be observed in the absorption spectra. However, the disorder of the system at RT causes a significant inhomogeneous broadening of the bands, which does not allow to resolve the excitonic splitting. On the other hand, the spectra at 77 K are

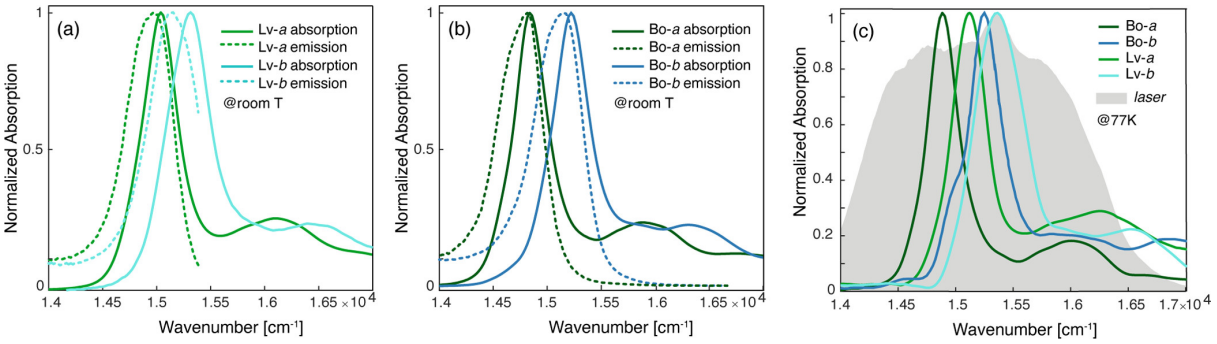

Figure 5.2: (a) Normalized absorption (solid line) and emission (dashed line) spectra of Lv-*a* (green) and Lv-*b* (light blue) in the Q-band region at room temperature. (b) Same as panel a for Bo-*a* (dark green) and Bo-*b* (dark blue). (c) Normalized absorption spectra at 77 K. The gray area represents the laser spectrum profile used in the 2DES experiments. Adapted from Ref. [118].

characterized by narrower and slightly blue-shifted peaks. Two main observations can be made by comparing the spectra of the four species. First, Lv complexes in both cases present a broader line shape; second, Chl *b*-binding proteins have a more resolved structure, with the appearance of clear shoulders on the red side of the spectra, which are less distinguishable in Chl *a* complexes. For example, in Bo-*b* it is possible to distinguish an additional band at about 14750 cm^{-1} (678 nm) and a shoulder of the main Q_y band at about 15000 cm^{-1} (656 nm). These two red shifted features are attributed to excitonic states, as mentioned before.
The presence of excitonic interactions among Chls is also confirmed by the CD spectra in the Vis region, reported in Figure 5.3 for all the four complexes at RT. The presence of two oppositely signed bands in the region from 550 to 750 nm for all WSCP samples is a clear signature of excitonic coupling among pigments. Moreover, the spectra of the Chl *b*-complexes, especially Lv-*b* are non-conservative, in contrast to those of the Chl *a* complexes, indicating the presence of higher-order couplings [120].

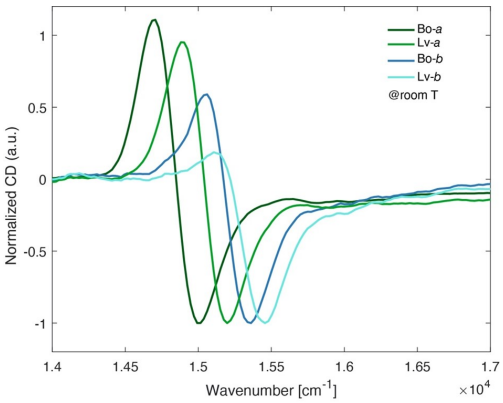

Figure 5.3: Vis-CD spectra of the four complexes at room temperature normalized on the negative peak. Adapted from Ref. [118].

5.5. 2DES characterization

5.5.1. Measurements at room temperature

Figure 5.4 shows the evolution of the 2DES signal as a function of the population time at RT. The main feature in the 2D maps is a diagonal peak due to ground state bleaching and stimulated emission involving the main electronic transitions addressed by the exciting pulses. At RT, the peak appears horizontally elongated because of the presence of a lower diagonal cross peak associated with the pres-

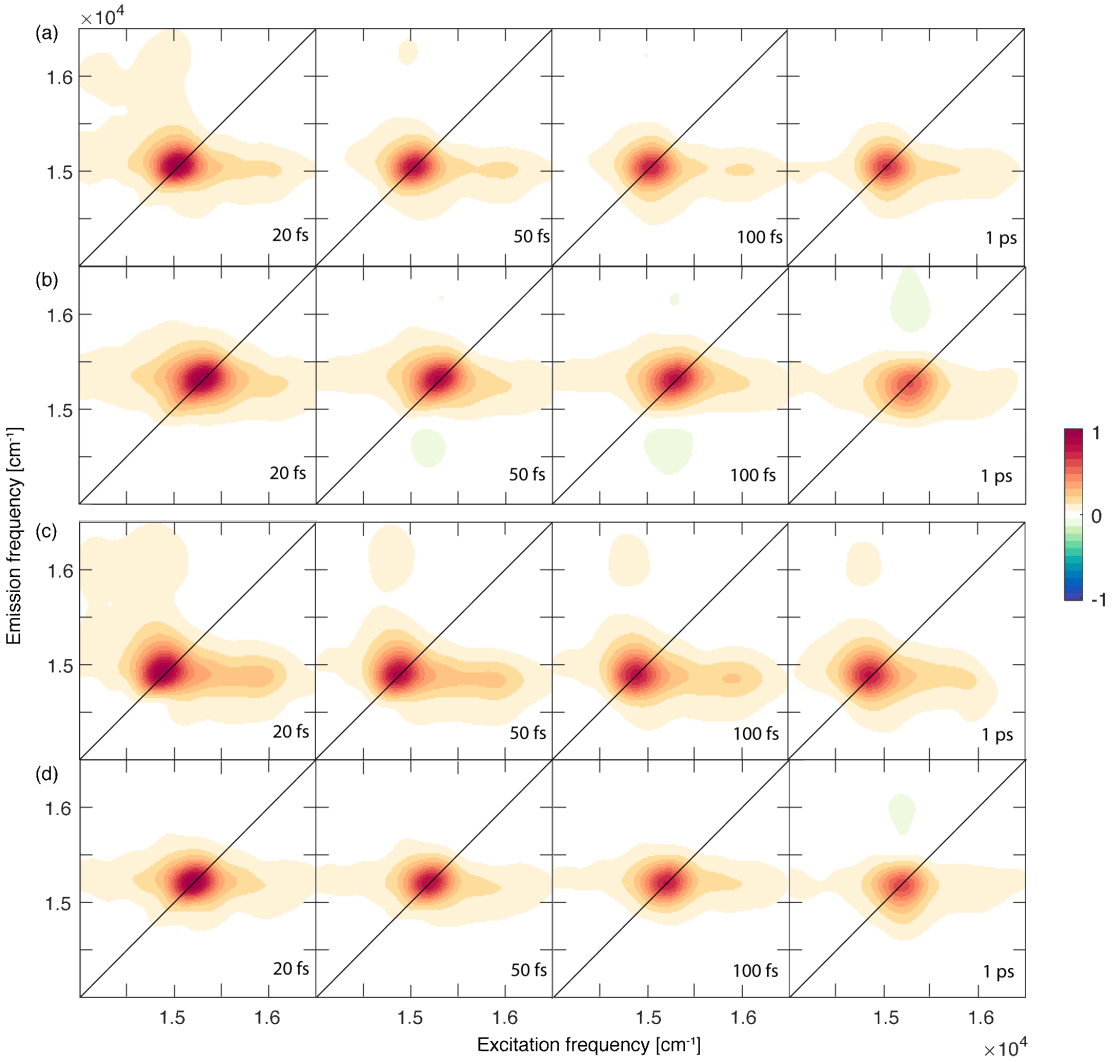

Figure 5.4: Evolution of 2DES maps at RT at selected values of population time t_2 for (a) Lv-*a*, (b) Lv-*b*, (c) Bo-*a*, and (d) Bo-*b*. Adapted from Ref. [118].

ence of vibrations coupled with the main electronic transition, as also witnessed by the evident vibronic progression in the absorption spectra. Due to the broadening effects of the signal, it is not possible to distinguish contributions from different excitonic states.

To clarify the dynamics underlying the time evolution of the 2DES response at RT, the data have been analyzed through a global multi-exponential fitting procedure where the first 15 fs were omitted in order to exclude possible artifacts arising from pulse superposition. The fitting results are visualized in terms of 2D-DAS in Figure 5.8 for Lv-*a* and Bo-*a* and in Figure 5.9 for Lv-*b* and Bo-*b*. The global fitting analysis for all the samples revealed two non-oscillating decaying components: one in the ultrafast timescale, ranging from 40 to 80 fs depending on the WSCP species, and

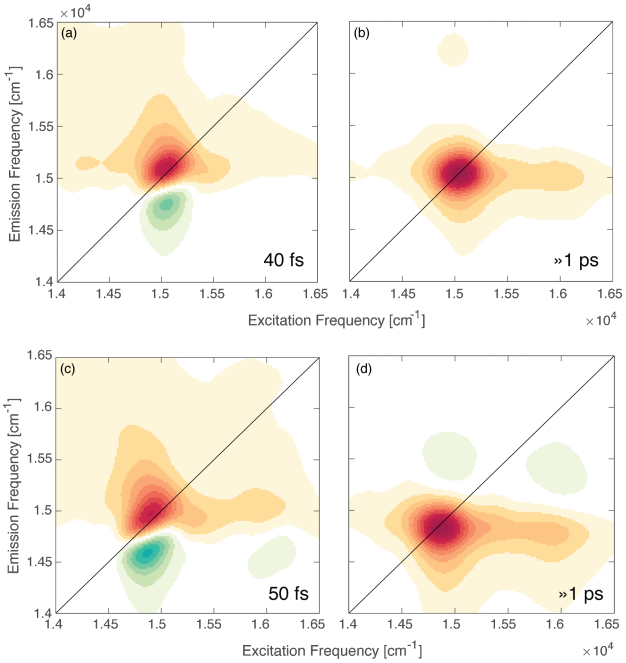

Figure 5.5: (a,b) 2D-DAS of Lv-*a* as obtained from the global fitting procedure of the 2DES data at RT. The associated time constants are reported in the panels.(c,d) 2D-DAS of Bo-*a* as obtained from the global fitting procedure of the 2DES data at RT. The associated time constants are reported in the panels.

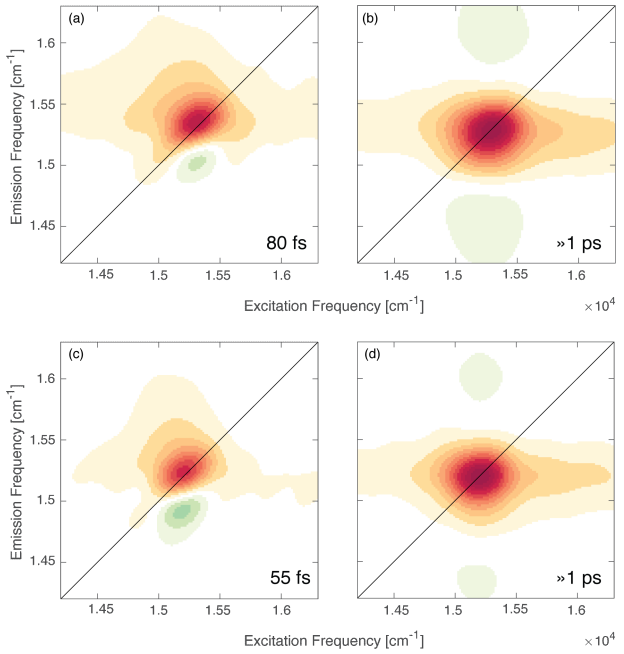

Figure 5.6: (a,b) 2D-DAS of Lv-*b* as obtained from the global fitting procedure of the 2DES data at RT. The associated time constants are reported in the panels.(c,d) 2D-DAS of Bo-*b* as obtained from the global fitting procedure of the 2DES data at RT. The associated time constants are reported in the panels.

the other one with a much longer time constant (>1 ps). For all WSCP samples, the longer component has a time constant much longer then the time window explored in the experiment. This behavior can be described as the relaxation of the whole system to the ground state after the laser pulses excitation. Regarding the ultrafast component, in all WSCP samples, the associated amplitude distributions show a positive amplitude signal in correspondence of the diagonal peak and a negative signal below the diagonal, which is a marker of relaxation processes from higher to lower energy state. The associated time constants are in good agreement with the calculated lifetime of 50-80 fs reported in the literature for homodimers of Chl *a* in WSCP [121]. At RT, no differences in the relaxation dynamics of Chl *a*- and Chl *b*-binding WSCPs can be observed.

5.5.2. Measurements at 77 K

Figure 5.7 shows the evolution of the 2DES signal as a function of the population time at 77 K. As for RT measurements, the main feature in the 2D maps is a diagonal peak due to ground state bleaching and stimulated emission of the electronic transitions addressed by the exciting pulses. However, at 77 K several features on and off diagonal can be observed. From a qualitative point of view, it is evident that the different broadening of the signals along the diagonal shows the same trend already observed in the absorption spectra where Lv samples and, in particular, Lv-*b* is characterized by the broadest bandwidth. Moreover, both of the Chl *b*-reconstituted samples are characterized by a more complex signal distribution than their analogs binding Chl *a*. For instance, while for Bo-*a* just two diagonal peaks can be identified at about 14600 and 14800 cm^{-1}, for Bo-*b* four signals can be clearly identified at about 14620, 14900, 15300 and 15650 cm^{-1}. Furthermore, especially at early times, cross peaks across these features can also be ascertained.
As for RT measurements, also in this case we applied the global multi-exponential fitting procedures used before to disentangle different underlying dynamics.
Focusing first on the non-oscillating population dynamics, the fitting results are shown in Figure 5.8 for Lv-*a* and Bo-*a* and in Figure 5.9 for Lv-*b* and Bo-*b*, where we reported the 2D-DAS associated with each time constant of the fitting.
For Lv-*a* and Bo-*a*, the global fitting analysis revealed very similar kinetics described by a bi-exponential decaying behaviour, as can also be deduced from the decay traces extracted at selected coordinates (Figure 5.8(c)-(f)). The first component has a time constant of about 100 fs for both samples. As already discussed for the mea-

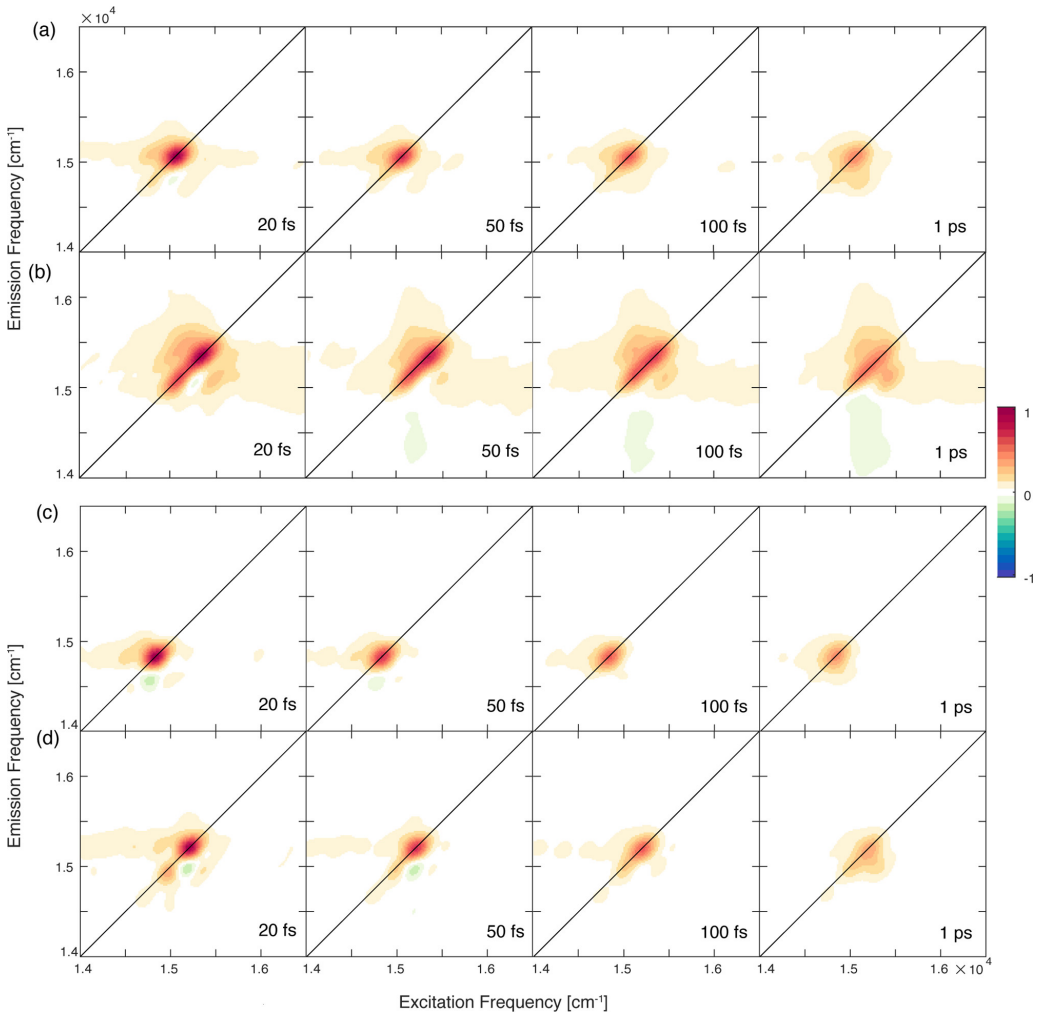

Figure 5.7: Evolution of 2DES maps at 77 K at selected values of population time t_2 for (a) Lv-a, (b) Lv-b, (c) Bo-a, and (d) Bo-b. Adapted from Ref. [118].

surements at RT, the associated amplitude distributions (Figure 5.8 (a)-(d) for Lv-*a* and Bo-*a*, respectively) shows a positive amplitude signal in correspondence of the diagonal peak and a negative signal below the diagonal, whose typically attributed to relaxation dynamics from higher to lower energy states [88, 95]. Actually, the position of this negative signal along the excitation and the emission axes suggests that a relaxation from the higher to the lower excitonic state is involved. The assignment of this kinetic constant to exciton relaxation is also in agreement with previous experiments on wild type class IIb WSCP [121]. The coordinates of the positive and negative signals in the 2D-DAS allow us to estimate the excitonic energy gap between the initial and the final states. In both proteins, this gap is ~ 220 cm^{-1}, which is in good agreement with the estimate of the coupling V based on the dipole-dipole interaction and on the geometrical assembly, reported in Section 5.2 (ΔE = 2V, ~ 204 and ~ 216 cm^{-1} for Lv-*a* and Bo-*a*, respectively).
The second time constant (> 1 ps) (Figure 5.8(b)-(e)) describes all the relaxation dynamics characterized by timescales longer than the investigated time window.
The behavior of the samples binding Chl *b* is quite different. In this case, the fitting procedure required three time components to reasonably fit the experimental time behavior for both samples. In addition to the first two time constants very similar to what was found for Lv-*a* and Bo-*a* ($\sim$ 110 fs and >1 ps), a third ultrafast component of about 10 fs was found. The necessity of a three exponential fitting is also clearly recognizable by the corresponding time traces extracted from the diagonal and off-diagonal coordinates (Figure 5.9(d)-(h)), where the presence of an additional ultrafast component is particularly evident, especially at cross-peaks coordinates (red traces).
The 2D-DAS relative to the first two components are very similar to the corresponding ones found for Lv-*a* and Bo-*a* (Figure 5.9(b)-(c),(f)-(g)). Therefore, a similar origin of the associated dynamic phenomena can be suggested, even if the broader distribution of the signals in these DAS already indicates that, in Lv-*b* and Bo-*b*, the excitonic states involved in the relaxation dynamics are more spread in energy than those in Lv-*a* and Bo-*a*.

The 2D-DAS of the shortest time constant presents a complex distribution of signals in both samples. For Lv-*b*, signals at diagonal and cross-peak positions between coordinates 14660, 15050, 15400, and 15660 cm^{-1} are identified, as pinpointed by the gray lines in Figure 5.9(a). Similarly, in Bo-*b*, diagonal and cross-peak positions between coordinates 14620, 14900, 15300, and 15650 cm^{-1} can be identified (Figure 5.9(e)). The positive amplitude at these coordinates means that the signal decays

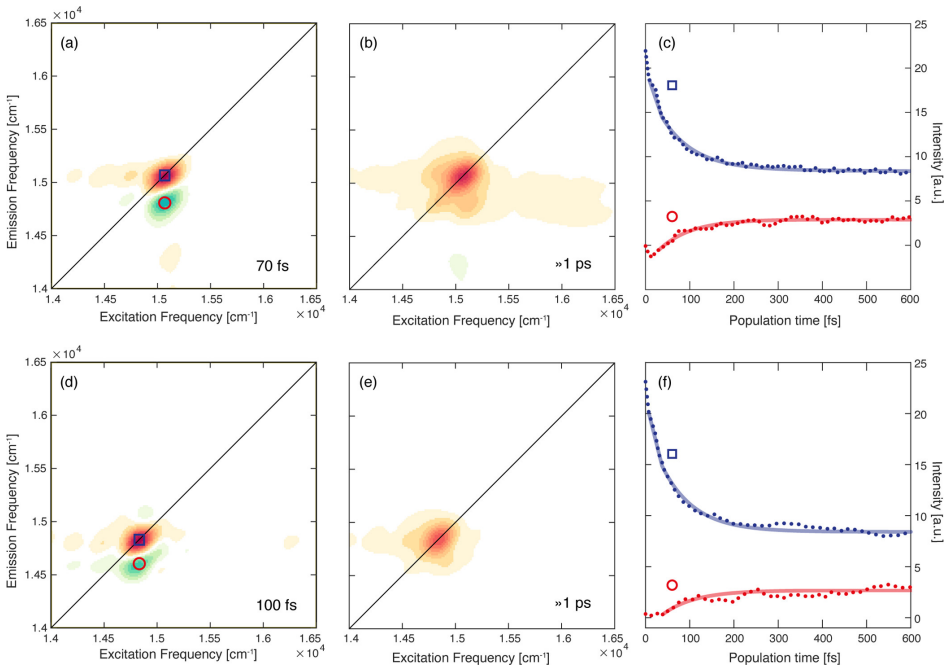

Figure 5.8: (a,b) 2D-DAS of Lv-*a* as obtained from the global fitting procedure of the 2DES data at 77 K. The associated time constants are reported in the panels. (c) Decay of the signal extracted at coordinates pinpointed by the blue square (15070, 15070) cm^{-1} and red circle (15070, 14850) cm^{-1}. Dotted lines: experimental data; solid lines: fitting curves. (d–f) Same as before for Bo-*a*. The coordinates pinpointed by the blue square are (14830, 14830) cm^{-1}, and those pinpointed by the red circle are (14830, 14600) cm^{-1}. Adapted from Ref. [118].

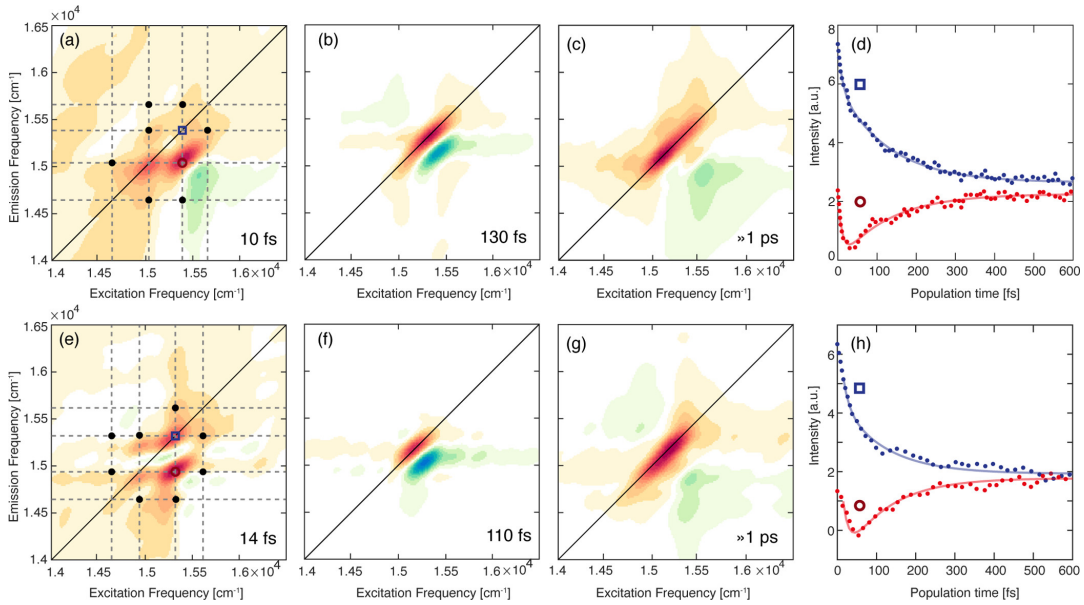

Figure 5.9: (a–c) 2D-DAS of Lv-*b* as obtained from the global fitting procedure of the 2DES data at 77 K. The associated time constants are reported in the panels. In panel a, the circles highlight the positions of the most intense cross peaks. (d) Decay of the signal extracted at coordinates pinpointed by the blue square (15400, 15400) cm^{-1} and red circle (15400, 15660) cm^{-1}. Dotted lines: experimental data; solid lines: fitting curve. (e–h) Same as panels a–d for Bo-*b*. The coordinates pinpointed by the blue square are (15300, 15300) cm^{-1}, and those pinpointed by the red circle are (15300, 14900) cm^{-1}. Adapted from Ref. [118].

with a characteristic time of 10 fs. These dynamics are attributed to the ultrafast dephasing of coherent superpositions of excitonic states instantaneously prepared by the exciting pulses. Since the time constant characterizing this process is very similar to the time resolution of the experiment, we can only deduce that these superpositions immediately dephase after photoexcitation; for this reason, no functional meaning can be attributed to these overdamped coherences. However, the amplitude distribution of the signal allows us to pinpoint with greater precision the energies of the excitonic states involved in the early times of the relaxation dynamics [47]. The coordinates of the signals appearing in the 2D-DAS of Figure 5.9(a) and (e) can thus be used as an estimate of the energy of the excitonic states. In both Chl *b* complexes, the presence of four excitonic states can be reasonably assessed. The energy of diagonal features corresponds with the position of the weak shoulders previously identified on the red side of the absorption spectra at 77 K (Figure 5.2). Moreover, the presence of signals appearing immediately after photoexcitation and at cross-peak positions between the main diagonal peaks at symmetric positions with respect to the diagonal (pinpointed in Figures 5.9(a)-(e) with black dots) is the typical manifestation of excitonic coupling [23, 47]. The presence of four dis-

tinguishable signals suggests that the four Chl *b* molecules in Lv-*b* and Bo-*b* cannot be simply considered as a pair of dimers; rather, they constitute a tetramer with non-negligible couplings among all four pigments. This was also suggested by optically detected magnetic resonance experiments [122]. The energy separations among the excitonic states in both Chl *b* samples are significantly higher than the energy gaps estimated from the calculation of the dipole-dipole coupling V ($\Delta E \approx 134$ cm^{-1} for both Lv-*b* and Bo-*b*) and also higher than the ones measured in Chl *a* samples. Assuming that the X-ray structure is providing the correct angles and distances, the error in the estimate of the coupling V may derive from a wrong initial estimate of the Chl *b* transition dipole moment, clearly not corresponding to the transition dipole moment of the isolated Chl *b* pigment in solution, unlike the case of Chl *a*.
This peculiar property of Chl *b* was already observed in previous experiments by analyzing the extinction coefficient of Chls *a* and *b* upon binding to the WSCP. Indeed, Palm et al. [108] noticed that Chl *b* embedded in the wild-type WSCP from either *B. oleracea* or *L. virginicum* exhibits an unexpectedly high molar extinction coefficient when compared with the corresponding Chl *a*-reconstituted complexes. This finding seems to point to a particularly large transition dipole moment of Chl *b* upon its binding to the WSCP. The only structural difference between Chl *a* and Chl *b* pigments is the presence of the formyl group in Chl *b* at the C7 position. It is already known that the formyl group modifies the optical properties of the chromophore [123] and can significantly contribute to the binding of Chl *b* to proteins, also thanks to the formation of H-bond networks [124–126]. Carbonyl groups can also modify the charge distribution and thus the transition dipole moment through polarization effects or the formation of H-bonds [127, 128]. These two mechanisms are typically correlated and not easily distinguishable in complex media [129]; however, the mere polarization effect can be excluded considering that the extinction coefficient of Chl *b* depends on the solvent's polarity in a manner comparable to Chl *a*. The most likely conclusion is that the electronic properties of the pigments (the transition dipole moment and then, in turn, also the electronic coupling and the excitonic energy gaps) are tuned by the presence of specific and directional interactions between the protein backbone and the formyl group on the Chl *b* moiety, mainly identified as H-bonds with specific amino acids, with or without the mediating action of a water molecule [29].
This implies a particularly interesting and not yet fully explored role of the scaffold in pigment-protein complexes, where the effects are not limited to variations of the site energies of the pigments.

5.6. Final remarks

In this work we have compared the ultrafast dynamics of four pigment-protein complexes, characterized two-by-two by the same protein scaffold but binding different pigments, chlorophyll *a* or *b*. From the structural point of view, as confirmed by the X-ray investigations, the four complexes are very similar with the only relevant difference being the possibility for Bo-*b* and Lv-*b* of establishing an additional H-bond through the formyl group of the Chl *b* in C7 position. Interestingly, it was found that the electronic coupling between pigments (and in turn also the energy gaps among excitonic states) can be correctly predicted based on geometrical considerations for Chl *a*-WSCPs, whereas strong deviations from the experiments are found for Chl *b*-WSCPs, where the geometrical prediction strongly underestimates the coupling. The different behavior has been justified by accounting for the possibility of involving the formyl group of the Chl *b* in C7 position in the formation of an additional H-bond with the protein backbone, with or without the mediating action of a water molecule. In conclusion, we have demonstrated that the establishment of specific and directional interactions can have very strong consequences for the electronic coupling and for the ultrafast dynamics of pigment-protein complexes. This is a particularly important finding because it implies the possibility of tuning the photophysics and the transport properties of multichromophores by engineering specific interactions with the surroundings. With respect to other supramolecular interactions, H-bonds appear to be particularly suited for this control task because of the possibility of more easily predictable orientations, distances, and geometries. For this purpose, in the following Chapter, we explore the role of H-bonds in tuning the ultrafast dynamics of molecules by studying a specifically engineered H-bonded molecular dimer.

6 | BODIPY

6.1. Introduction

In the previous Chapter, we demonstrated that the establishment of specific interactions, like H-bonds, could tune the electronic couplings of pigments and affect the ultrafast dynamics of pigment-protein complexes. These results suggested that it could be possible to control the photophysics of multichromophoric systems by engineering specific interactions with the surroundings.
More specifically, H-bonds play an essential role in many photophysical processes. While the effects of H-bond interactions on the ground state dynamics have been widely investigated, less information is reported on the role of H-bonding in the electronic excited state. It is known that, upon photoexcitation of the H-bonded systems, a reorganization of hydrogen donor and acceptor molecules takes place due to the significant charge distribution difference between different electronic states [35]. This reorganization process controls the excited-state dynamics of H-bonded complexes in a crucial way, activating or facilitating many photophysical processes. [36, 40]. The electronic excited state H-bonding dynamics are principally determined by the vibrational motions of the hydrogen donor and acceptor groups and generally occur on ultrafast time scales of hundreds of femtoseconds.
Starting from these findings, we studied a specifically engineered H-bonded molecular dimer with the aim of verifying to what extent the presence of H-bonds could affect the ultrafast dynamic relaxation in the excited state. In particular, we investigated an H-bonded molecular dimer prepared by self-assembly of two boron-dipyrromethene (BODIPY) dyes driven by the formation of a triple H-bond (Figure 6.1(a)).
BODIPY molecules are a family of fluorescent molecules used for a very large number of applications due to their structural versatility and spectroscopic properties [130, 131]. The core of the chromophore consists of two pyrrole rings connected by a methene bridge and a boron atom coordinated to two fluorine atoms [132].

The spectroscopic and photophysical properties of BODIPY dyes can be fine-tuned by a direct functionalization of the core at proper positions shifting the absorption from wavelengths of about 500 nm up to the NIR region. In this work, distyryl-functionalized BODIPY has been used to push the absorption spectrum in a spectral region convenient for the 2DES measurements (550 nm–750 nm).
Moreover, also the two isolated BODIPY monomer molecules have been investigated in order to verify the presence of ultrafast dynamic processes specifically triggered by the establishment of H-bonds between the two monomeric units.

6.1.1. Design of the H-bonded dimer

The H-bonded dimer was prepared according to the method previously published [133] and kindly provided by Prof. Cordaro, Università di Messina. In order to promote the formation of an H-bonded dimer, the donor and acceptor molecules were designed by introducing at the meso position of a distyryl-BODIPY moiety one-butyl-uracil (URA) and 2,6-diacetamido pyridine (DAAP) groups, respectively. The two molecules, denoted from now on as URA-BODIPY and DAAP-BODIPY, respectively, were prepared starting from the respective aldehydes used as precursors. The dimer has been prepared by mixing equimolar concentrations of URA-BODIPY and DAAP-BODIPY. The dimer formation has been monitored and confirmed by ^{1}H NMR spectroscopy, following the changes in the chemical shift values of the hydrogen atoms involved in the H-bond formation.

6.2. Experimental Methods

DAAP-BODIPY, URA-BODIPY and the dimer, prepared as described in the previous section, were diluted in anhydrous chloroform ($CHCl_3$), until reaching an optical density of about 0.3 at the absorption maximum in a 1 mm cuvette. TA measurements were performed with the setup described in Section 2.1.2.1. TA spectra were recorded in 0.1 ps steps in a time window from - 3 to 1000 ps and their quality was improved by repeating and averaging measurements 250 times to obtain a sufficient signal-to-noise ratio. For 2DES experiments, the laser spectrum was centered at 15500 cm^{-1} (645 nm). The pulse duration was compressed to 8 fs, corresponding to a spectral bandwidth of about 1840 cm^{-1}. The pulse energy was 7 nJ at the sample position. The population time (t_2) was scanned from 0 to 1000 ps in steps of 7.5 fs, with each experiment repeated at least five times to ensure reproducibility. Steady-

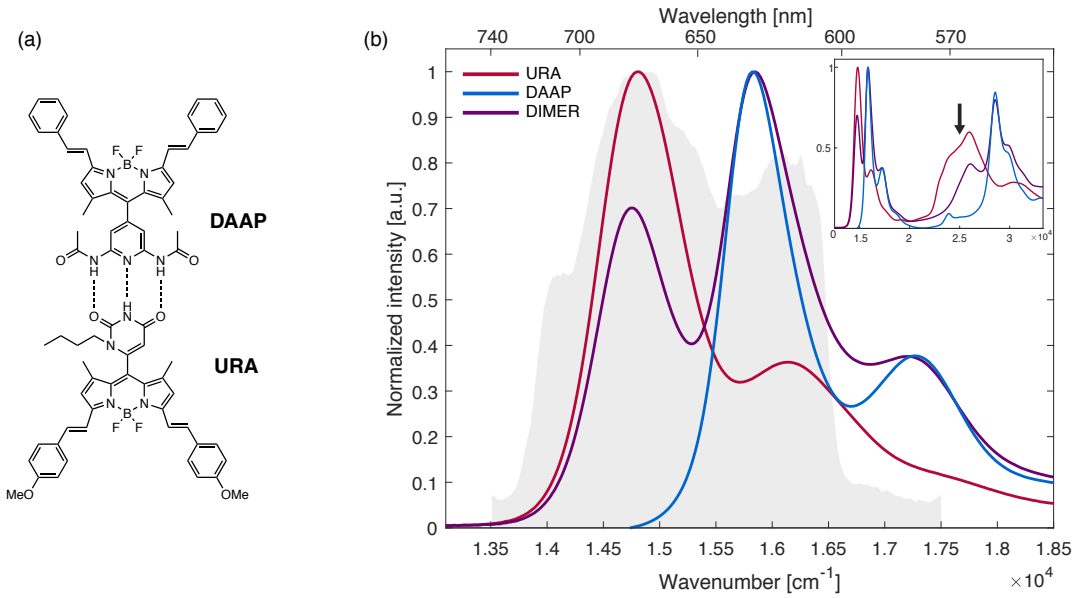

Figure 6.1: (a) Molecular structure of the H-bonded dimer (b) Normalized absorption spectra of DAAP-BODIPY (blue), URA-BODIPY (red), and dimer (purple) in the 550 nm–750 nm spectral range. The gray area represents the laser spectrum profile used in the 2DES experiments. In the inset, the spectra in the full visible range are reported and the arrow indicates the excitation wavelength in transient-absorption experiments. Adapted from Ref. [134].

state absorption spectra were acquired before and after each scan to control that no degradation of the sample happened during the TA and the 2DES measurements.

6.3. Linear characterization

The linear absorption spectra measured for DAAP-BODIPY, URA-BODIPY and the dimer dissolved in anhydrous $CHCl_3$ are reported in Figure 6.1(b). The spectra of the two monomers shows the characteristic absorption bands of BODIPY chromophores [131]. The main absorption band at 15820 cm^{-1} (632 nm) and at 14810 cm^{-1} (675 nm) for DAAP-BODIPY and URA-BODIPY, respectively, is assigned to $S_0 \rightarrow S_1$ 0-0 transition. Additionally, the pronounced shoulders at higher energies can be identified as vibronic progression composed of several vibrational states. The excitations to higher energy electronic states are usually less permitted and appear as weaker broad bands at shorter wavelengths, as shown in the inset of Figure 6.1(b) [131].

The absorption spectrum of the dimer turns out to be a combination of the spectra of the two monomers: it shows two main absorption bands at 15850 cm^{-1} (631 nm) and 14750 cm^{-1} (678 nm), slightly shifted with respect to the ones of the two iso-

lated monomers. These little spectral shifts may be linked to the formation of the hydrogen bonds, which are known to have relatively small effects on the linear absorption spectra [44]. The presence of hydrogen bonds in the dimer does not seem to induce a significant electron coupling between the two monomers, as confirmed by the spectral features of the dimer, which appear to be a mere sum of those of the single chromophores. The same behaviour was also ascertained in other spectroscopic measurements, like steady-state and time-resolved fluorescence [133].

6.4. Transient Absorption Spectroscopy

The TA spectra recorded at selected values of the delay time for all the samples are reported in Figure 6.2. For both monomeric DAAP-BODIPY and URA-BODIPY, the excitation at 400 nm leads to the formation of negative ground state bleaching (GSB) features associated with the $S_0 \rightarrow S_1$ electronic transition and the relative vibronic progressions (negative signals at 632 nm and 588 nm for DAAP-BODIPY and 675 nm and 625 nm for URA-BODIPY). Moreover, in both cases, a broad positive excited state absorption (ESA) signal related to $S_1 \rightarrow S_n$ transition is present at shorter wavelengths.
The TA spectrum of the dimer is similar to the TA spectrum of URA-BODIPY; this is expected considering that at the excitation wavelength of 400 nm, the absorption spectrum of the dimer is dominated by the absorption features of the URA-BODIPY monomer.
The time traces of both monomers can be fitted with a bi-exponential kinetic model. The fastest component (120 fs for URA-BODIPY and 160 fs for DAAP-BODIPY) is assigned to the formation of the S_1 state after relaxation from the higher energy state populated with the excitation of the pump at 400 nm ($S_{400} \rightarrow S_1$). The longer component has a time constant >1 ns, which could not be determined with better precision since it is much longer than the investigated time window. This decay corresponds to the relaxation process from S_1 to the ground state S_0.
Also for the dimer, the time evolution could be fitted with a bi-exponential model with time constants of 140 fs and >1 ns. The longest time constant describes the same relaxation process happening in both monomers. Nevertheless, although the value of the shortest time constant is very similar to the ones found for the monomeric species, the temporal response of the dimer cannot be explained as a mere sum of the behaviors of the two non-interacting chromophores. This is especially evident in the 600 nm–640 nm region, as also illustrated by the decay traces of the dimer

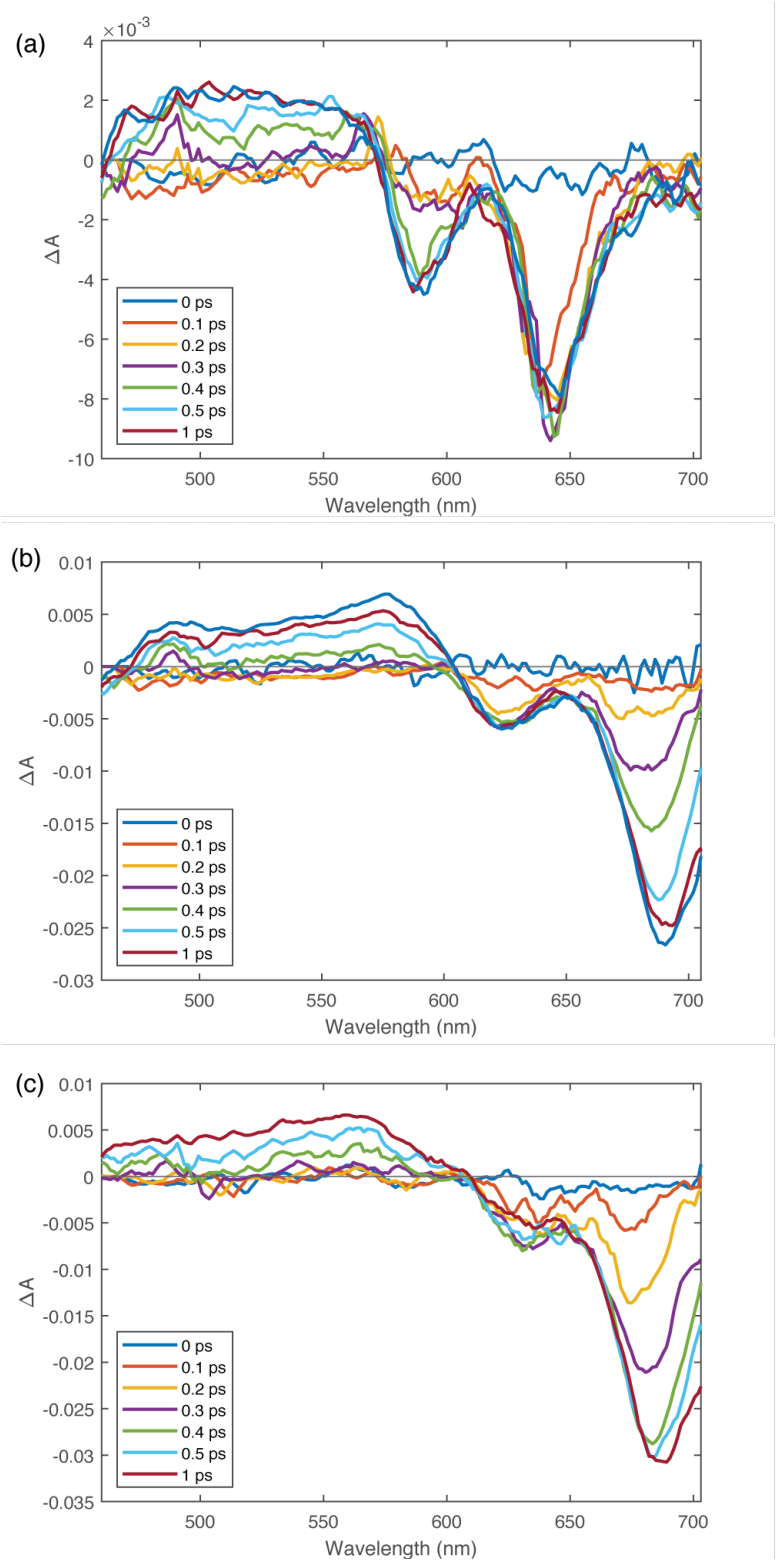

Figure 6.2: Transient absorption spectra (ΔA vs probe wavelength) at selected values of delay time for (a) DAAP-BODIPY, (b) URA-BODIPY and (c) dimer. Adapted from Ref. [134].

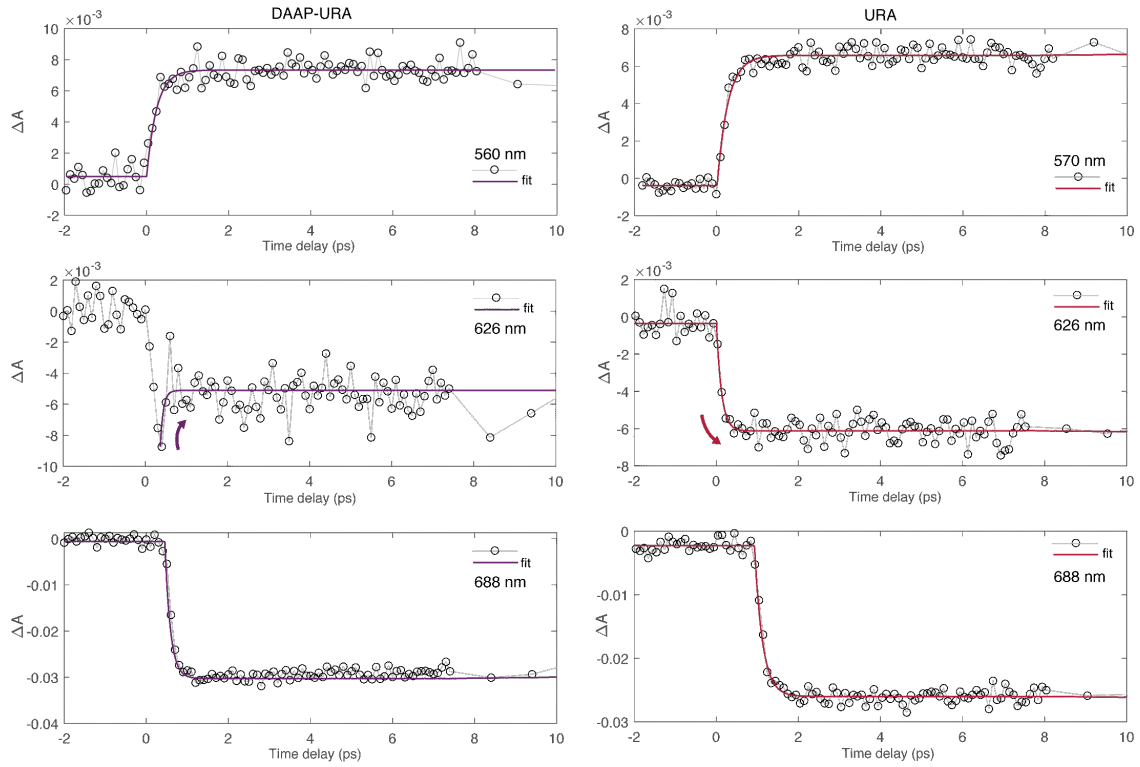

Figure 6.3: Decay traces (ΔA vs. time delay) extracted at relevant probe wavelengths (560, 626 and 688 nm) for the dimer (left column) and URA-BODIPY monomer (right column). The dots denote experimental points, while colored thick lines represent the result of the bi-exponential fitting. Curved colored arrows highlight the decaying (growing) contribution of the ultrafast time component in the dimer (URA-BODIPY). Adapted from Ref. [134].

and the URA-BODIPY monomer at 626 nm, reported in Figure 6.3. In the decay trace of the monomer the shortest time component contributes as a growing contribution to the overall relaxation dynamics; on the contrary, in the same spectral region, where, for the dimer, there is a good overlap between the spectral features of the two monomers, the shortest ultrafast time component contributes to the overall relaxation dynamics as a decaying contribution. These findings seem to suggest that, at wavelengths where there is a good overlap between the spectral features of the two BODIPY moieties, a new dynamic process, not present in the isolated monomers, is activated upon dimer formation, likely associated with a relaxation involving both URA- and DAAP-BODIPY moieties.

However, we cannot make any assignment of the mechanism considering the limited time resolution of the pump–probe technique and the overlap between the GSB features of two monomers, which sum up in the dimer. For these reasons, 2DES measurements have been employed to help clarify these complex dynamics.

6.5. 2DES characterization

6.5.1. Results and discussion

Figure 6.4 shows the evolution of the 2DES signal at selected values of population times for the three BODIPY samples.

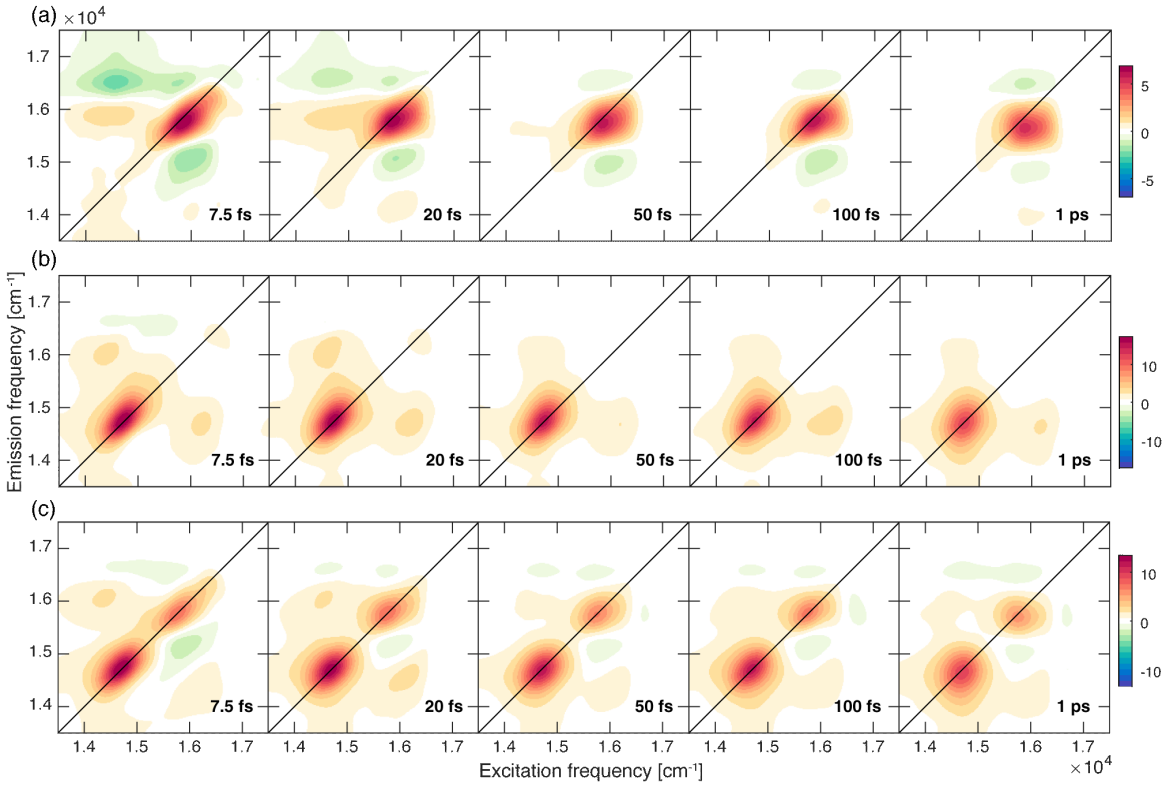

Figure 6.4: Evolution of purely absorptive 2DES maps at selected values of the population time for (a) the DAAP-BODIPY monomer, (b) URA-BODIPY monomer, and (c) dimer. Adapted from Ref. [134].

For the DAAP-BODIPY, the laser spectrum covers the 0-0 absorption band. The 2D maps show a positive diagonal peak, originated by the ground state bleaching (GSB) and stimulated emission (SE) of the S_1 state and compatible with the position of the maximum of the absorption spectrum. In addition, two negative peaks can be detected at symmetric upper and lower diagonal positions, which can be explained as excited-state absorption (ESA) signals towards higher energy states, as already observed in TA spectra. The diagonal signal, initially elongated along the diagonal, becomes more rounded and red-shifted, at increasing values of population time. According to previous literature [135], after photoexcitation, the S_1 state quickly relaxes as a result of inter- and intramolecular vibrational energy redistribution and

solvent reorganization, leading to a shift of stimulated emission to lower energy, also known as dynamic Stokes shift [85, 136]. At the same time, the two negative signals gradually lose intensity; for the peak below diagonal, this is also motivated by the growth of the positive peak in the same spectral region, which counterbalances the negative ESA signal.
The relaxation dynamics of URA-BODIPY is very similar to the one of the DAAP-BODIPY. Small differences can be related to the different overlap conditions between the absorption spectrum and the exciting laser profile, which, for this sample, covers both the main absorption band and the vibronic progression. As for the DAAP-BODIPY, the 2D maps are dominated by a positive diagonal peak, attributed to GSB and SE of S_1 state. As the population time increases, the signal, elongated at early times, evolves to a more circular shape and slightly red shifts, as for the DAAP-BODIPY monomer. In this case, there is no evidence of negative signals in the region above and below diagonal. Nonetheless, the presence of positive cross-peaks can be detected at symmetric off-diagonal positions. These cross-peaks are typically associated with the excitation of vibrational modes, strongly coupled with the main transition [137].
The 2DES response of the dimer manifests a richer profile as a result of the combination of the response of the two monomers composing the dimer. At a first inspection, the 2D maps of the dimer appear as a sum of the responses of the two monomers.
To clarify the underlying dynamics and highlight possible differences between the behavior of the monomers and the dimer, we performed a global multi-exponential fitting procedure [67].
Focusing first on the non-oscillating population dynamics of the two monomers, the data could be fitted with a bi-exponential decaying behaviour, in agreement with what has already been reported in the literature [95]. For both DAAP-BODIPY and URA-BODIPY monomers, the fitting analysis revealed two time constants of about 15 fs and >1 ps. The associated 2D-DAS are reported in Figure 6.5. The longer time constant (>1 ps) describes the decay dynamics to the ground state of the entire system, which happens in a timescale much longer than the investigated time window, as also confirmed by pump-probe experiments. For the DAAP-BODIPY monomer, these dynamics also include the ESA signal above and below diagonal, whose intensity progressively decays with the same time constant.
Concerning the ultrafast component, the associated 2D-DAS can be interpreted as a combination of the spectral diffusion process [85] and the relaxation from the vertically excited Franck-Condon state toward a relaxed electronic configuration, me-

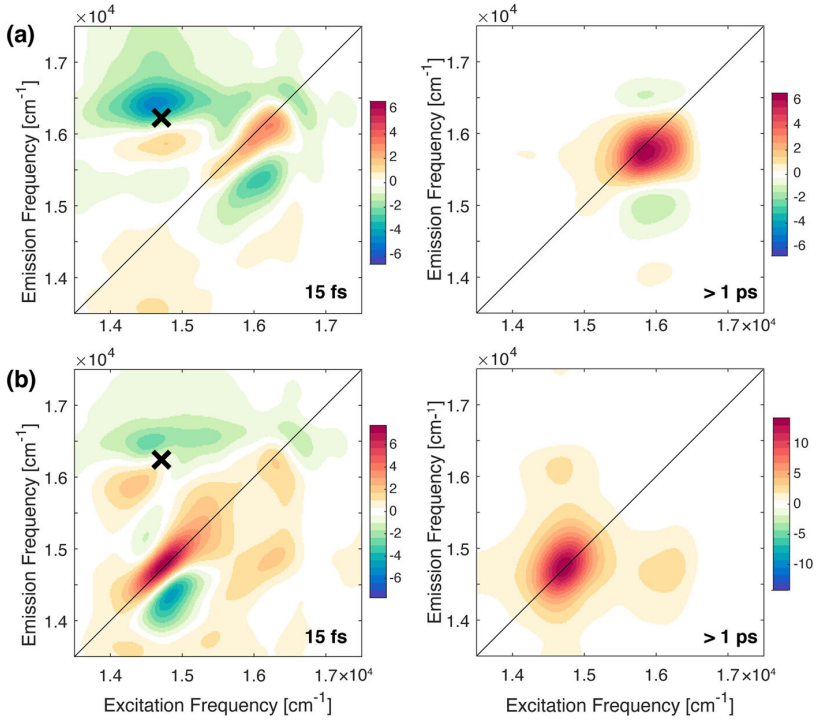

Figure 6.5: 2D-decay associated spectra (2D-DAS) resulting from the global fitting of the 2DES maps for (a) DAAP-BODIPY and (b) URA-BODIPY monomers. The associated time constants are reported in each panel. The black cross marks the non-resonant contribution of the solvent at early times. Adapted from Ref. [134].

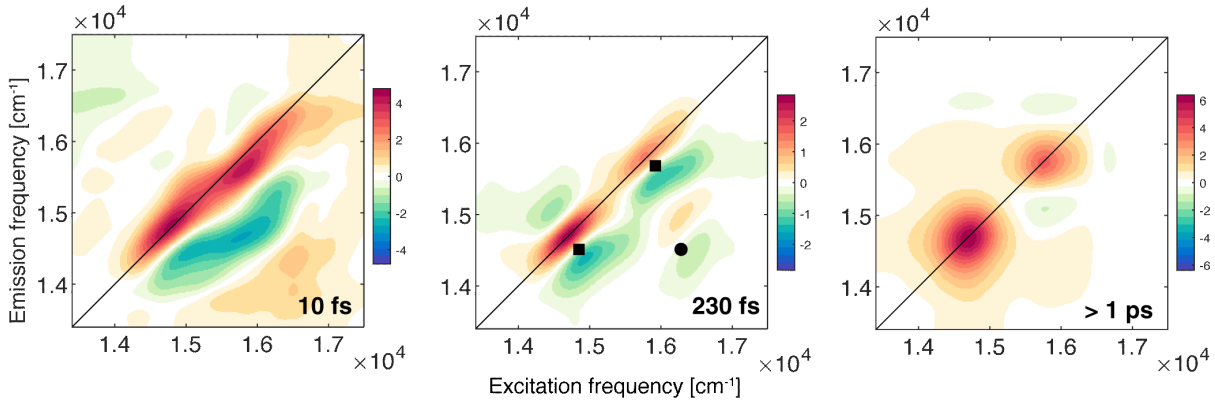

Figure 6.6: 2D-decay associated spectra (2D-DAS) resulting from the global fitting of the 2DES maps for the dimer. The associated time constants are reported in each panel. Square and circle markers pinpoint relevant signals commented in the text. Adapted from Ref. [134].

diated by solvent interactions [95]. Moreover, also the non-resonant contribution of the solvent can be observed in the upper diagonal position of the DAS (pinpointed with a black cross marker in Figure 6.5).

In contrast, the dynamics of the dimer required three exponential components to be fitted. The corresponding time constants are about 10 fs, 230 fs and >1 ps, whose associated 2D-DAS are reported in Figure 6.6.

The shortest and the longest time components describe the same dynamical processes already ascertained in both the monomeric species. On the contrary, the 2D-DAS related to the 230 fs time constant captures a dynamics totally absent in the monomers. It should also be noted that the presence of this additional ultrafast component has a time constant very similar to the one for the $S_{400} \rightarrow S_1$ process found in the TA spectra of the non-interacting monomers. This clarifies why, in the TA spectrum of the dimer, these additional relaxation pathway could not be fully distinguished from the intra-chromophore $S_{400} \rightarrow S_1$ paths and just gave rise to a different signal amplitude contribution in the 600–640 nm spectral region (Figure 6.3).

The 2D-DAS of the 230 fs component presents a complex distribution of signals. First, two positive diagonal peaks can be identified in conjunction with two negative signals below the diagonal (marked by squares in the second panel of Figure 6.6); as already reported in the literature, such a signal distribution represents a downward relaxation within an excited state manifold [95, 138],). In this case, we can identify a relaxation channel that involves each of the two chromophores separately since we find the same behavior at (14800, 14800) and (15800, 15800) cm^{-1} diagonal coordinates, corresponding to the energy of the S_1 state of the DAAP-BODIPY and

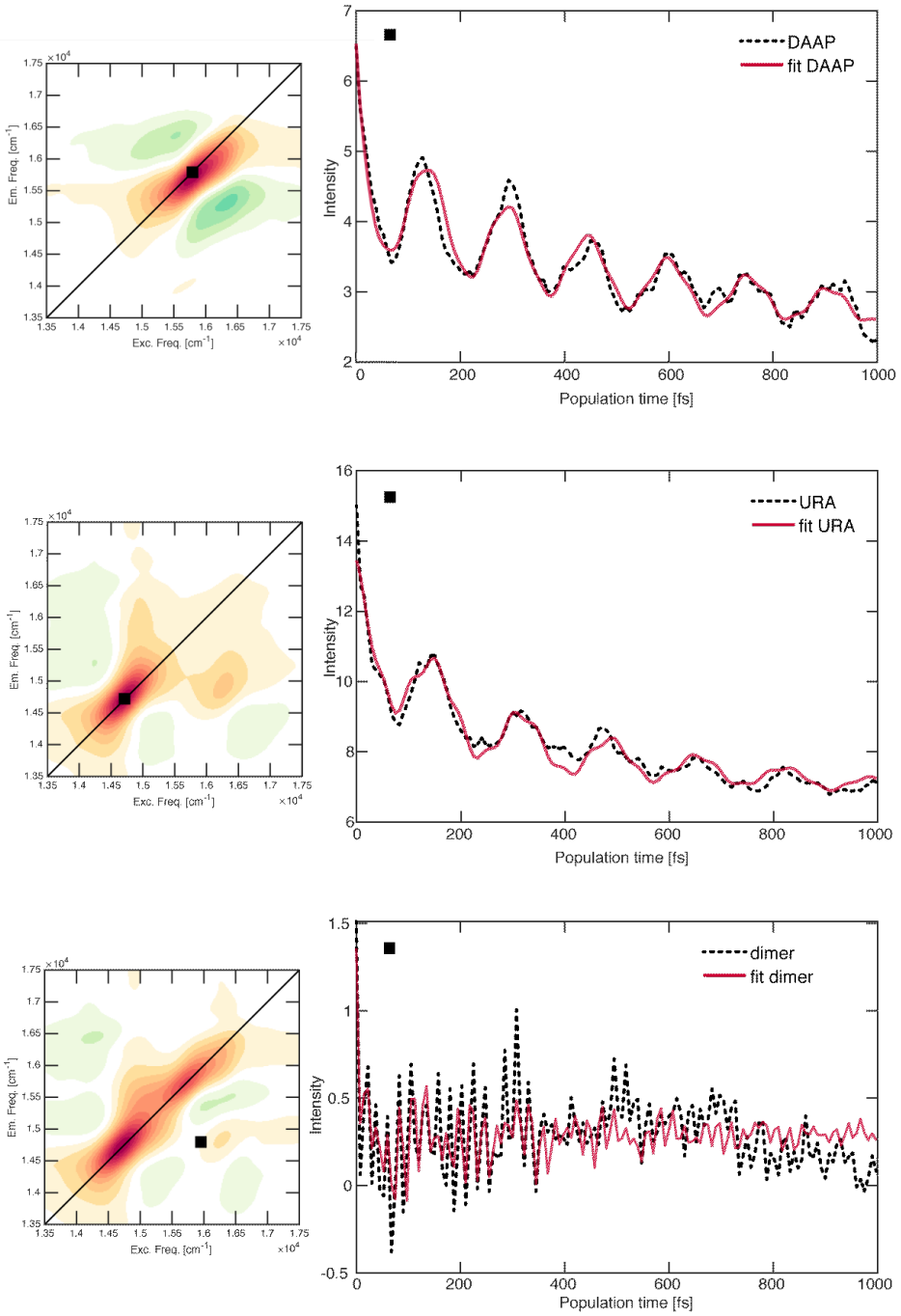

Figure 6.7: Signal decay (rephasing) as a function of population time, extracted at relevant coordinates pinpointed by the square marker in the 2D maps on the left. Black dashed lines represent the experimental signal, and the red solid lines are the result of the global fitting procedure. (a) DAAP-BODIPY, (b) URA-BODIPY, (c) dimer. Panels (a) and (b) show that the beating behaviour of the signal for the samples is dominated by low frequency modes of the chloroform solvent.

URA-BODIPY, respectively. Despite the intra-chromophore nature of the process, it appears to be activated only when the two monomers are coupled to form the dimer and shows the same dynamics for both chromophores.
In addition, a negative peak appears at cross-coordinates between the two monomeric S_1 states (circle in Figure 6.6). A negative signal at these coordinates denotes a population transfer from a state at about 16000 cm^{-1} (x-coordinate) to a state at about 14500 cm^{-1} (y-coordinate). This would suggest an inter-chromophore energy transfer from the S_1 of DAAP-BODIPY to the S_1 of URA-BODIPY, happening with the same time of 230 fs. Thus, it becomes clear that both these dynamics, the intra- and the inter-chromophore, are characterized by the same time constant, so they likely share a common origin. Concerning the nature of this inter-chromophore transfer, we can both exclude a Förster energy transfer mechanism, because the transfer happens in an ultrafast timescale, and an excitonic mechanism promoted by a strong coupling between the two monomers, considering the linear optical properties of the dimer and the inter-chromophore distance of about 1.5 nm, obtained from previous DFT calculation [133].
From previous literature, it is known that H-bonded chromophores might reveal additional ultrafast dynamics associated with transient H-bonding interactions taking place after photoexcitation [45]. It was also demonstrated that these dynamics are promoted by a reorganization in the electronic excited state driven by H-bonding dynamics [35], mostly determined by the vibrational motions of the H donor and acceptor groups [33, 139] and tipically occurring on time scales of hundreds of femtoseconds [140]. In light of this, we suppose that the 230 fs dynamics, present in the dimer response but absent in the non-interacting monomers, could be attributed to a process involving intra and inter-chromophore relaxation processes, significantly coupled with the H-bond dynamics.
This finding is also supported by the analysis of the beatings behaviour. The oscillating dynamics have been studied with the same global fitting methodology as well as Fourier analysis. The overall beating behaviour is illustrated by power spectra in Figure 6.8(a). For all the samples, the beatings are dominated by a strong non-resonant contribution of the chloroform vibrational modes (261 cm^{-1}, 363 cm^{-1}, 680 cm^{-1} e 1220 cm^{-1}) [141], as verified also superimposing the Raman spectrum of $CHCl_3$ (Figure 6.8(a)). These vibrational modes could also be noticed extracting the signal at relevant coordinates, as depicted in Figure 6.7.
It was, however, possible to recover additional beating components, reported in Table 6.1. The 2D-CAS for both monomers modes present the typical 'chair' pattern

Table 6.1: Vibrational modes of URA-BODIPY, DAAP-BODIPY and the dimer recovered from the Fourier analysis of the residuals.

	Frequency (cm^{-1})				
URA-BODIPY	1190 cm^{-1}	1280 cm^{-1}	1460 cm^{-1}	1500 cm^{-1}	1610 cm^{-1}
DAAP-BODIPY	1190 cm^{-1}	1253 cm^{-1}	1470 cm^{-1}	1670 cm^{-1}	
dimer	1200 cm^{-1}	1470 cm^{-1}	1660 cm^{-1}		

predicted for vibrational modes [86, 137, 142]. Figure 6.8(b) exemplifies this analysis for the mode at 1460 cm^{-1} recorded for the URA-BODIPY monomer. The higher amplitude of the signal located above the diagonal (negative frequencies) suggests a stronger contribution of this mode in the excited state. Also, the dynamic behavior of these beating modes supports their vibrational nature, presenting dephasing times in the order of ps. In the dimer case, the amplitude distribution depicted in the 2D-CAS is significantly different, as exemplified for the mode at 1470 cm^{-1} in Figure 6.8(c). These components contribute mainly to the 2DES signal below the diagonal at coordinates where the cross peak attributed to the 230 fs inter-molecular relaxation channel is found. All these modes can be attributed to vibrational modes involving functional groups and bonds implicated in the formation of H-bonds in the dimer. In particular, the frequencies at 1200 cm^{-1} and 1470 cm^{-1} are typically associated with vibrational modes of amino groups involving N–H bending and C–N stretching, while the mode at 1660 cm^{-1} is more strongly related to the C==O stretching [143, 144]. Their dynamic behavior is also peculiar, being characterized by damping times of about 150 fs, as quantified by the global fitting and visualized through time-frequency transform (TFT) analysis (Figure 6.8(d)). Therefore, all these findings point toward the effective presence of an active mediating role of the H-bonds in the ultrafast dynamics of the dimer. The envisioned mechanism provides that, after photoexcitation of the H-bonded dimer, a reorganization of the charge distribution occurs. This reorganization involves both intra- and inter-molecular processes, and it is driven by the vibrational motions of the H donor and acceptor groups.

6.6. Final remarks

The ultrafast dynamics of an H-bonded dimer of BODIPY chromophores has been characterized to verify if the presence of H-bonds could affect to some extent the

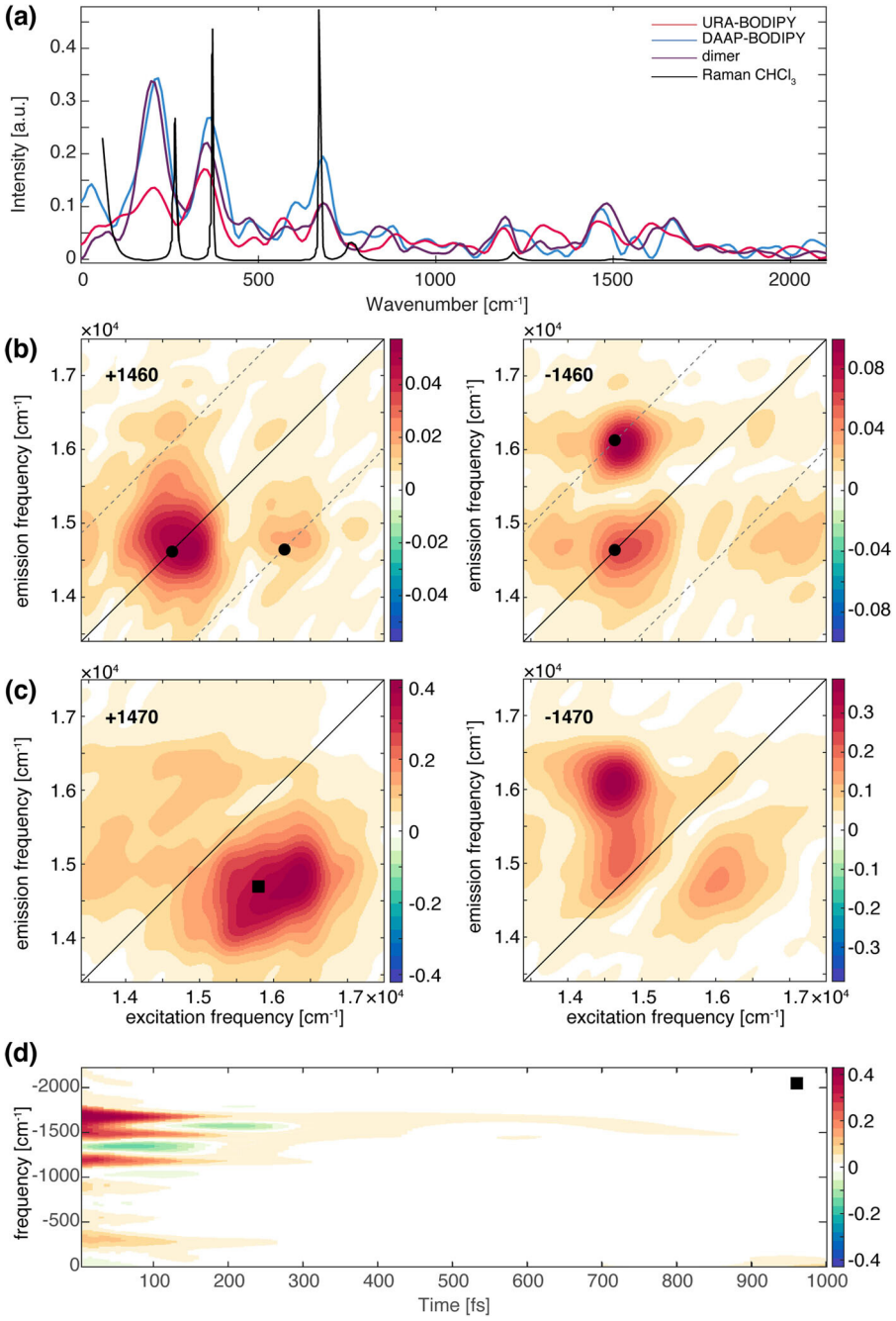

Figure 6.8: Beating analysis of the 2DES signals. (a) Power Fourier spectra for the three species. The Raman spectrum of the chloroform solvent is also reported for comparison (black line). (b) 2D-CAS obtained from the global fitting analysis of the URA-BODIPY monomer signal for a beating component with a frequency of ±1460 cm^{-1}. Analogous to 2D-DAS, the 2D-CAS show the amplitude distribution of a specific beating component in the 2D maps. Black dots pinpoint coordinates where vibrational modes are expected to contribute. (c) Same as (b) but for the dimer. (d) Time-frequency transform of the decay trace extracted at coordinates (16000, 14700) cm^{-1} corresponding to the square in panel (c). Adapted from Ref. [134].

relaxation dynamics in the excited state. To prove that, pump-probe and 2DES measurements were performed on the dimer and on both the monomeric units composing the dimer. We found that the formation of a dimer opens up a new ultrafast relaxation channel, characterized by a time constant of about 200 fs.
We verified, exploiting 2DES multidimensionality, that this new relaxation dynamic is determined by two kinds of processes. First, an "intra-molecular" relaxation pathway involves the two chromophoric moieties separately but simultaneously. Second, we detected an “inter-molecular” relaxation mechanism, which involves the transfer of population from the S_1 of DAAP-BODIPY to the S_1 of URA-BODIPY. The analysis of the beating behavior of the 2DES signals, mainly connected with nuclear motions, revealed the presence of peculiar properties: (i) they are most likely linked with functional groups involved in the H-bonds formation, (ii) they contribute mainly at a cross-peak position where an inter-molecular transfer mechanism has been identified and they do not present the typical amplitude distribution expected for vibrational modes, and (iii) the beating dynamics associated with these modes are damped in the same timescale of this inter-molecular transfer process. It is likely to conclude that the formation of H-bonds activates new ultrafast dynamic channels in the relaxation dynamics of the dimer involving intra- and inter-molecular mechanisms. The activation of an inter-molecular mechanism is particularly significant considering the very weak interaction of the two BODIPY molecules and the considerable distance between their centers of mass. This indeed suggests that the design of H-bonded structures is a particularly powerful tool to drive the ultrafast dynamics in complex materials.

7 | Action-based Spectroscopy

7.1. Theory

Through the years, multidimensional optical spectroscopy has proved to be decisive for the investigation of the ultrafast dynamics of complex systems. As shown in the previous chapters, he success of this technique is strictly linked to the possibility of following the evolution of a system both in time and frequency and to the feasibility of directly observing couplings between states [46]. Over the last decades, different experimental implementations have been proposed [64]. The traditional and most used approach is the heterodyne-detected 2DES (hereafter referred simply as "2DES"), already discussed in detail in Chapter 3. Just to recall the most important aspects, the final signal in 2DES is a coherent signal generated after the interaction of three laser pulses, which results proportional to the macroscopic polarization of the investigated system [51]. 2DES is based on a non-collinear geometry, thus relies on the wave-vector selection of the third-order signal according to the phase-matching conditions [46, 47]. Although this approach provides a background-free detection, the major drawback is a limited spatial resolution [145], which leads to a 2DES signal that represents an ensemble-averaged response over a large number of molecules [146].

To overcome these limitations, Action-2DES (A-2DES) has been recently proposed as an alternative approach for measuring coherent nonlinear spectra, without the need for coherent detection [147]. A-2DES is based on the detection of an incoherent signal generated after the interaction of four laser pulses. More in detail, the first pulse brings the system to a coherent superposition of states, which is converted to a population by the second pulse. The third pulse generates again a coherent superposition of states, which the fourth pulse turns into an excited fourth-order population [148]. Therefore, the final signal results to be directly proportional to an excited-state population. Different kinds of incoherent signals can be detected, depending upon the investigated system. For example, fluorescence was used to in-

vestigate the conformation of molecular dimer complexes [149], a mixture of photosynthetic bacteria [146], as well as coupled squaraine dimers with increasing spacer length [147]. Photocurrent detection has been used to study quantum dot photocells [150], photoinduced processes in quantum wells [151] or the ultrafast dynamics of organic solar cells [152]. Other detection methods are based on photoions [153] or photoelectrons [154]. Moreover, A-2DES can be combined with single-molecule and microscopy techniques to achieve a spatial resolution beyond the diffraction limit [145, 146, 154].

A-2DES signal can be described in the framework of the fourth-order perturbation theory. Recalling the density matrix formalism described in Section 3.1.1 for 2DES, the A-2DES is an incoherent signal, which originates from the diagonal elements ρ_{nn} of the density matrix. As described previously, this signal is proportional to the fourth-order excited state population, which can be calculated, in the interaction picture, as the expectation value of a projection operator $\hat{\Pi}_I$, in analogy with Equation 3.14:

$$A^{(4)}(t) = Tr\left[\hat{\Pi}_I \rho_I^{(4)}(t)\right] \tag{7.1}$$

where $\hat{\Pi}_I = \sum_n \Gamma_n |\phi_n\rangle\langle\phi_n|$ run onto all the excited states, each of them weighted by their respective quantum yield coefficient Γ_n, which values depend on the detection method [149, 155]. Thus, in analogy with Equation 3.19, the final signal can be expressed as:

$$\begin{aligned} A^{(4)}(t) = \int_0^\infty dt_4 \int_0^\infty dt_3 \int_0^\infty dt_2 \int_0^\infty dt_1 E(t-t_4)E(t-t_4-t_3) \\ E(t-t_4-t_3-t_2)E(t-t_4-t_3-t_2-t_1)Q^{(4)}(t_4,t_3,t_2,t_1) \end{aligned} \tag{7.2}$$

where we introduce the population-based response functions $Q^{(4)}(t_4, t_3, t_2, t_1)$ defined as:

$$\begin{aligned} Q^{(4)}(t_4,t_3,t_2,t_1) = \left(-\frac{i}{\hbar}\right)^4 \langle \hat{\Pi}_I(t_4+t_3+t_2+t_1) \\ \times [\mu_I(t_3+t_2+t_1),[\mu_I(t_2+t_1),[\mu_I(t_1),[\mu_I(0),\rho(0)]]]]\rangle \end{aligned} \tag{7.3}$$

By explicitly calculating the commutator, we obtain all the 2^4 possible Liouville pathways, including also the 8 terms of the third order response function previously calculated (and reported in Equation 3.22). In addition, in A-2DES the last interaction can act both on the left (ket) or on the right (bra) of the density matrix, leading to further contributions of opposite signs in the Liouville pathways. Ex-

perimentally, different contributions from the total signals can be discriminated by different phase combinations of the four exciting pulses. Indeed, the signal phase ϕ_{sig} can be written as:

$$\phi_{sig} = \alpha\phi_1 + \beta\phi_2 + \gamma\phi_3 + \delta\phi_4 \tag{7.4}$$

with $\alpha, \beta, \gamma, \delta$ representing the number and the kind of interaction of each of the four pulses with the density matrix. For example, a value of $\alpha = +1$ represents an absorption (emission) contribution if the first pulse acts on the right (left) of the density matrix. On the contrary, for a value of $\alpha = -1$ an interaction on the right (left) of the density matrix corresponds to an emission (absorption) contribution. Among all the different contributions, the most important for our interest are the rephasing and the non-rephasing signals, which are respectively given by the two following different phase combinations:

$$\begin{aligned} \phi_{sig}^{R} &= -1\phi_1 + 1\phi_2 + 1\phi_3 - 1\phi_4 \\ \phi_{sig}^{NR} &= +1\phi_1 - 1\phi_2 + 1\phi_3 - 1\phi_4 \end{aligned} \tag{7.5}$$

As already pointed out for 2DES (see Section 3.1.5), the different contributions to the signal, identified as GSB, SE and ESA pathways, can be more easily visualized in the form of Feynman diagrams. The same formalism can be applied to describe the final signal of A-2DES, taking into account the interaction with the additional fourth pulse [149]. The Feynman diagrams for the rephasing and non-rephasing pathways are reported in Figure 7.1.

After the last interaction, the system is left in an excited (or double-excited) population state [150]. The GSB and the SE pathways produce population in the first-excited state $|e\rangle\langle e|$ and contribute to the total signal with the same sign. Moreover, there are two different ESA pathways. The first ESA pathway (ESA_1) brings the final population to the first-excited state $|e\rangle\langle e|$. In the second ESA pathway (ESA_2), the final population resides in the doubly-excited state $|f\rangle\langle f|$. It is important to note that, while the ESA_1 pathway contributes with the same sign as the GSB and SE, the ESA_2 pathway contributes with an opposite sign [150].

The total signal is given by the sum of these four excitation pathways, according to GSB + SE + ESA_1 - ESA_2, where $ESA_2 = \Gamma \cdot ESA_1$, with $\Gamma \geq 0$ the quantum yield associated with the doubly-excited state with respect to the one associated with the first-excited state. Indeed, we must take into account that the quantum yields of the first and the double-excited states can be quite different, and the contributions of

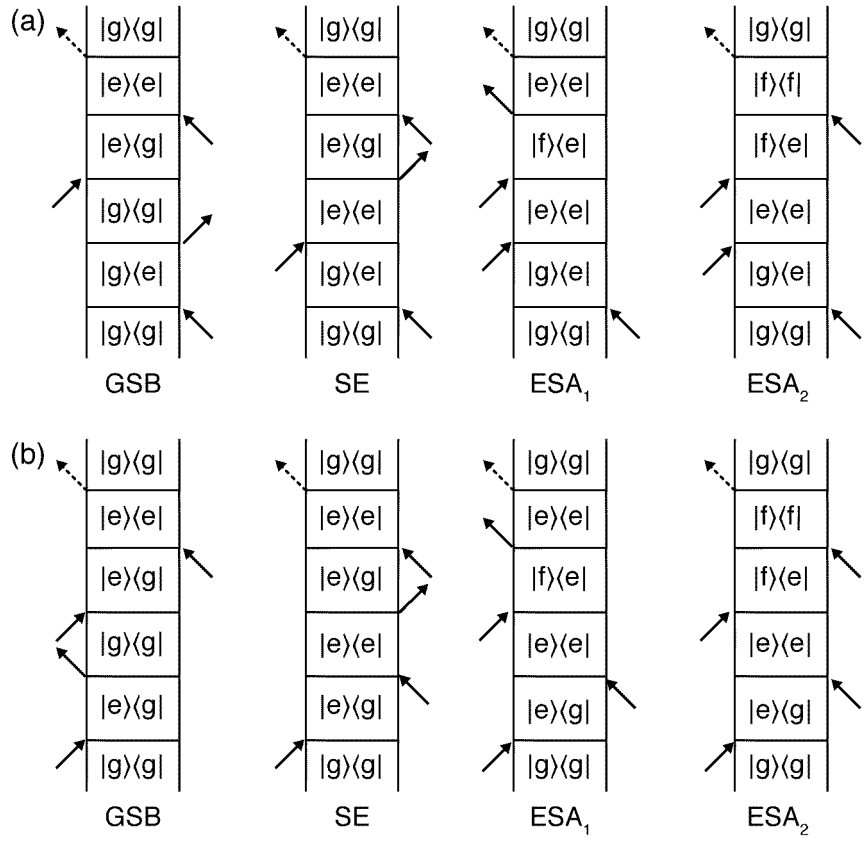

Figure 7.1: Feynman diagrams summarizing all the possible contributions detected by A-2DES experiment for (a) rephasing and (b) non-rephasing signals.

ESA_2 need to be properly weighted. Generally, the value of Γ depends on the type of incoherent signal. For example, in fluorescence detected A-2DES experiments the value of Γ is typically ≤ 1, indicating that the fluorescence quantum yield from higher energy excited states is small in comparison with the fluorescence yield from excited states at lower energy, especially in the presence of radiationless processes [156, 157]. For photocurrent-detected 2D experiments, the value of Γ may be much larger than the fluorescence case with a value ≥ 2, since the photocurrent quantum yield is enhanced for high-energy excited states in comparison to low-energy states [150].

A-2DES is a fully-collinear technique, meaning that all the interacting pulses travel the same optical path. The different contributions to the final signal cannot be separated spatially, as in the case of conventional 2DES. Other approaches are used to disentangle the detected signal into the components of interest, which are based on the principle that the signal phase is a combination of the phases of the excitation pulses [158]. This phase dependence can therefore be exploited to retrieve the fi-

nal signal by changing the phases of the four exciting pulses while repeating the measurement. Generally, two main approaches are used to control the phases of the pulses and are explained briefly in the following paragraphs:
(i) **phase cycling:** in this method, the phases of the four exciting pulses are independently rotated of a certain known amount [159, 160]. Usually, a pulse shaper generates a train of four laser pulses with a different phase combination. Different signals are recorded for any phase combination and then, summing them properly, a 2D spectrum of the process of interest can be extracted. The phase of the final signal can be written as a combination of the phases of the four pulses:

$$\phi_s = \alpha\phi_1 + \beta\phi_2 + \gamma\phi_3 + \delta\phi_4 \tag{7.6}$$

where the condition $\alpha + \beta + \gamma + \delta = 0$ needs to be fullfilled. Moreover, considering only four interactions with the exciting pulse sequence, we need to include an additional condition:

$$|\alpha| + |\beta| + |\gamma| + |\delta| \leq 4 \tag{7.7}$$

Since the system ends in a population state, only three out of the four indices $(\alpha, \beta, \gamma, \delta)$ are independent of each other, allowing to consider only relative phases $\phi_{21} \equiv \phi_2 - \phi_1$, $\phi_{31} \equiv \phi_3 - \phi_1$ and $\phi_{41} \equiv \phi_4 - \phi_1$, all referred to the phase of the first pulse. During an experiment, the phases can only be sampled in discrete steps. For example, considering the rephasing contribution with $(\alpha = -1, \beta = +1, \gamma = +1, \delta = -1)$, it has been demonstrated that it can be extracted with a $1 \times 3 \times 3 \times 3$ phase-cycling scheme, where each of the relative phases ϕ_{21}, ϕ_{31}, and ϕ_{41} is changed in three equidistant steps between 0 and 2π [159].
(ii) **phase modulation:** within this approach, the phase of each pulse is continuously modulated at specific modulation frequencies. This technique was first implemented by Marcus *et* coworkers [62]. In their experiment, a multi-branch interferometric setup was used to split each single laser pulses into a train of four pulses. Each interferometric branch contains an acousto-optic modulator that continuously modulates the phase of each pulse. In a more recent application, the use of a suitable pulse shaper allows to combine the pulse-by-pulse shaping while modulating the phases of the different pulses [152, 161, 162]. The phase ϕ_{i} of each pulse is varied so that:

$$\phi_i(f_i, t) = 2\pi m f_i T \tag{7.8}$$

where f_i are the modulation frequencies of the order of hundreds of Hz, m runs

through the number of waveform repetitions for a single experiment and T is the delay time between two consecutive trains of four pulses. Lastly, by Fourier transforming the recorded signal to the frequency domain, the different contributions to the signal appear at different linear combinations of the modulation frequencies and can be easily separated.

During the last few years, A-2DES has turned out to be a very promising technique for its numerous benefits. In particular, A-2DES detection schemes have a distinct advantage in terms of sensitivity compared to 2DES. This makes it possible to measure signals from small volumes and, in principle, also single molecules [163, 164]. Another advantage is that the signal is not an interference between electric fields, as in 2DES, but it is a real property of the system. This offers direct access to the physical quantity of interest and enables to operate at the real regime conditions of the devices. This opens up the possibility of studying the dynamics of *in vivo* proteins with a fluorescence-detection [165] or observing directly only the charges generated by specific processes in the case of photocurrent-detection [148]. Moreover, A-2DES measurements allow neglecting many "background" responses, such as coherent artefacts, solvent or scattering contributions, selecting only the dynamics of interest. However, while the interpretation of 2DES spectra is well established, the A-2DES is a fairly new technique and its interpretation is still an open debate in literature [158]. Since the measured signal is different, the well known tools developed for the interpretation of 2DES cannot be directly applied to A-2DES. In addition, the cross-peaks features in A-2DES spectra strictly depend on the quantum yield of the studied system and their evaluation is not trivial [158]. Experimentally, there are more stringent requirements for the choice of the sample, which should be optimized carefully depending on the detection scheme. For example, in the case of photocurrent, the samples must be conductive or deposited on a conductive substrate in order to measure a current signal. This means that not all samples can be easily measured without a preliminary careful design.

7.2. Setup and data analysis

7.2.1. Setup

The A-2DES setup built in our laboratory is based on photocurrent detection. A schematic representation of the A-2DES setup is reported in Figure 7.2. The laser source and the NOPA are the same used for coherent 2DES experiments. After

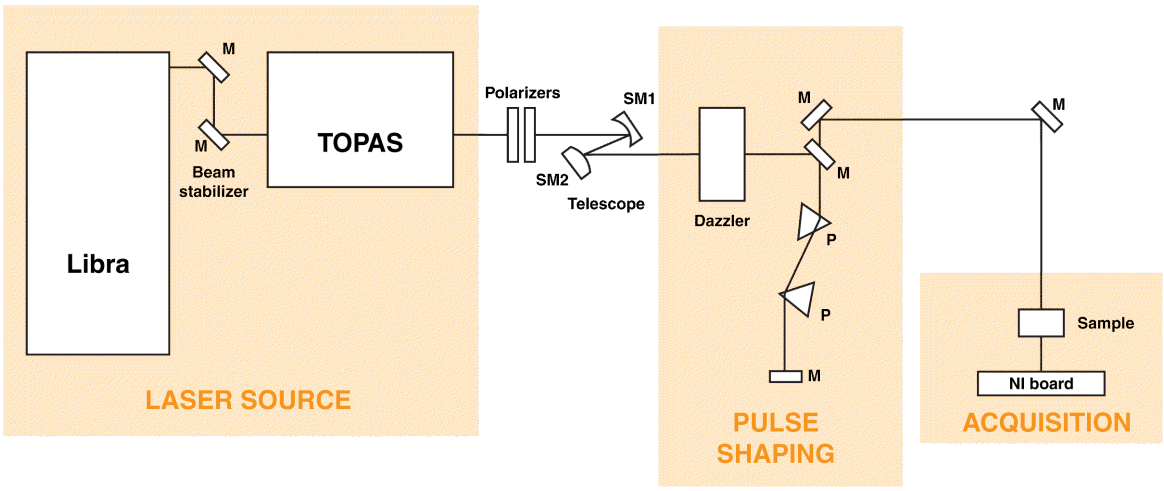

Figure 7.2: Schematic representation of the A-2DES setup. Abbreviations: (M) mirror, (SM) spherical mirror, (P) prism.

a prism compression stage, the laser pulse enters an acousto-optic pulse shaper (Fastlite Dazzler). In the case of A-2DES setup the Dazzler, previously exploited only to finely control the phase of the different frequency components, is also used to generate, from each incoming laser pulse, a sequence of four time-delayed exciting pulses. The values of the corresponding time delays (t_1, t_2, t_3) are scanned independently during an experiment to obtain the full time-dependent fourth-order signal. To achieve the phase modulation scheme, the phase of each exciting pulse is also modulated at a specific frequency f_i. A mirror is then used to direct the beam on the sample and the photocurrent is read-out through a National Instruments board (NI usb-4432).

7.2.2. Data acquisition and analysis

In our phase-modulation detection, the f_i can assume values that depend on the maximum storage memory of the Dazzler pulse shaper [152]. The Dazzler has 72 slots of memory, therefore we chose to perform a pattern of 72 waveforms for each set of fixed time delays (t_1, t_2, t_3). The f_i of the first exciting pulse is always kept fixed at zero (f_i=0), while the other three exciting pulses increase their phase of $\pi/6$, $\pi/8$, and $\pi/9$, respectively at each streamed waveform. In this way, the four pulses start all with phase equal to zero, and, during the last 72$^{\mathrm{nd}}$ pulse of the sequence, the phase of the three modulated pulses is a 2π multiple minus $\pi/6$, $\pi/8$, and $\pi/9$, respectively. The Dazzler keeps cycling these 72 waveforms until a good signal-to-noise ratio is reached. At the next laser pulse, corresponding to the first one of the

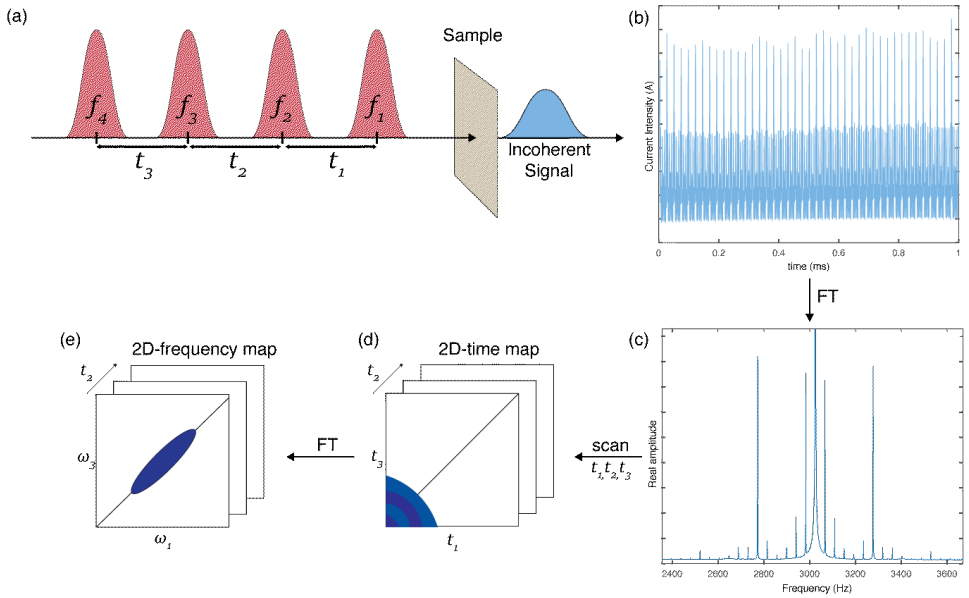

Figure 7.3: Pictorial scheme of the A-2DES data acquisition and analysis procedure. After the interaction of the sample with a train of four pulses (a), a modulated signal is acquired (b). The FFT spectrum of this signal gives a peak at a different frequency for each contribution to the fourth-order population. The A-2DES maps are rebuilt by extracting the components at all time-delays (d). After data processing and Fourier transform along t_1 and t_3, the 2D-frequency map is obtained (e).

next sequence, the values of (t_1, t_2, t_3) are changed and this pattern can start again. The final signal recorded by the acquisition board is a signal modulated in time through a combination of all the frequencies, as depicted in Figure 7.3(b). Subsequently, this acquired signal is Fourier transformed to obtain a spectrum for each tern of (t_1, t_2, t_3), as reported in Figure 7.3(c), which includes several signals at specific combinations of frequencies [166]. A particular modulation frequency is chosen (for example the one corresponding to the rephasing or the non-rephasing signals). By plotting the signal at this exact modulation frequency as a function of the scanned time delays, we get 2D-maps as a function of the delays between pulses (see Figure 7.3(c)). After Fourier transforming along t_1 and t_3 axes, we obtain a series of frequency-frequency maps (Figure 7.3(d)), similar to those obtained in a 2DES measurement.

7.3. Measurements

To test our setup, the choice of the sample was of crucial importance, since it needs to be conductive and to generate a current when photoexcited, in order to measure a photocurrent signal. For this reason, we performed a preliminary measurement

on a Graphene (Gr)-based device, in collaboration with the group of Prof. Luigi Sangaletti (UniCatt, Brescia). Gr represents a good benchmark since it shows a wide range of unique electronic and optical properties [167]. For example, pristine Gr, that is graphene in its original unoxidized form, shows great potential as an optically conductive window, due to its high optical transmittance (of almost 98%), which allows a large range of light wavelengths to pass through [168]. Thus, the direct measurement of a photocurrent turned out to be relatively simple respect to other samples. Moreover, Gr functionalization can enhance its properties, including opening its band gap [169] or tuning its conductivity [168, 170]. All these modulations generally improve the performances of Gr-based devices, which find applications in many different fields, like photocatalysis [171, 172], energy materials [173, 174], photonics [175] and so on. Furthermore, Gr-based devices can be functionalized with strong light-absorbing species such as chromophores or nanoparticles. In this way, they are able to convert light energy into electrical energy in photoelectrochemical cells or photodetectors [176]. The coupling between the Gr and the light-absorber molecules leads to efficient energy or charge transfer to or from the Gr-based devices after photoexcitation [177]. For all these reasons, a deeper comprehension of the optical properties of pristine Gr is fundamental for its exploitation. With A-2DES, we can push our understanding beyond the current knowledge, capturing the ultrafast dynamics right after Gr photoexcitation in real working devices.

7.3.1. Experimental methods and results

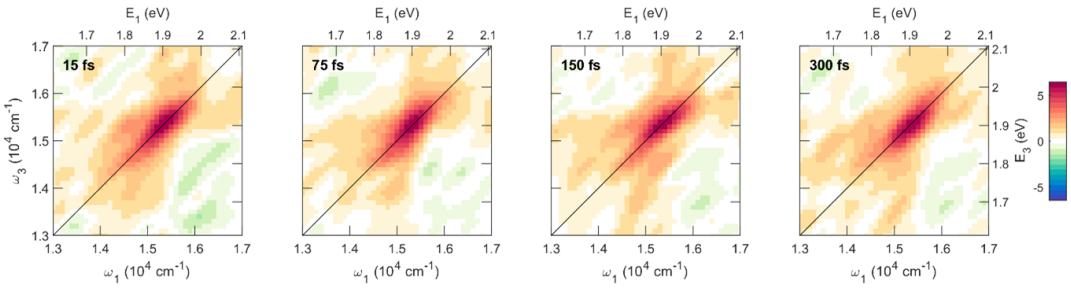

Figure 7.4: Rephasing A-2DES maps at selected values of population times for the Gr sample.

The measurements on pristine Gr have been performed with the A-2DES setup described in Section 7.2.1. The t_2 time delay was scanned from 0 to 300 fs, with steps of 7.5 fs. The pulse energy was 30 nJ at the sample position. The samples are placed on a circuit board, consisting of a load resistor (R_L) in series with the sample resistance (R_S), to which a constant voltage (V_C = 5 V) is applied. The spot size at the sample

position was about 1 mm.
Figure 7.4 shows the evolution of the A-2DES signal as a function of the population time for the pristine Gr sample. Qualitatively, the main feature is a diagonal peak centred at about 15500 cm^{-1} (1.9 eV), whose position remains almost constant at increasing population time. This should be expected considering that the pristine Gr can absorb in all the visible region. Indeed, the A-2DES response is a convolution of the sample absorption and of the laser spectrum [178]. So in this case, the highest contribution to the total signal comes from the laser band. These measurements are not particularly informative on the system, but ensure us the possibility of measuring a photocurrent from a Gr devices. As a future perspective, these findings pave the way to a future functionalization of the Gr with a metal-phtalocyanines to investigate the presence of charge transfer processes between the molecules and the Gr surface and to get more details about the underneath ultrafast transfer dynamics.

7.3.2. Artifacts problem

In A-2DES, the Dazzler is used to generate, from each incoming pulse, a train of four pulses and to modulate their respective time delays and relative phases. The Dazzler is an acousto-optic pulse shaper, meaning that the laser pulse can be seen as a waveform which is shaped by applying an acoustic power. This waveform can be normalized to a "constant-gain" reference waveform, which ensures that the acoustic power and, in turn, the optical power of the shaped laser pulse stays constant during an experiment. At small acoustic-power operating regime, this constant regime is verified. However, at high acoustic-power, the Dazzler has limited capabilities in keeping it costant while changing the phases of the pulse. This give rise to nonlinearities artifacts, which are not dependent on the response of the sample but on the fluctuant power of excitation. This effect is mainly present in the rephasing signal and it is manifested as a large amplitude contribution along the diagonal that hides the real signatures of the systems, as shown in Figure 7.5. Proofs of this artifacts were previously reported in the works of the Brixner group [155]. In their experiments, they correct this nonlinearities with an *a priori* approach, by iteratively searching and dividing the measured signal by a correction factor for each pulse sequence, until the diagonal artifact is removed and does not contribute anymore to the final signal.
In our group, we adopted an alternative *a posteriori* approach. We measure the output of the Dazzler simultaneously with the measurements by placing a photodiode

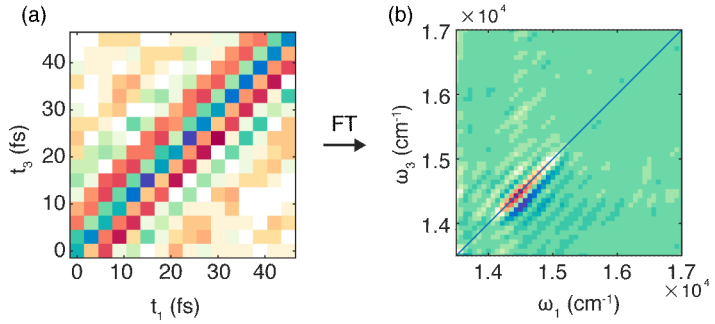

Figure 7.5: (a) Time-dependent A-2DES map showing the diagonal artifacts arising from Dazzler nonlinearities, which leads to (b) a spurious peak in the 2D-frequency map obtained after Fourier transforming along t_1 and t_3.

on a back reflection. We then use this response to renormalize the signal. While this easy methodology allows a first correction of the main contributions to the artifact, still more refined procedures must be developed to increase the reliability of the final data.

8 | Conclusions and future developments

The present research aimed to characterize the excited state dynamics of biological and bioinspired systems. In particular, this dissertation seeks to contribute to this growing area of research by exploring the details of processes happening immediately after the photoexcitation of different systems. Considering the timescale of these phenomena, Two-dimensional Electronic Spectroscopy (2DES) fits into this context as a leading technique in the study of ultrafast dynamics up to the femtosecond regime. Thanks to a global fitting analysis methodology previously developed in our group, we could obtain the time constants regulating the kinetics of the relaxation processes and get more insights into the related mechanisms.

As a first step, we investigated the ultrafast dynamics of Chl *b* molecules in solution both at RT and 77K. The objective of this study was to determine whether different dynamic mechanisms were activated in these two different thermal regimes. For the measurements at RT, we found that the dynamics at early times was dominated by the spectral diffusion processes associated with the fluctuations of the environment surrounding the molecules, to which we attributed a time constant of 150 fs. This time was consistent with the typical timescales of solvation dynamics of other common dyes reported in literature. Interestingly, we could not observe any trace of internal conversion between Q_x and Q_y bands, confirming previous studies suggesting a lower degree of Q_x- Q_y mixing in Chl *b* compared to Chl *a*. At 77 K, no sign of spectral diffusion was detected since the inertial motion of solvent molecules is hindered by the low temperature. The primary mechanism dominating the excited states relaxation was instead an ultrafast (60 fs) redistribution of energy into vibrational modes by internal conversion. Thanks to the capability of the 2DES, we could not only provide a time constant for this process but also verify the importance of a selected subset of vibrational modes assisting the internal conversion process. These findings shed new light on the photophysical properties of Chl *b*, which might po-

tentially lead also to a better understanding of the role of Chl *b* in light-harvesting complexes and of the different behaviour with respect to the more common Chl *a*.

As a step further on building this knowledge, we decided to compare the ultrafast behavior of Chl *a* and Chl *b* when embedded in multichromophoric protein complexes. To this aim, we considered four Water-Soluble Chlorophyll-binding Proteins (WSCPs), characterized two-by-two by the same protein scaffold but binding different pigments, Chl *a* or Chl *b*. The four complexes share a very similar structure, with the only relevant difference being the possibility for Chl *b*-binding WSCPs of establishing an additional H-bond through the formyl group of the Chl *b* with the protein scaffold. Our final goal was to understand if it was possible to correlate the optical and dynamic response of the four complexes to the presence of specific pigment-protein interactions. Actually, 2DES measures revealed small but significant differences in the ultrafast dynamics of the four complexes. More specifically, we found that the electronic coupling between pigments can be correctly predicted based on geometrical considerations only for Chl *a*-WSCP, whereas strong deviations from the calculations are found for Chl *b*-WSCP, where the geometrical prediction highly underestimates the coupling. The stronger coupling in Chl *b*-WSCP explains the differences in the recorded dynamics, like the appearance of an additional ultrafast decay constant, attributed to the almost instantaneous decay of the superpositions of excitonic states generated after excitation. The different behaviour manifested by Chl *a* and Chl *b* in the same protein complex and the discrepancies between calculated and experimental energy gaps in Chl *b*-WSCP could be justified by accounting for the only structural difference between the two complexes, i.e., the presence of the formyl group in Chl *b* at the C7 position and the possibility of engaging this group in the formation of an additional H-bond with the protein backbone. Therefore, we demonstrated that the formation of an H-bond could have very strong consequences on the electronic structure and on the ultrafast dynamics of pigment-protein complexes. This finding implies the possibility of tuning the photophysics and the transport properties of artificial systems by properly engineering H-bonds within their structure. In this context, our observations allow a step forward towards more conscious exploitation of these important interactions.

Bearing in mind the importance of H-bond interactions, we took an additional step to understand how their presence can influence the dynamics in the excited state. With this aim, we characterized through pump-probe and 2DES measurements an H-bonded dimer of BODIPY chromophores, properly designed such that three H-

bonds are established between the two chromophores moieties. The same measurements were also performed on both the monomeric units to assess the presence of dynamics relevant only in the dimer. Our measurements revealed that the formation of a dimer opens up a new ultrafast relaxation channel, characterized by a time constant of about 200 fs. Further investigations pointed out that two kinds of processes contribute to these dynamics. First, we detected an "intra-molecular" relaxation pathway, which involves the two chromophoric moieties separately but simultaneously. Second, an "intermolecular" relaxation mechanism involves the transfer of population among the two BODIPY units forming the dimer. The analysis of the beating behaviour of the 2DES signals revealed the presence of peculiar features only in the dimer, developing in a timescale of about 150 fs and attributable to vibrational motions of the groups involved in the H-bond. In light of these pieces of evidence and compared with the previous literature on excited-state H-bond dynamics, it could conceivably be hypothesised that the H-bonds activate new ultrafast dynamic channels in the relaxation dynamics of the dimer involving simultaneous intra- and inter-molecular mechanisms. These findings confirmed our intuition that the design of H-bonded structures can effectively be exploited to drive the ultrafast dynamics in complex materials.

As a final step, we implemented in our laboratory a novel A-2DES technique based on photocurrent detection. The advantage of this detection is the possibility of directly measuring a real properties of the systems, providing an unprecedented level of insight into the excited state dynamics of conductive devices in operating conditions. The first experimental results on a prototypical Graphene-based device were encouraging, ensuring us the possibility of measuring a photocurrent. Certainly, this setup is fairly new, so it will require further improvements and more sophisticated signal acquisition and analysis, especially for the correction of artifacts deriving by the Dazzler's intrinsic behaviour.

The shreds of evidence presented in this thesis depict the pathway that we followed to move from biological complexes to biomimetic artificial energy harvesting devices. Inspired by what we learned about the photophysics of biologically relevant pigments and biological complexes, we moved to the design and characterization of artificial systems. On the one side, we understood that a deeper knowledge of the role of the environment is crucial to understand the underlying mechanisms and functions of natural processes and exploit them for the design and the improvements of new bioinspired molecules. Along this line, we thus proposed the design of

H-bonds motifs as a strategy to modulate and drive the ultrafast dynamics of energy transport. On the other side, it is clear that the design of new artificial biomimetic systems needs to be complemented by the development of new spectroscopic tools able to reveal with increasing clarity the dynamic behavior and the connection between the photophysical properties of the materials and the functionalities of the final devices built with these materials. The 2DES and its recent novel implementations, the A-2DES, turned out to be cutting-edge techniques in this constantly developing field, allowing the detection of ultrafast processes with unprecedented clarity.

Bibliography

[1] J. Hwang, Y. Jeong, J. M. Park, K. H. Lee, J. W. Hong, and J. Choi, "Biomimetics: forecasting the future of science, engineering, and medicine," *International journal of nanomedicine*, vol. 10, p. 5701, 2015.

[2] U. G. Wegst, H. Bai, E. Saiz, A. P. Tomsia, and R. O. Ritchie, "Bioinspired structural materials," *Nature materials*, vol. 14, no. 1, pp. 23–36, 2015.

[3] G. D. Scholes, "Quantum-coherent electronic energy transfer: Did nature think of it first?," *The Journal of Physical Chemistry Letters*, vol. 1, no. 1, pp. 2–8, 2010.

[4] V. Balzani, A. Credi, and M. Venturi, "Photochemical conversion of solar energy," *ChemSusChem: Chemistry & Sustainability Energy & Materials*, vol. 1, no. 1-2, pp. 26–58, 2008.

[5] A. Sarkar, T. Behera, R. Sasmal, R. Capelli, C. Empereur-Mot, J. Mahato, S. S. Agasti, G. M. Pavan, A. Chowdhury, and S. J. George, "Cooperative supramolecular block copolymerization for the synthesis of functional axial organic heterostructures," *Journal of the American Chemical Society*, vol. 142, no. 26, pp. 11528–11539, 2020.

[6] H.-J. Kim, P. C. Nandajan, J. Gierschner, and S. Y. Park, "Light-harvesting fluorescent supramolecular block copolymers based on cyanostilbene derivatives and cucurbit[8]urils in aqueous solution," *Advanced Functional Materials*, vol. 28, no. 4, p. 1705141, 2018.

[7] Q. Song, S. Goia, J. Yang, S. C. Hall, M. Staniforth, V. G. Stavros, and S. Perrier, "Efficient artificial light-harvesting system based on supramolecular peptide nanotubes in water," *Journal of the American Chemical Society*, vol. 143, no. 1, pp. 382–389, 2020.

[8] R. Zagami, M. A. Castriciano, A. Romeo, M. Trapani, R. Pedicini, and L. M.

Scolaro, "Tuning supramolecular chirality in nano and mesoscopic porphyrin j-aggregates," *Dyes and Pigments*, vol. 142, pp. 255–261, 2017.

[9] A. Arrigo, F. Puntoriero, G. La Ganga, S. Campagna, M. Burian, S. Bernstorff, and H. Amenitsch, "Aggregation-induced energy transfer in a decanuclear Os(II)/Ru(II) polypyridine light-harvesting antenna dendrimer," *Chem*, vol. 3, no. 3, pp. 494–508, 2017.

[10] U. Hahn, M. Gorka, F. Vögtle, V. Vicinelli, P. Ceroni, M. Maestri, and V. Balzani, "Light-harvesting dendrimers: Efficient intra-and intermolecular energy-transfer processes in a species containing 65 chromophoric groups of four different types," *Angewandte Chemie*, vol. 114, no. 19, pp. 3747–3750, 2002.

[11] R. Kathpalia and A. K. Verma, "Bio-inspired nanoparticles for artificial photosynthesis," *Materials Today: Proceedings*, vol. 45, pp. 3825–3832, 2021.

[12] H. Imahori, Y. Mori, and Y. Matano, "Nanostructured artificial photosynthesis," *Journal of Photochemistry and Photobiology C: Photochemistry Reviews*, vol. 4, no. 1, pp. 51–83, 2003.

[13] P. K. Dutta, R. Varghese, J. Nangreave, S. Lin, H. Yan, and Y. Liu, "Dna-directed artificial light-harvesting antenna," *Journal of the American Chemical Society*, vol. 133, no. 31, pp. 11985–11993, 2011.

[14] P. K. Dutta, S. Levenberg, A. Loskutov, D. Jun, R. Saer, J. T. Beatty, S. Lin, Y. Liu, N. W. Woodbury, and H. Yan, "A DNA-directed light-harvesting/reaction center system," *Journal of the American Chemical Society*, vol. 136, no. 47, pp. 16618–16625, 2014.

[15] G. D. Scholes, G. R. Fleming, A. Olaya-Castro, and R. Van Grondelle, "Lessons from nature about solar light harvesting," *Nature chemistry*, vol. 3, no. 10, pp. 763–774, 2011.

[16] G. Fowler, R. Visschers, G. Grief, R. Van Grondelle, and C. Hunter, "Genetically modified photosynthetic antenna complexes with blueshifted absorbance bands," *Nature*, vol. 355, no. 6363, pp. 848–850, 1992.

[17] T. P. Krüger, E. Wientjes, R. Croce, and R. van Grondelle, "Conformational switching explains the intrinsic multifunctionality of plant light-harvesting complexes," *Proceedings of the National Academy of Sciences*, vol. 108, no. 33, pp. 13516–13521, 2011.

[18] E. Wientjes, G. Roest, and R. Croce, "From red to blue to far-red in Lhca4: how does the protein modulate the spectral properties of the pigments?," *Biochimica et Biophysica Acta (BBA)-Bioenergetics*, vol. 1817, no. 5, pp. 711–717, 2012.

[19] H. Witt, E. Schlodder, C. Teutloff, J. Niklas, E. Bordignon, D. Carbonera, S. Kohler, A. Labahn, and W. Lubitz, "Hydrogen bonding to P700: site-directed mutagenesis of threonine A739 of photosystem I in Chlamydomonas reinhardtii," *Biochemistry*, vol. 41, no. 27, pp. 8557–8569, 2002.

[20] C. Curutchet, J. Kongsted, A. Munoz-Losa, H. Hossein-Nejad, G. D. Scholes, and B. Mennucci, "Photosynthetic light-harvesting is tuned by the heterogeneous polarizable environment of the protein," *Journal of the American Chemical Society*, vol. 133, no. 9, pp. 3078–3084, 2011.

[21] F. Levi, S. Mostarda, F. Rao, and F. Mintert, "Quantum mechanics of excitation transport in photosynthetic complexes: a key issues review," *Reports on Progress in Physics*, vol. 78, no. 8, p. 082001, 2015.

[22] H. Haken and P. Reineker, "The coupled coherent and incoherent motion of excitons and its influence on the line shape of optical absorption," *Zeitschrift für Physik*, vol. 249, no. 3, pp. 253–268, 1972.

[23] E. Collini, "Spectroscopic signatures of quantum-coherent energy transfer," *Chemical Society Reviews*, vol. 42, no. 12, pp. 4932–4947, 2013.

[24] A. Olaya-Castro and G. D. Scholes, "Energy transfer from Förster–Dexter theory to quantum coherent light-harvesting," *International Reviews in Physical Chemistry*, vol. 30, no. 1, pp. 49–77, 2011.

[25] B. Mennucci and S. Corni, "Multiscale modelling of photoinduced processes in composite systems," *Nature Reviews Chemistry*, vol. 3, no. 5, pp. 315–330, 2019.

[26] L. Cupellini, M. Bondanza, M. Nottoli, and B. Mennucci, "Successes & challenges in the atomistic modeling of light-harvesting and its photoregulation," *Biochimica et Biophysica Acta (BBA)-Bioenergetics*, vol. 1861, no. 4, p. 148049, 2020.

[27] K. Vrandecic, M. Ratsep, L. Wilk, L. Rusevich, M. Golub, M. Reppert, K.-D. Irrgang, W. Kuhlbrandt, and J. Pieper, "Protein dynamics tunes excited state

positions in light-harvesting complex ii," *The Journal of Physical Chemistry B*, vol. 119, no. 10, pp. 3920–3930, 2015.

[28] J. Gao, D. A. Bosco, E. T. Powers, and J. W. Kelly, "Localized thermodynamic coupling between hydrogen bonding and microenvironment polarity substantially stabilizes proteins," *Nature structural & molecular biology*, vol. 16, no. 7, pp. 684–690, 2009.

[29] A. Agostini, E. Meneghin, L. Gewehr, D. Pedron, D. M. Palm, D. Carbonera, H. Paulsen, E. Jaenicke, and E. Collini, "How water-mediated hydrogen bonds affect chlorophyll a/b selectivity in water-soluble chlorophyll protein," *Scientific reports*, vol. 9, no. 1, pp. 1–10, 2019.

[30] R. Horn and H. Paulsen, "Early steps in the assembly of light-harvesting chlorophyll a/b complex: time-resolved fluorescence measurements," *Journal of Biological Chemistry*, vol. 279, no. 43, pp. 44400–44406, 2004.

[31] M. J. Llansola-Portoles, F. Li, P. Xu, S. Streckaite, C. Ilioaia, C. Yang, A. Gall, A. A. Pascal, R. Croce, and B. Robert, "Tuning antenna function through hydrogen bonds to chlorophyll a," *Biochimica et Biophysica Acta (BBA)-Bioenergetics*, vol. 1861, no. 4, p. 148078, 2020.

[32] R. E. Hubbard and M. K. Haider, "Hydrogen bonds in proteins: role and strength," *eLS*, 2010.

[33] E. Nibbering, F. Tschirschwitz, C. Chudoba, and T. Elsaesser, "Femtochemistry of hydrogen bonded complexes after electronic excitation in the liquid phase: the case of coumarin 102," *The Journal of Physical Chemistry A*, vol. 104, no. 18, pp. 4236–4246, 2000.

[34] M. Banno, K. Ohta, S. Yamaguchi, S. Hirai, and K. Tominaga, "Vibrational dynamics of hydrogen-bonded complexes in solutions studied with ultrafast infrared pump-probe spectroscopy," *Accounts of Chemical Research*, vol. 42, pp. 1259–1269, sep 2009.

[35] G.-J. Zhao and K.-L. Han, "Hydrogen bonding in the electronic excited state," *Accounts of chemical research*, vol. 45, no. 3, pp. 404–413, 2012.

[36] P. Song and F.-C. Ma, "Intermolecular hydrogen-bonding effects on photophysics and photochemistry," *International Reviews in Physical Chemistry*, vol. 32, no. 4, pp. 589–609, 2013.

[37] R. Orłowski, J. A. Clark, J. B. Derr, E. M. Espinoza, M. F. Mayther, O. Staszewska-Krajewska, J. R. Winkler, H. Jędrzejewska, A. Szumna, H. B. Gray, *et al.*, "Role of intramolecular hydrogen bonds in promoting electron flow through amino acid and oligopeptide conjugates," *Proceedings of the National Academy of Sciences*, vol. 118, no. 11, p. e2026462118, 2021.

[38] A. L. Sobolewski and W. Domcke, "Photophysics of intramolecularly hydrogen-bonded aromatic systems: ab initio exploration of the excited-state deactivation mechanisms of salicylic acid," *Physical Chemistry Chemical Physics*, vol. 8, no. 29, pp. 3410–3417, 2006.

[39] D. Shemesh and W. Domcke, "Effect of the chirality of residues and γ-turns on the electronic excitation spectra, excited-state reaction paths and conical intersections of capped phenylalanine–alanine dipeptides," *ChemPhysChem*, vol. 12, no. 10, pp. 1833–1840, 2011.

[40] G.-J. Zhao and K.-L. Han, "Role of intramolecular and intermolecular hydrogen bonding in both singlet and triplet excited states of aminofluorenones on internal conversion, intersystem crossing, and twisted intramolecular charge transfer," *The Journal of Physical Chemistry A*, vol. 113, no. 52, pp. 14329–14335, 2009.

[41] D. Wang, C. Hao, S. Wang, H. Dong, and J. Qiu, "A theoretical forecast of the hydrogen bond changes in the electronic excited state for BN and its derivatives," *Central European Journal of Physics*, vol. 10, no. 1, pp. 116–123, 2012.

[42] S. R. Flom and P. F. Barbara, "Proton transfer and hydrogen bonding in the internal conversion of S1 anthraquinones," *The Journal of Physical Chemistry*, vol. 89, no. 21, pp. 4489–4494, 1985.

[43] J. L. Sessler, B. Wang, and A. Harriman, "Photoinduced energy transfer in associated, but noncovalently-linked photosynthetic model systems," *Journal of the American Chemical Society*, vol. 117, no. 2, pp. 704–714, 1995.

[44] A. Swain, B. Cho, R. Gautam, C. J. Curtis, E. Tomat, and V. Huxter, "Ultrafast Dynamics of Tripyrrindiones in Solution Mediated by Hydrogen-Bonding Interactions," *Journal of Physical Chemistry B*, vol. 123, pp. 5524–5535, 2019.

[45] E. Pines, D. Pines, Y.-Z. Ma, and G. R. Fleming, "Femtosecond pump-probe measurements of solvation by hydrogen-bonding interactions," *ChemPhysChem*, vol. 5, no. 9, pp. 1315–1327, 2004.

[46] A. Gelzinis, R. Augulis, V. Butkus, and L. Valkunas, "Two-dimensional spectroscopy for non-specialists," *BBA - Bioenergetics*, pp. 271–285, 2018.

[47] A. M. Branczyk, D. B. Turner, and G. D. Scholes, "Two-dimensional electronic spectroscopy for the quantum-optics enthusiast," *Annalen der Physik*, pp. 1–20, 2013.

[48] E. Collini, "2d electronic spectroscopic techniques for quantum technology applications," *The Journal of Physical Chemistry C*, vol. 125, no. 24, pp. 13096–13108, 2021.

[49] W. W. Parson, *Modern optical spectroscopy*, vol. 2. Springer, 2007.

[50] J. R. Lakowicz, *Principles of fluorescence spectroscopy*. Springer, 2006.

[51] S. Mukamel, *Principles of nonlinear optical spectroscopy*. Oxford series in optical and imaging sciences, Oxford University Press, 1995.

[52] M. Cho, *Two-Dimensional Optical Spectroscopy*. CRC Press, 2009.

[53] R. Kubo, *Adv. Chem. Phys.* Shuler K., Ed.; Wiley Interscience: New York, 1969., Vol. 15, pp 101–127.

[54] M. Blume, "Stochastic theory of line shape: generalization of the kubo-anderson model," *Physical Review*, vol. 174, no. 2, p. 351, 1968.

[55] V. Butkus, D. Zigmantas, L. Valkunas, and D. Abramavicius, "Vibrational vs. electronic coherences in 2D spectrum of molecular systems," *Chemical Physics Letters*, vol. 545, pp. 40–43, 2012.

[56] J. Réhault, M. Maiuri, A. Oriana, and G. Cerullo, "Two-dimensional electronic spectroscopy with birefringent wedges," *Review of Scientific Instruments*, vol. 85, no. 12, p. 123107, 2014.

[57] I. A. Heisler, R. Moca, F. V. Camargo, and S. R. Meech, "Two-dimensional electronic spectroscopy based on conventional optics and fast dual chopper data acquisition," *Review of Scientific Instruments*, vol. 85, no. 6, 2014.

[58] A. Nemeth, J. Sperling, J. Hauer, H. F. Kauffmann, and F. Milota, "Compact phase-stable design for single- and electronic spectroscopy," *Optics letters*, vol. 34, no. 21, pp. 3301–3303, 2009.

[59] L. Bolzonello, A. Volpato, E. Meneghin, and E. Collini, "Versatile setup for

high-quality rephasing , non-rephasing , and double quantum 2D electronic spectroscopy," *J. Opt. Soc. Am. B*, vol. 34, no. 6, pp. 1223–1233, 2017.

[60] K. W. DeLong, R. Trebino, and D. J. Kane, "Comparison of ultrashort-pulse frequency-resolved-optical-gating traces for three common beam geometries," *Journal of the Optical Society of America B*, vol. 11, no. 9, p. 1595, 1994.

[61] N. Christensson, Y. Avlasevich, A. Yartsev, K. Müllen, T. Pascher, and T. Pullerits, "Weakly chirped pulses in frequency resolved coherent spectroscopy," *The Journal of chemical physics*, vol. 132, no. 17, p. 174508, 2010.

[62] P. F. Tekavec, G. A. Lott, and A. H. Marcus, "Fluorescence-detected two-dimensional electronic coherence spectroscopy by acousto-optic phase modulation," *Journal of Chemical Physics*, vol. 127, no. 21, 2007.

[63] D. J. Kane and R. Trebino, "Characterization of Arbitrary Femtosecond Pulses Using Frequency-Resolved Optical Gating," *IEEE Journal of Quantum Electronics*, vol. 29, no. 2, pp. 571–579, 1993.

[64] F. D. Fuller and J. P. Ogilvie, "Experimental Implementations of Two-Dimensional Fourier Transform Electronic Spectroscopy," *Annual Review of Physical Chemistry*, vol. 66, no. 1, pp. 667–690, 2015.

[65] R. Augulis and D. Zigmantas, "Two-dimensional electronic spectroscopy with double modulation lock-in detection: enhancement of sensitivity and noise resistance," *Optics Express*, vol. 19, no. 14, p. 13126, 2011.

[66] S. H. Shim and M. T. Zanni, "How to turn your pump-probe instrument into a multidimensional spectrometer: 2D IR and Vis spectroscopies via pulse shaping," *Physical Chemistry Chemical Physics*, vol. 11, no. 5, pp. 748–761, 2009.

[67] A. Volpato, L. Bolzonello, E. Meneghin, and E. Collini, "Global analysis of coherence and population dynamics in 2D electronic spectroscopy," *Optics Express*, vol. 24, no. 21, pp. 24773–24785, 2016.

[68] A. Volpato and E. Collini, "Time-frequency methods for coherent spectroscopy," *Optics Express*, vol. 23, no. 15, p. 20040, 2015.

[69] A. Volpato and E. Collini, "Optimization and selection of time-frequency transforms for wave-packet analysis in ultrafast spectroscopy," *Optics Express*, vol. 27, no. 3, pp. 2975–2987, 2019.

[70] B. Grimm, R. Porra, W. Rüdiger, and H. Scheer. Springer Dordrecht.

[71] J. K. Hoober, L. L. Eggink, and M. Chen, "Chlorophylls, ligands and assembly of light-harvesting complexes in chloroplasts," *Photosynthesis Research*, vol. 94, no. 2-3, pp. 387–400, 2007.

[72] R. Tanaka and A. Tanaka, "Chlorophyll cycle regulates the construction and destruction of the light-harvesting complexes," *BBA - Bioenergetics*, vol. 1807, no. 8, pp. 968–976, 2011.

[73] H. van Amerogen, L. Valkunas, and R. van Grondelle, *Photosynthetic excitons*. Singapore: World Scientific, 2000.

[74] R. Croce, R. van Grondelle, H. van Amerongen, and I. H. M. V. Stokkum, eds., *Light Harvesting in Photosynthesis*. Boca Raton: CRC Press, 2018.

[75] J. A. Oksanen, P. Martinsson, E. Åkesson, P. H. Hynninen, and V. Sundström, "Transient hole burning and solvation dynamics of chlorophyll b monomers in various solvent environments," *Journal of Physical Chemistry A*, vol. 102, no. 23, pp. 4328–4336, 1998.

[76] W. P. Bricker, P. M. Shenai, A. Ghosh, Z. Liu, M. G. M. Enriquez, P. H. Lambrev, H.-S. Tan, C. S. Lo, S. Tretiak, S. Fernandez-Alberti, and Y. Zhao, "Non-radiative relaxation of photoexcited chlorophylls: theoretical and experimental study," *Scientific Reports*, vol. 5, no. 1, p. 13625, 2015.

[77] M. F. Khyasudeen, P. J. Nowakowski, H. L. Nguyen, J. H. Sim, T. N. Do, and H. S. Tan, "Studying the spectral diffusion dynamics of chlorophyll a and chlorophyll b using two-dimensional electronic spectroscopy," *Chemical Physics*, vol. 527, no. August, p. 110480, 2019.

[78] N. H. C. Lewis and G. R. Fleming, "Two-dimensional electronic-vibrational spectroscopy of chlorophyll a and b," *The Journal of Physical Chemistry Letters*, vol. 7, pp. 831–837, mar 2016.

[79] M. Gouterman, "Spectra of porphyrins," *Journal of Molecular Spectroscopy*, vol. 6, pp. 138–163, 1961.

[80] M. Gouterman, G. H. Wagnière, and L. C. Snyder, "Spectra of porphyrins. Part II. Four orbital model," *Journal of Molecular Spectroscopy*, vol. 11, pp. 108–127, 1963.

[81] L. Hedayatifar, E. Irani, M. Mazarei, S. Rasti, Y. T. Azar, A. T. Rezakhani,

A. Mashaghi, F. Shayeganfar, M. Anvari, T. Heydari, A. R. Tabar, N. Nafari, M. A. Vesaghi, R. Asgari, and M. R. Rahimi Tabar, "Optical absorption and electronic spectra of chlorophylls a and b," *RSC Advances*, vol. 6, no. 111, pp. 109778–109785, 2016.

[82] J. R. Reimers, Z.-L. Cai, R. Kobayashi, M. Rätsep, A. Freiberg, and E. Krausz, "Assignment of the Q-bands of the chlorophylls: Coherence loss via Qx - Qy mixing," *Scientific Reports*, vol. 3, no. 1, p. 2761, 2013.

[83] M. Rätsep, J. Linnanto, and A. Freiberg, "Mirror symmetry and vibrational structure in optical spectra of chlorophyll a," *Journal of Chemical Physics*, vol. 130, no. 19, pp. 1–11, 2009.

[84] E. Fresch and E. Collini, "Relaxation dynamics of chlorophyll b in the sub-ps ultrafast timescale measured by 2d electronic spectroscopy," *International journal of molecular sciences*, vol. 21, no. 8, p. 2836, 2020.

[85] R. Moca, S. R. Meech, and I. A. Heisler, "Two-dimensional electronic spectroscopy of chlorophyll a: Solvent dependent spectral evolution," *The Journal of Physical Chemistry B*, vol. 119, no. 27, pp. 8623–8630, 2015.

[86] E. Meneghin, D. Pedron, and E. Collini, "Raman and 2D electronic spectroscopies : A fruitful alliance for the investigation of ground and excited state vibrations in chlorophyll a," *Chemical Physics*, 2018.

[87] E. Meneghin, D. Pedron, and E. Collini, "Spectroscopy data for the time and frequency characterization of vibrational coherences in bacteriochlorophyll a," *Data in Brief*, vol. 23, p. 103707, apr 2019.

[88] L. Bolzonello, F. Fassioli, and E. Collini, "Correlated fluctuations and intraband dynamics of j-aggregates revealed by combination of 2DES schemes," *The Journal of Physical Chemistry Letters*, vol. 7, pp. 4996–5001, dec 2016.

[89] E. Meneghin, C. Leonardo, A. Volpato, L. Bolzonello, and E. Collini, "Mechanistic insight into internal conversion process within Q-bands of chlorophyll a," *Scientific Reports*, vol. 7, no. 1, p. 11389, 2017.

[90] E. Meneghin, D. Pedron, and E. Collini, "Characterization of the coherent dynamics of bacteriochlorophyll a in solution," *Chemical Physics*, vol. 519, pp. 85–91, 2019.

[91] S. A. Passino, Y. Nagasawa, T. Joo, and G. R. Fleming, "Three-pulse echo peak

shift studies of polar solvation dynamics," *The Journal of Physical Chemistry A*, vol. 101, pp. 725–731, jan 1997.

[92] M. L. Horng, J. A. Gardecki, A. Papazyan, and M. Maroncelli, "Subpicosecond measurements of polar solvation dynamics: Coumarin 153 revisited," *The Journal of Physical Chemistry*, vol. 99, pp. 17311–17337, nov 1995.

[93] M. Berg, C. A. Walsh, L. R. Narasimhan, K. A. Littau, and M. D. Fayer, "Dynamics in low temperature glasses: Theory and experiments on optical dephasing, spectral diffusion, and hydrogen tunneling," *The Journal of Chemical Physics*, vol. 88, no. 3, pp. 1564–1587, 1988.

[94] F. Šanda, V. Perlík, C. N. Lincoln, and J. Hauer, "Center line slope analysis in two-dimensional electronic spectroscopy," *The Journal of Physical Chemistry A*, vol. 119, no. 44, pp. 10893–10909, 2015.

[95] L. Bolzonello, A. Polo, A. Volpato, E. Meneghin, M. Cordaro, M. Trapani, M. Fortino, A. Pedone, M. A. Castriciano, and E. Collini, "Two-dimensional electronic spectroscopy reveals dynamics and mechanisms of solvent-driven inertial relaxation in polar bodipy dyes," *The Journal of Physical Chemistry Letters*, vol. 9, no. 5, pp. 1079–1085, 2018.

[96] M. Jakučionis, V. Chorošajev, and D. Abramavičius, "Vibrational damping effects on electronic energy relaxation in molecular aggregates," *Chemical Physics*, vol. 515, no. March, pp. 193–202, 2018.

[97] P. M. Shenai, S. Fernandez-Alberti, W. P. Bricker, S. Tretiak, and Y. Zhao, "Internal conversion and vibrational energy redistribution in chlorophyll a," *The Journal of Physical Chemistry B*, vol. 120, pp. 49–58, jan 2016.

[98] H. Kano and T. Kobayashi, "Time-resolved fluorescence and absorption spectroscopies of porphyrin J-aggregates," *The Journal of Chemical Physics*, vol. 116, pp. 184–195, dec 2001.

[99] L.-Q. Dong, K. Niu, and S.-L. Cong, "Theoretical analysis of internal conversion pathways and vibrational relaxation process of chlorophyll-a in ethyl ether solvent," *Chemical Physics Letters*, vol. 440, no. 1, pp. 150–154, 2007.

[100] N. Mataga, Y. Shibata, H. Chosrowjan, N. Yoshida, and A. Osuka, "Internal conversion and vibronic relaxation from higher excited electronic state of por-

phyrins: femtosecond fluorescence dynamics studies," *The Journal of Physical Chemistry B*, vol. 104, pp. 4001–4004, may 2000.

[101] J. C. Owrutsky, D. Raftery, and R. M. Hochstrasser, "Vibrational relaxation dynamics in solutions," *Annual Review of Physical Chemistry*, vol. 45, no. 1, pp. 519–555, 1994.

[102] M. Pajusalu, M. Rätsep, and A. Freiberg, "Temperature dependent electron–phonon coupling in chlorin-doped impurity glass and in photosynthetic FMO protein containing bacteriochlorophyll a," *Journal of Luminescence*, vol. 152, pp. 79–83, 2014.

[103] J. N. Sturgis and B. Robert, "Pigment binding-site and electronic properties in light-harvesting proteins of purple bacteria," *The Journal of Physical Chemistry B*, vol. 101, no. 37, pp. 7227–7231, 1997.

[104] T. Murata, F. Toda, K. Uchino, and E. Yakushiji, "Water-soluble chlorophyll protein of Brassica oleracea var. botrys (cauliflower)," *Biochimica et Biophysica Acta (BBA)-Bioenergetics*, vol. 245, no. 1, pp. 208–215, 1971.

[105] H. Satoh, A. Uchida, K. Nakayama, and M. Okada, "Water-soluble chlorophyll protein in brassicaceae plants is a stress-induced chlorophyll-binding protein," *Plant and Cell Physiology*, vol. 42, no. 9, pp. 906–911, 2001.

[106] A. Agostini, D. M. Palm, F.-J. Schmitt, M. Albertini, M. D. Valentin, H. Paulsen, and D. Carbonera, "An unusual role for the phytyl chains in the photoprotection of the chlorophylls bound to Water-Soluble Chlorophyll-binding Proteins," *Scientific reports*, vol. 7, no. 1, pp. 1–13, 2017.

[107] V. Prabahar, L. Afriat-Jurnou, I. Paluy, Y. Peleg, and D. Noy, "New homologues of brassicaceae water-soluble chlorophyll proteins shed light on chlorophyll binding, spectral tuning, and molecular evolution," *The FEBS journal*, vol. 287, no. 5, pp. 991–1004, 2020.

[108] D. M. Palm, A. Agostini, V. Averesch, P. Girr, M. Werwie, S. Takahashi, H. Satoh, E. Jaenicke, and H. Paulsen, "Chlorophyll a/b binding-specificity in water-soluble chlorophyll protein," *Nature Plants*, vol. 4, no. 11, pp. 920–929, 2018.

[109] D. Bednarczyk, O. Dym, V. Prabahar, Y. Peleg, D. H. Pike, and D. Noy, "Fine

tuning of chlorophyll spectra by protein-induced ring deformation," *Angew. Chemie - Int. Ed.*, vol. 55, no. 24, pp. 6901–6905, 2016.

[110] D. Horigome, H. Satoh, N. Itoh, K. Mitsunaga, I. Oonishi, A. Nakagawa, and A. Uchida, "Structural mechanism and photoprotective function of water-soluble chlorophyll-binding protein," *Journal of Biological Chemistry*, vol. 282, no. 9, pp. 6525–6531, 2007.

[111] A. Agostini, D. M. Palm, F.-J. Schmitt, M. Albertini, M. D. Valentin, H. Paulsen, and D. Carbonera, "An unusual role for the phytyl chains in the photoprotection of the chlorophylls bound to Water-Soluble Chlorophyll-binding Proteins," *Scientific Reports*, vol. 7, no. 1, p. 7504, 2017.

[112] C. Theiss, I. Trostmann, S. Andree, F. J. Schmitt, T. Renger, H. J. Eichler, H. Paulsen, and G. Renger, "Pigment - Pigment and pigment - Protein interactions in recombinant Water-Soluble Chlorophyll Proteins (WSCP) from cauliflower," *The Journal of Physical Chemistry B*, vol. 111, no. 46, pp. 13325–13335, 2007.

[113] S. Takahashi, H. Yanai, Y. Oka-Takayama, A. Zanma-Sohtome, K. Fujiyama, A. Uchida, K. Nakayama, and H. Satoh, "Molecular cloning, characterization and analysis of the intracellular localization of a water-soluble chlorophyll-binding protein (WSCP) from Virginia pepperweed (Lepidium virginicum), a unique WSCP that preferentially binds chlorophyll b in vitro," *Planta*, vol. 238, no. 6, pp. 1065–1080, 2013.

[114] M. Desclos, L. Dubousset, P. Etienne, F. Le Caherec, H. Satoh, J. Bonnefoy, A. Ourry, and J.-C. Avice, "A proteomic profiling approach to reveal a novel role of brassica napus drought 22 kd/water-soluble chlorophyll-binding protein in young leaves during nitrogen remobilization induced by stressful conditions," *Plant Physiology*, vol. 147, no. 4, pp. 1830–1844, 2008.

[115] H. Satoh, K. Nakayama, and M. Okada, "Molecular cloning and functional expression of a water-soluble chlorophyll protein, a putative carrier of chlorophyll molecules in cauliflower," *Journal of Biological Chemistry*, vol. 273, no. 46, pp. 30568–30575, 1998.

[116] T. Oba and H. Tamiaki, "Which side of the π-macrocycle plane of (bacterio) chlorophylls is favored for binding of the fifth ligand?," *Photosynthesis research*, vol. 74, no. 1, pp. 1–10, 2002.

[117] T. S. Balaban, "Relevance of the diastereotopic ligation of magnesium atoms of chlorophylls in the major light-harvesting complex ii (lhc ii) of green plants," *Photosynthesis research*, vol. 86, no. 1, pp. 251–262, 2005.

[118] E. Fresch, E. Meneghin, A. Agostini, H. Paulsen, D. Carbonera, and E. Collini, "How the protein environment can tune the energy, the coupling, and the ultrafast dynamics of interacting chlorophylls: The example of the water-soluble chlorophyll protein," *The journal of physical chemistry letters*, vol. 11, no. 3, pp. 1059–1067, 2020.

[119] R. S. Knox and B. Q. Spring, "Dipole strengths in the chlorophylls," *Photochemistry and Photobiology*, vol. 77, no. 5, pp. 497–501, 2003.

[120] D. Lindorfer, F. Müh, and T. Renger, "Origin of non-conservative circular dichroism of the CP29 antenna complex of photosystem II," *Physical Chemistry Chemical Physics*, vol. 19, no. 11, pp. 7524–7536, 2017.

[121] T. Renger, I. Trostmann, C. Theiss, M. E. Madjet, M. Richter, H. Paulsen, H. J. Eichler, A. Knorr, and G. Renger, "Refinement of a structural model of a pigment-protein complex by accurate optical line shape theory and experiments," *Journal of Physical Chemistry B*, vol. 111, no. 35, pp. 10487–10501, 2007.

[122] A. Agostini, D. M. Palm, H. Paulsen, and D. Carbonera, "Optically detected magnetic resonance of chlorophyll triplet states in water-soluble chlorophyll proteins from lepidium virginicum: Evidence for excitonic interaction among the four pigments," *The Journal of Physical Chemistry B*, vol. 122, no. 23, pp. 6156–6163, 2018.

[123] M. Chen, "Chlorophyll modifications and their spectral extension in oxygenic photosynthesis," *Annual review of biochemistry*, vol. 83, pp. 317–340, 2014.

[124] Z. Liu, H. Yan, K. Wang, T. Kuang, J. Zhang, L. Gui, X. An, and W. Chang, "Crystal structure of spinach major light-harvesting complex at 2.72 Å resolution," *Nature*, vol. 428, no. 6980, pp. 287–292, 2004.

[125] D. J. Swainsbury, K. M. Faries, D. M. Niedzwiedzki, E. C. Martin, A. J. Flinders, D. P. Canniffe, G. Shen, D. A. Bryant, C. Kirmaier, D. Holten, *et al.*, "Engineering of B800 bacteriochlorophyll binding site specificity in the Rhodobacter sphaeroides LH2 antenna," *Biochimica et Biophysica Acta (BBA)-Bioenergetics*, vol. 1860, no. 3, pp. 209–223, 2019.

[126] T. Brotosudarmo, S. Mackowski, E. Hofmann, R. Hiller, C. Bräuchle, and H. Scheer, "Relative binding affinities of chlorophylls in peridinin–chlorophyll–protein reconstituted with heterochlorophyllous mixtures," *Photosynthesis research*, vol. 95, no. 2, pp. 247–252, 2008.

[127] T. Polívka, M. Pellnor, E. Melo, T. Pascher, V. Sundström, A. Osuka, and K. R. Naqvi, "Polarity-tuned energy transfer efficiency in artificial light-harvesting antennae containing carbonyl carotenoids peridinin and fucoxanthin," *The Journal of Physical Chemistry C*, vol. 111, no. 1, pp. 467–476, 2007.

[128] T. Slee, A. Larouche, and R. F. Bader, "Properties of atoms in molecules: dipole moments and substituent effects in ethyl and carbonyl compounds," *The Journal of Physical Chemistry*, vol. 92, no. 22, pp. 6219–6227, 1988.

[129] H. Ishikita and K. Saito, "Proton transfer reactions and hydrogen-bond networks in protein environments," *Journal of The Royal Society Interface*, vol. 11, no. 91, p. 20130518, 2014.

[130] G. Ulrich, R. Ziessel, and A. Harriman, "The chemistry of fluorescent bodipy dyes: versatility unsurpassed," *Angewandte Chemie International Edition*, vol. 47, no. 7, pp. 1184–1201, 2008.

[131] H. Lu, J. Mack, Y. Yang, and Z. Shen, "Structural modification strategies for the rational design of red/NIR region BODIPYs," *Chemical Society Reviews*, vol. 43, no. 13, pp. 4778–4823, 2014.

[132] A. Schmitt, B. Hinkeldey, M. Wild, and G. Jung, "Synthesis of the Core Compound of the BODIPY Dye Class: 4, 4-Difluoro-4-bora-(3a, 4a)-diaza-s-indacene," *Journal of Fluorescence*, vol. 19, no. 4, pp. 755–758, 2009.

[133] M. Trapani, M. A. Castriciano, E. Collini, G. Bella, and M. Cordaro, "Supramolecular BODIPY based dimers: synthesis, computational and spectroscopic studies," *Organic & Biomolecular Chemistry*, vol. 19, no. 37, pp. 8118–8127, 2021.

[134] E. Fresch, N. Peruffo, M. Trapani, M. Cordaro, G. Bella, M. A. Castriciano, and E. Collini, "The effect of hydrogen bonds on the ultrafast relaxation dynamics of a BODIPY dimer," *The Journal of Chemical Physics*, vol. 154, no. 8, p. 084201, 2021.

[135] Y. Lee, S. Das, R. M. Malamakal, S. Meloni, D. M. Chenoweth, and J. M. Anna,

"Ultrafast solvation dynamics and vibrational coherences of halogenated boron-dipyrromethene derivatives revealed through two-dimensional electronic spectroscopy," *Journal of the American Chemical Society*, vol. 139, no. 41, pp. 14733–14742, 2017.

[136] J. D. Hybl, A. Albrecht Ferro, and D. M. Jonas, "Two-dimensional fourier transform electronic spectroscopy," *The Journal of Chemical Physics*, vol. 115, no. 14, pp. 6606–6622, 2001.

[137] D. B. Turner, R. Dinshaw, K.-K. Lee, M. S. Belsley, K. E. Wilk, P. M. Curmi, and G. D. Scholes, "Quantitative investigations of quantum coherence for a light-harvesting protein at conditions simulating photosynthesis," *Physical Chemistry Chemical Physics*, vol. 14, no. 14, pp. 4857–4874, 2012.

[138] A. Volpato, M. Zerbetto, L. Bolzonello, E. Meneghin, B. Fresch, T. Benelli, L. Giorgini, and E. Collini, "Effect of different conformational distributions on the ultrafast coherence dynamics in porphyrin-based polymers," *The Journal of Physical Chemistry C*, vol. 123, no. 16, pp. 10212–10224, 2019.

[139] C. Chudoba, E. Nibbering, and T. Elsaesser, "Ultrafast structural response of hydrogen bonded complexes to electronic excitation in the liquid phase," *The Journal of Physical Chemistry A*, vol. 103, no. 29, pp. 5625–5628, 1999.

[140] G.-J. Zhao and K.-L. Han, "Early time hydrogen-bonding dynamics of photoexcited coumarin 102 in hydrogen-donating solvents: theoretical study," *The Journal of Physical Chemistry A*, vol. 111, no. 13, pp. 2469–2474, 2007.

[141] T. Shimanouchi *et al.*, *Tables of molecular vibrational frequencies*, vol. 1. National Bureau of Standards Washington, DC, 1972.

[142] D. Green, F. VA Camargo, I. A. Heisler, A. G. Dijkstra, and G. A. Jones, "Spectral filtering as a tool for two-dimensional spectroscopy: a theoretical model," *The Journal of Physical Chemistry A*, vol. 122, no. 30, pp. 6206–6213, 2018.

[143] L. Lapinski, H. Rostkowska, M. J. Nowak, J. S. Kwiatkowski, and J. Leszczyński, "Infrared spectra of thiouracils: Experimental matrix isolation and ab initio Hartree-Fock, post-Hartree-Fock and density functional theory studies," *Vibrational Spectroscopy*, vol. 13, no. 1, pp. 23–40, 1996.

[144] T. Fornaro, M. Biczysko, J. Bloino, and V. Barone, "Reliable vibrational wavenumbers for CO and N-H stretchings of isolated and hydrogen-bonded

nucleic acid bases," *Physical Chemistry Chemical Physics*, vol. 18, pp. 8479–8490, mar 2016.

[145] V. Tiwari, "Multidimensional electronic spectroscopy in high-definition—combining spectral, temporal, and spatial resolutions," *The Journal of Chemical Physics*, vol. 154, no. 23, p. 230901, 2021.

[146] V. Tiwari, Y. A. Matutes, A. T. Gardiner, T. L. Jansen, R. J. Cogdell, and J. P. Ogilvie, "Spatially-resolved fluorescence-detected two-dimensional electronic spectroscopy probes varying excitonic structure in photosynthetic bacteria," *Nature Communications*, vol. 9, no. 1, 2018.

[147] P. Malý, J. Lüttig, S. Mueller, M. H. Schreck, C. Lambert, and T. Brixner, "Coherently and fluorescence-detected two-dimensional electronic spectroscopy: direct comparison on squaraine dimers," *Physical Chemistry Chemical Physics*, vol. 22, no. 37, pp. 21222–21237, 2020.

[148] A. A. Bakulin, C. Silva, and E. Vella, "Ultrafast spectroscopy with photocurrent detection: Watching excitonic optoelectronic systems at work," *Journal of Physical Chemistry Letters*, vol. 7, no. 2, pp. 250–258, 2016.

[149] A. Perdomo-Ortiz, J. R. Widom, G. A. Lott, A. Aspuru-Guzik, and A. H. Marcus, "Conformation and electronic population transfer in membrane-supported self-assembled porphyrin dimers by 2D fluorescence spectroscopy," *Journal of Physical Chemistry B*, vol. 116, no. 35, pp. 10757–10770, 2012.

[150] K. J. Karki, J. R. Widom, J. Seibt, I. Moody, M. C. Lonergan, T. Pullerits, and A. H. Marcus, "Coherent two-dimensional photocurrent spectroscopy in a PbS quantum dot photocell," *Nature Communications*, vol. 5, pp. 1–7, 2014.

[151] G. Nardin, T. M. Autry, K. L. Silverman, and S. T. Cundiff, "Multidimensional coherent photocurrent spectroscopy of a semiconductor nanostructure," *Optics express*, vol. 21, no. 23, pp. 28617–28627, 2013.

[152] L. Bolzonello, F. Bernal-texca, L. G. Gerling, J. Ockova, E. Collini, J. Martorell, and N. F. V. Hulst, "Photocurrent-detected 2D electronic spectroscopy reveals ultrafast hole transfer in operating PM6/Y6 organic solar cells," *Journal of Physical Chemistry Letters*, vol. 12, no. 16, pp. 3983–3988, 2021.

[153] S. Roeding and T. Brixner, "Coherent two-dimensional electronic mass spectrometry," *Nature Communications*, vol. 9, no. 1, pp. 1–9, 2018.

[154] M. Aeschlimann, T. Brixner, A. Fischer, C. Kramer, P. Melchior, W. Pfeiffer, C. Schneider, C. Strüber, P. Tuchscherer, and D. V. Voronine, "Coherent two-dimensional nanoscopy," *Science*, vol. 333, no. 6050, pp. 1723–1726, 2011.

[155] S. Röding, *Coherent multidimensional spectroscopy in molecular beams and liquids using incoherent observables*. PhD thesis, Universität Würzburg, 2018.

[156] J. R. Widom, N. P. Johnson, P. H. von Hippel, and A. H. Marcus, "Solution conformation of 2-aminopurine dinucleotide determined by ultraviolet two-dimensional fluorescence spectroscopy," *New Journal of Physics*, vol. 15, no. 2, p. 025028, 2013.

[157] G. A. Lott, A. Perdomo-Ortiz, J. K. Utterback, J. R. Widom, A. Aspuru-Guzik, and A. H. Marcus, "Conformation of self-assembled porphyrin dimers in liposome vesicles by phase-modulation 2d fluorescence spectroscopy," *Proceedings of the National Academy of Sciences*, vol. 108, no. 40, pp. 16521–16526, 2011.

[158] O. Kühn, T. Mančal, and T. Pullerits, "Interpreting fluorescence detected two-dimensional electronic spectroscopy," *Journal of Physical Chemistry Letters*, vol. 11, no. 3, pp. 838–842, 2020.

[159] H.-S. Tan, "Theory and phase-cycling scheme selection principles of collinear phase coherent multi-dimensional optical spectroscopy," *The Journal of chemical physics*, vol. 129, no. 12, p. 124501, 2008.

[160] S. Yan and H.-S. Tan, "Phase cycling schemes for two-dimensional optical spectroscopy with a pump–probe beam geometry," *Chemical Physics*, vol. 360, no. 1-3, pp. 110–115, 2009.

[161] S. Draeger, S. Roeding, and T. Brixner, "Rapid-scan coherent 2D fluorescence spectroscopy," *Optics Express*, vol. 25, no. 4, p. 3259, 2017.

[162] S. Mueller, J. Lüttig, P. Malý, L. Ji, J. Han, M. Moos, T. B. Marder, U. H. Bunz, A. Dreuw, C. Lambert, and T. Brixner, "Rapid multiple-quantum three-dimensional fluorescence spectroscopy disentangles quantum pathways," *Nature Communications*, vol. 10, no. 1, pp. 1–11, 2019.

[163] M. Liebel, C. Toninelli, and N. F. van Hulst, "Room-temperature ultrafast

nonlinear spectroscopy of a single molecule," *Nature Photonics*, vol. 12, no. 1, pp. 45–49, 2018.

[164] V. Tiwari, Y. A. Matutes, A. Konar, Z. Yu, M. Ptaszek, D. F. Bocian, D. Holten, C. Kirmaier, and J. P. Ogilvie, "Strongly coupled bacteriochlorin dyad studied using phase-modulated fluorescence-detected two-dimensional electronic spectroscopy," *Optics express*, vol. 26, no. 17, pp. 22327–22341, 2018.

[165] V. Tiwari, Y. A. Matutes, A. T. Gardiner, T. L. Jansen, R. J. Cogdell, and J. P. Ogilvie, "Spatially-resolved fluorescence-detected two-dimensional electronic spectroscopy probes varying excitonic structure in photosynthetic bacteria," *Nature Communications*, vol. 9, no. 1, pp. 1–10, 2018.

[166] F. A. Damtie, A. Wacker, T. Pullerits, and K. J. Karki, "Two-dimensional action spectroscopy of excitonic systems: Explicit simulation using a phase-modulation technique," *Physical Review A*, vol. 96, no. 5, pp. 1–12, 2017.

[167] L. Rodríguez-Pérez, M. Á. Herranz, and N. Martín, "The chemistry of pristine graphene," *Chemical Communications*, vol. 49, no. 36, pp. 3721–3735, 2013.

[168] V. Georgakilas, J. N. Tiwari, K. C. Kemp, J. A. Perman, A. B. Bourlinos, K. S. Kim, and R. Zboril, "Noncovalent functionalization of graphene and graphene oxide for energy materials, biosensing, catalytic, and biomedical applications," *Chemical reviews*, vol. 116, no. 9, pp. 5464–5519, 2016.

[169] S. Sahu and G. Rout, "Band gap opening in graphene: a short theoretical study," *International Nano Letters*, vol. 7, no. 2, pp. 81–89, 2017.

[170] A. K. Geim, "Graphene: status and prospects," *Science*, vol. 324, no. 5934, pp. 1530–1534, 2009.

[171] J. Albero, D. Mateo, and H. García, "Graphene-based materials as efficient photocatalysts for water splitting," *Molecules*, vol. 24, no. 5, p. 906, 2019.

[172] G. Moon, W. Kim, A. D. Bokare, N.-e. Sung, and W. Choi, "Solar production of H2O2 on reduced graphene oxide–TiO2 hybrid photocatalysts consisting of earth-abundant elements only," *Energy & Environmental Science*, vol. 7, no. 12, pp. 4023–4028, 2014.

[173] J. N. Tiwari, R. N. Tiwari, and K. S. Kim, "Zero-dimensional, one-dimensional, two-dimensional and three-dimensional nanostructured materials for ad-

vanced electrochemical energy devices," *Progress in Materials Science*, vol. 57, no. 4, pp. 724–803, 2012.

[174] J. N. Tiwari, R. N. Tiwari, G. Singh, and K. S. Kim, "Recent progress in the development of anode and cathode catalysts for direct methanol fuel cells," *Nano Energy*, vol. 2, no. 5, pp. 553–578, 2013.

[175] Q. Bao and K. P. Loh, "Graphene photonics, plasmonics, and broadband optoelectronic devices," *ACS nano*, vol. 6, no. 5, pp. 3677–3694, 2012.

[176] H.-X. Wang, Q. Wang, K.-G. Zhou, and H.-L. Zhang, "Graphene in light: design, synthesis and applications of photo-active graphene and graphene-like materials," *Small*, vol. 9, no. 8, pp. 1266–1283, 2013.

[177] A. M. Ross, S. Osella, V. R. Policht, M. Zheng, M. Maggini, F. Marangi, G. Cerullo, T. Gatti, and F. Scotognella, "Deciphering photoinduced charge transfer dynamics in a cross-linked graphene–dye nanohybrid," *The Journal of Physical Chemistry C*, vol. 126, no. 7, pp. 3569–3581, 2022.

[178] F. V. De Camargo, L. Grimmelsmann, H. L. Anderson, S. R. Meech, and I. A. Heisler, "Resolving vibrational from electronic coherences in two-dimensional electronic spectroscopy: The role of the laser spectrum," *Physical Review Letters*, vol. 118, no. 3, pp. 1–6, 2017.

List of Figures

List of Tables